論文 / 著書情報
Article / Book Information

題目(和文)	前周期遷移金属を用いた新規半導体の設計
Title(English)	Design for Novel Semiconductors Based on Early Transition Metals
著者(和文)	新井健司
Author(English)	Takeshi Arai
出典(和文)	学位:博士(工学), 学位授与機関:東京工業大学, 報告番号:甲第10834号, 授与年月日:2018年3月26日, 学位の種別:課程博士, 審査員:細野 秀雄,大場 史康,平松 秀典,松石 聡,神谷 利夫,多田 朋史
Citation(English)	Degree:Doctor (Engineering), Conferring organization: Tokyo Institute of Technology, Report number:甲第10834号, Conferred date:2018/3/26, Degree Type:Course doctor, Examiner:,,,,,
学位種別(和文)	博士論文
Type(English)	Doctoral Thesis

Design for Novel Semiconductors Based on Early Transition Metals

Takeshi Arai
2018
Department of Material Science and Engineering
Interdisciplinary Graduate School of Science and Engineering
Tokyo Institute of Technology

Contents

Design for Novel Semiconductors Based on Early Transition Metals 1
Chapter 1. General Introduction 4
1.1. Introduction 4
1.1.1. History and the present study 4
1.1.2. Frontier of materials exploration 6
1.1.3 Outline for introduction 7
1.2 Electronic structure of semiconductor 7
1.2.1 Physical properties and electronic structure 7
1.2.2 Theory for material design 9
1.2.3 Review of electronic structure previously reported 17
1.2.4 Summary of physical properties previously reported 21
1.3 Defect physics for semiconductors 21
1.4 Objectives of this study 27
1.4.1 Shift from *post* to *early* transition metals 27
1.4.2 Objective of the present study 27
1.4.3 Target properties ..... エラー! ブックマークが定義されていません。
References 28
Chapter 2. Design of transparent bipolar semiconductor: ZrOS 49
2.1 Introduction 49
2.2 Material design 49
2.3 Candidate Material 52
2.4 Validation from theoretical calculation 53
2.5 Experimental validation 55
2.6 Discussion 57
2.7 Conclusion 59
2.8 Appendix 59
2.9 Experimental section 60
References 63
Chapter 3. Inversion of carrier polarity with polymorph change in LaSeF 85
3.1 Introduction 85
3.2 Results 86
3.3 Discussion 90
3.4 Conclusion 94

3.5 Experimental section 94
References 96
Chapter 4. General conclusion 110
Acknowledgement 113
Publication lists 114
Presentation lists 115
Awards 115
Biography 116
Education 116

Chapter 1. General Introduction

1.1. Introduction

1.1.1. History and the present study

Novel functionality of semiconductors has been a strong driving force for a variety of revolutionary change and innovations in modern society. Since the invention of germanium based bipolar transistor in 1947-1948[1,2] and the subsequent success of silicon based metal-oxide-semiconductor field effect transistor, semiconductor devices have given rise to a new field, solid state electronics. Nowadays, Si-based large scale integrated circuits are key components in almost all electrical and electronic systems. In the meantime, compound and oxide semiconductors have established unique positions in those applications where Si devices cannot exhibit good performance owing to intrinsic material properties. For example, III-V semiconductors such as GaAs and InP have been widely employed for high-frequency devices and light-emitting diode[3,4]. Oxide semiconductors such as In_2O_3 and SnO_2 have been used for various applications such as transparent conductor and gas sensor[5,6].

In 1997, Kawazoe *et al* launched a novel design for *p*-type transport in wide-gap oxides where previous oxides cannot contribute[7]. They established the strategy to utilize "the chemical bonding between Cu 3*d* and O 2*p* orbitals" and validated it through experiments of $CuAlO_2$. This material design has opened up new avenues to develop hetero *p*-*n* junction of wide-gap oxides. In 2004, Nomura *et al* identified high electron mobility in amorphous of In-Ga-Zn-O system (*a*-IGZO)[8]. The electron mobility of *a*-IGZO (~10 $cm^2 V^{-1} s^{-1}$) is similar to those of the corresponding single crystals (~10 $cm^2 V^{-1} s^{-1}$). Conversely, for silicon, amorphous state reduces its carrier mobility (~0.1-1.0 $cm^2 V^{-1} s^{-1}$) from that of single-crystalline silicon (~100-1000 $cm^2 V^{-1} s^{-1}$). The *a*-IGZO

have been applied for the thin-film transistor in display backplane electronics, where the previous semiconductors cannot perform efficiently. This innovative functionality is based on the concept: the large spatially extended *s* orbital" of Ga^{3+} and In^{3+}. **Figure 1** summarizes the history of material design for wide-gap semiconductors. Always, realizing unique properties have been based on the novel material design.

These proposed material design is simple and outstanding, but don't incorporate the properties of point defects and valence changes, which are very important when carrier doping. Therefore, Cu based oxides are difficult to exhibit *n*-type conduction due to Cu^{1+} vacancy[9] and usual oxides don't show hole transport due to O^{2-} vacancy (and its deep valence band minimum). This poor dopability in wide-gap oxides results in problematic bipolar conduction, inhibiting homo *p*-*n* junction devices.

Considering the properties of defects, the design of semiconductor based on *early transition metals* (*e*TMs) is proposed. Almost previous semiconductors are constructed with *p*-block elements and post transition metals (*p*TMs), summarized in **Figure 1**. The *e*TMs are expected to effectively prevent cation vacancy, as described in section 1.3. This feature is important to control the carrier polarity in their ionic semiconductors. Additionally, the novel semiconductor based on the *e*TMs will also give new insights to defect physics for semiconductors.

Herein, target properties are bipolarity in wide-gap semiconductor, where wide-gap is basic for transparent electronics and next-generation power electronics. In the category of semiconductors based on the *p*TMs, it is difficult to achieve the coexistence of bipolarity and wide bandgap. However, the *e*TMs are suitable for polarity switch due to the effective prevention of cation vacancy.

In this doctoral thesis, I established design of wide-gap bipolar semiconductor. First,

tetragonal phase of ZrOS was proposed as transparent bipolar semiconductor in chapter 2. This design is based on three reliable strategies: utilizing *e*TM cations (Zr^{4+}) for improving carrier dopability, establishing chemical bonding suitable for bipolarity, and preparing forbidden bandgap to keep optical transparency. Then, by extending the concepts associated with ZrOS, hexagonal phase of LaSeF was found as a candidate of wide-gap bipolar semiconductors. However, accidentally, a polymorphic change from hexagonal to tetragonal phases was observed, accompanying a major carrier switch induced by doping of LaSeF. This is a rare case of a change in polymorph and carrier polarity induced by impurity doping. As a result, these findings will provide new insights into the design of wide-gap semiconductors.

1.1.2. Frontier of materials exploration

Recent progress in computer performance has stimulated data-driven materials exploration, so-called materials informatics. This is a method to find a material with the desired functionality by applying quantum calculation to an enormous number of materials on database such as ICSD. There are many articles related to materials informatics, for example, wide-gap *n*-type[10] and *p*-type[11,12] conductive oxides, transparent *p*-type conductors[13,14], thermoelectric materials[15], solar absorber[16,17], electride materials[18], and so on. Taking this mainstream into consideration, material exploration with no concept is impossible. However, for any materials exploration, the initial “idea” and “material concept” are required before the quantum calculation[19]. Thus, the aim of this study is to provide the initial “material concept” and “material design” based on a reliable strategy.

1.1.3 Outline for introduction

The outline of the following introduction is described here.

In section 1.2, the theory of chemical bonding is introduced to design functional semiconductor. The chemical bonding is a powerful tool to design electronic structure from constituent elements and crystal structure.

In section 1.3, the defect physics is described. The controllability of carrier polarity is determined by balance between ease of point defects and electronic structure.

In section 1.4, the objective of this doctoral thesis is shown.

1.2 Electronic structure of semiconductor

In this chapter, the bridge between elements and crystal structure, electronic structure, and physical properties in semiconductor is described. **Figure 2** summarizes the aim of this chapter. First, section 1.2.1 shows relationship between physical properties for semiconductors and its electronic structure. Then, section 1.2.2 indicates how to design the electronic structure from constituent elements and crystal structure by considering the chemical bonding. Finally, section 1.2.3 and 1.2.4 demonstrate electronic structures of several previous semiconductors and its performance, respectively.

1.2.1 Physical properties and band structure

Band structure is a powerful tool to guide the properties of semiconductors, namely the electrical transport and the optical absorption. Switching the carrier polarity (*n*-type and *p*-type), *i.e.*, bipolarity, plays an essential role to fabricate *p*-*n* junction. Additionally, the optical absorption properties determine the application of the semiconductor. If high,

such semiconductor is suable for solar absorber or light emitting device, but if low, for transparent electronics.

Electrical conductivity

The electrical conductivity σ is defined by the product of mobility μ and carrier concentration *n*, *i.e.*, $\sigma = en\mu$ [20]. The μ is represented as $\mu = e\tau/m^*$. Here, the τ denotes a mean free path, strongly depending on the crystalline state. The m^* represents the effective mass deriving from the band dispersion, $1/m^* \propto d^2E(k)/dk^2$. As band curvature is sharper, m^* is smaller and μ is larger as shown in **Figure 4a**. Therefore, sharp curve of band edge is required in order to obtain high electrical conductivity. The *n* at the room temperature is the number of electron or hole thermally excited from donor level or to acceptor level, respectively. The dopability of semiconductors are determined by the balance between ease of point defects and stability of carrier in a band. The latter is important from the viewpoint of electronic structure, and it is understood by the energy levels of CBM and VBM from a vacuum level, represented in **Figure 4b.** The electron and hole doping into semiconductors require a material with a large electron-affinity (deep CBM) and small ionization potential (shallow VBM) [21], respectively, because the electrons are more stabilized in a deeper CBM and removing the electrons from the VBM level (*i.e.*, generating the holes) is easier in a shallow VBM.

Optical absorption

The optical absorption occurs when electrons in the VB are excited to the CB by photon. The key parameters for this property are the bandgap E_g and the absorption coefficient α. The E_g is defined as the energy gap between CBM and VBM, being

consistent with the absorption edge. On the other hand, the α depends on the various factors; the *k* points of CBM and VBM levels, the forbidden or allowed transition of band edges, joint density of state (JDOS), and momentum matrix element (MME). The different *k* point of band edges (the indirect bandgap) suppresses the optical absorption because the optical excitation is done via phonon transition based on the conservation of momentum. Then, the forbidden transition of band edges also reduces the optical absorption. The edge of α for indirect, direct forbidden, and direct allowed bandgap are described as $\alpha \propto (h\nu\text{-}E_g)^n/h\nu$ (absorption edge) with n = 2, 3/2, and 1/2, respectively[22]. As shown in **Figure 5** (here, E_g = 1 eV), the direct allowed transition exhibits the steep edge of α. However, the weak α around E_g is shown in the direct forbidden and indirect bandgap. In the case of the direct allowed transition, we should consider JDOS and MME. However, because these parameters are not taken into consideration in the material design of this research, the explanation for them is omitted.

1.2.2 Theory for material design

Here, the theory of chemical bonding is described. We must design materials with desired functionality from constituent elements and crystal structures. An understanding of chemical bonding between atoms is important for this purpose. The chemical bonding is a powerful tool to connect the real and reciprocal space imaging. For example, imaging the flow of electrons in the semiconductor, the electron carrier travel along the path of atomic orbitals forming the conduction band. If the route is not paved, the carrier will not flow, *i.e.*, this route corresponding to flat CB. This pathway is formed by the chemical bonding between atomic orbitals. Therefore, we consider the process that the chemical bonds in real space form the electronic structure in reciprocal space.

The chemical bonding follows three factors; energy level of atomic orbitals, irreducible representation of atomic orbitals, and separation between atoms. Here, the theory of chemical bonding is qualitative, not quantitative. The quantitative is required for the detailed analysis but not appropriate for the initial design of the material.

Chemical bonding

As the distance between atoms decreases, the atomic orbitals mix and form new ground states. **Figure 6** shows the schematic of chemical bonding in two equivalent atoms **(a)** and two atoms of different polarity **(b)**[23]. The chemical bonding is constructed as combinations of atomic orbitals, and are then populated by electron pairs. When two equivalent atomic orbitals, s^A and s^B, combine, they yield a bonding combination and a corresponding anti-bonding orbital. The bonding combination is characterized by positive overlap, and by concentration of electron density in the region between the nuclei, resulting in the low energy level. By contrast, the anti-bonding combination exhibits negative overlap, and a node of the combined atomic orbitals in the region between the nuclei. When s^A and s^B are *s* orbitals, the bonding combination is $s^A + s^B$, and the antibonding one $s^A - s^B$, as shown in **Figure 6a**. Similar to **(a)**, the chemical bonding is also constructed in the case of **(b)**. However, unlike **(a)**, the components of s^C (here, cation) largely contributes to the anti-bonding state ($s^C - s^D$). Conversely, the s^D (anion) mainly constructs the bonding state ($s^C + s^D$). Thus, the atomic polarity results in the large difference of the energy levels between ($s^C + s^D$) and ($s^C - s^D$).

Related to the polarity, the valence state of atoms is important for understanding the components for the CB and VB in band structure. For example, in the case of NaCl, the 3*s* orbital of Na^+ is unoccupied and the 3*p* orbitals of Cl^- is fully occupied, owing to the

difference of polarity. Therefore, the CB and VB in NaCl are mainly composed of the 3*s* of Na^+ and the 3*p* of Cl^-, respectively. Another example is tin oxides (SnO and SnO_2). In SnO, the 5*p* orbitals of Sn^{2+} are empty and compose the CB. The 5*s* of Sn^{2+} and the 2*p* of O^{2-} are filled and therefore constitute the VB. On the other hand, in SnO_2, its CB and VB are composed of the unoccupied 5*s* of Sn^{4+} and the occupied 2*p* of O^{2-}, respectively.

Energy level of atomic orbitals

The polarity of atoms is related to the ionization energy and the electronegativity. The higher the ionization energy (and the electronegativity), the deeper the energy level of the atomic orbitals relative to the vacuum level. **Figure 7a** shows the ionization energy as a function of atomic number [24]. The energy level becomes deeper from the alkali metal to the halogen. This fact represents that the alkali metals and the halogens work as the strongest cations and anions, respectively. Additionally, the energy level of atoms is shallower as heavier, shown in **Figure 7b** [25].

As a tendency for electronic structure of semiconductors, the energy level of CBM mainly composed of alkali, alkaline earth, and early transition metals is too shallow to achieve *n*-type conductor. On the other hand, oxides and halides are not suitable for hole transport due to their deep VBM levels. For pnictogen and Te compounds, the bandgap often closes, resulting in a semimetallic state.

Symmetry and irreducible representation

Even in the case of near energy levels, the atomic orbitals with different irreducible representations (Irrep) never mix with each other. The state where an overlap of orbitals is forbidden by an Irrep is called “non-bonding state”. The Irrep is the symbol that

represents the periodic pattern of negative and positive phases of wave function in unit cell. When two orbitals possess the same Irrep, they mix and form the chemical bonding with each other [26]. **Figure 8a** is a schematic for the periodic pattern of atomic orbital phases. Here, the chain-type structure is formed of the *s* orbital on site A, s^{A}, with multiplicity two and the *p* orbitals on site B, p^{B}, with multiplicity one. The in-phase configuration of s^{A} orbital (s^{A} (in)) is totally symmetric and forms the boding nature. On the other hand, the out-of-phase configuration of s^{A} (s^{A} (out)) possesses the inversion symmetry with site B as the boundary, resulting in periodical repeats of the positive and negative sign of atomic phases. This periodicity is the same to the $p^{B}{}_{\sigma}$ orbital, which also has the inversion symmetry with site B. Thus, the overlap integral between the s^{A} (out) and $p^{B}{}_{\sigma}$ is finite, yielding the bonding and anti-bonding state as shown in **Figure 8b**. However, the periodic pattern of the s^{A} (in) and $p^{B}{}_{\pi}$ orbitals don't correspond to other orbitals, forming non-bonding state, respectively.

The Irrep depends on four factors: point group (space group), symmetry of atomic orbitals (*s*, *p*, or *d* orbitals), multiplicity and site symmetry, and *k* point. Here, this section indicates only the description for material design, not the mathematical details.

(i) *Space group and point group*

The space group determines the number of Irrep, which corresponds to the number of symmetry operation in the point group. Therefore, the number of Irrep increases in the higher symmetrical crystal structure. With the low symmetry crystal structure, the atomic orbitals belong to the same Irrep with high probability, forming the chemical bonding state. Conversely, the non-bonding state often occur in the crystal structure with high symmetry.

(ii) *Symmetry of atomic orbitals (s, p, or d orbitals),*

The atomic orbital has the specific symmetry depending on each shape. For example, *s* orbital is totally symmetric in real space. The in-phase configuration of the same atomic orbital ensures the bonding state regardless of its site symmetry. Conversely, the different atomic orbitals often form the non-bonding with each other.

(iii) *Multiplicity and site symmetry*

The Irrep in which the atomic orbit is characterized depends on the multiplicity and site symmetry. For example, when two atoms are present in the unit cell (that is, multiplicity two), the pattern of the sign of the wave function is divided into the in-phase and out-of-phase configurations. The number of Irrep of its atomic orbitals is at most its multiplicity.

The atomic orbital located at the low multiplicity site of the high symmetry crystal structure strongly interacts or doesn't form any bonding with the neighboring atomic orbitals. From the viewpoint of Irrep, the non-bonding state often appears with the different atomic symmetry on the high symmetry site in the high symmetry crystal structure.

(iv) *The k point*

The periodicity of wave function is changed by the *k* point. For example, at the G point, $k = (0, 0)$, the wave function is periodic in the unit cell, that is, the wave function of the neighbor unit cell is the same phase to that of the unit cell. In the case of the X point, $k = (\pi/a, 0)$, the periodicity of wave function is twice along the x direction, that is, the wave function of the nearest unit cell is the inverse phase to that of the unit cell. Therefore, we can regard that the formal unit cell doubles on the x axis and then changes the Irrep of the atomic orbitals.

Band Width

One important feature of a band is its dispersion, or band width; the difference in energy between the highest and lowest levels in the band. The width of bands depends on the separation of atoms in the real space. **Figure 9** illustrates example in detail for a molecular and a chain of H atoms spaced 3, 2, and 1 Å apart [27]. **Figure 9a** shows the energy levels of anti-bonding and bonding between hydrogens as a function of H-H distance. The shorter the distance, the larger the energy difference between them. This schematic corresponds to the band dispersion of the chain as shown in **Figure 9b**. At $k = \pi/a$, the phase of nearest atom is inverted and induces the anti-bonding nature. This results in the sharper curvature with the shorter separation of the atomic orbitals. The imagination of the electron path in real space is consistent with the feature of band curvature. For example, in the case of large separation, a = 3 Å, moving the electron is possible only by hopping between atomic orbitals. This hopping process inhibits the smooth movement of electrons and is consistent with the flat band. On the other hand, for a = 1 Å, the electron path is connected, leading to a good electrical transport. This short separation in real space brings the sharp curvature in band structure.

Bloch equation and chemical bonding [28]

In the periodicity of crystal structure, the wave function is defined as the Bloch function. **Figure 10** summarizes the relationship between the chemical bonding and the Bloch equation. The factor e^{ikr} induces the inverse phase in the nearest atom at $k \neq 0$. For example, at $k = \pi/a$, the phase of atomic orbital on $r = a$ is inverted but on $r = 2a$ is the same. This induces the bonding state of *p* orbitals and decreases the energy level.

Selection rule for band structure

The Irrep gives the information of not only chemical bonding but also transition of states by photon. The selection rule of a interband transition of the band structure is derived from a triple direct product (TDP) between an initial state, a final state, and a direction of polarity of electromagnetic radiation[29]. When the triple direct product includes the totally symmetric representation (A_1 and A_{1g}), its transition is allowed. Generally, when the two states correspond to the same Irrep, its direct product produces the totally symmetric class A_{1g} (A_1). Therefore, if the direct product between the CBM state and the VBM state (CBM $\otimes$ VBM) includes the Irrep of polarization of the light (CBM $\otimes$ VBM $\supset p_{x/y/z}$), the interband transition of its band edge states is allowed (CBM $\otimes$ $p_{x/y/z}$ $\otimes$ VBM $\supset A_1$ or A_{1g}). **Figures 11** shows the multiplication tables for D_{4h} and D_{2d}, whose matrix denotes the direct product between band states having a row of Irrep and a column of Irrep. The allowed transitions are marked with the orange and blue colors for the p_x (p_y) and p_z polarized lights, respectively. Apparently, in the case of D_{4h} group which has 10 classes of Irrep, the many forbidden transitions relatively appear than the case of D_{2d} group due to odd and even characters. Thus, it is indicated that the nature of the forbidden optical transition is closely related to the point groups with the high symmetry.

Strategy for material design

(i) *Electrical conductivity*

Effective mass of electron and hole

The effective mass is described as $1/m^* \propto d^2E(k)/dk^2$, which corresponds to the difference in the energy with the slightly change of k point on band edge. There are three

simple methods to reduce the effective mass. First, short separation of atoms is useful. The short separation of cations (anions) is effective to decrease the electron (hole) effective mass. The second is to utilize a largely spread atomic orbitals derived from the high group of elements. Third is to utilize the fact that the chemical bonding state changes in *k* space. The change of chemical bonding state depending on k point makes the bandwidth wider.

Energy levels of CBM and VBM from vacuum level

To decrease the CBM level requires high ionization energy of cation, low Madelung energy from anion, weak anti-bonding between cation and anion, and strong bonding state between cations. On the other hand, the VBM for hole doping is oppose to the CBM for electron doping. The requirements for enhancing the VBM level are low ionization energy of anion, low Madelung energy from cation, weak bonding nature between cation and anion, and strong anti-bonding between anions.

(ii) *Optical absorption*

Bandgap

The energy levels of CBM and VBM determine not only carrier doping efficiency but also bandgap.

Indirect or direct bandgap

It is difficult to exactly predict the k point of CBM and VBM states. This reason is that its maximum or minimum energy levels are determined depending on how atoms are arranged in the unit cell and the specific form of the atomic orbitals.

Forbidden or allowed transition of band edge

This content is described above in Selection rule for band structure. As the symmetry

is higher, the forbidden transition often appears.

1.2.3 Review of electronic structure previously reported

In this section, we review electronic structures of functional semiconductors known so far. In the beginning, the valence state of cation and anion should be checked to understand the chemical bonding. For example, in the case of Sn^{2+}, since it takes the state of $(5s)^2(5p)^0$ as electronic configuration, the energy of Sn 5*s* orbital is below Fermi energy because the orbital is formally filled by electrons, and the energy of Sn 5*p* orbital is above Fermi energy. On the other hand, in the case of Sn^{4+} whose state is formally $(5s)^0(5p)^0$, its *s* orbital forms not the valence band but the conduction band. Thus, SnO and SnO_2 are totally different compounds from the view point of electronic structure. **Figure 12** shows the schematic electronic structure of Si, oxides, and Cu based oxides.

(i) Covalent semiconductor: Si

Si is representative of covalent semiconductors, whose band edge states are composed of hybridized sp^3 σ and σ*-bonding as VBM and CBM, respectively. These features are derived from tetrahedral network in Diamond or Wurtzite crystal structure. The high mobility and efficient carrier doping appear in IV or III-V semiconductors, where have been applied to a variety of optelectronic devices.

Main Group elements as cation

(ii) oxides based on the cations with spatially spread *ns* orbital: In_2O_3

In_2O_3 is famous as transparent conductive oxides (TCOs) and is shown here as a representative of a conventional oxide semiconductor. The material design of TCOs is

based on post-transition metal (*pTM*) ions such as In^{3+}, Cd^{2+}, and Sn^{4+}, whose states are $((n\text{-}1)d)^{10}(ns)^0(np)^0$, $n \geq 5$[30,31,32]. The unoccupied 5*s* orbitals of In^{3+} and Cd^{2+} widely spatial spread, thus bringing the strong bonding between cations (**Figure 12b**). Decreasing CBM level and electron effective mass lead to the excellent *n*-type conductivity. Additionally, the deep VBM level composed of O *p* orbitals widens the bandgap and keep the optical transparency in the visible light. However, the fabrication of *p*-type conductivity is difficult due to its deep VBM, preventing homo *p*-*n* junction. From the viewpoint of chemical bonding, the family of In_2O_3 [33] are ZnO [34], Ga_2O_3 [35], CdO [36], SnO_2 [37], and $InGaZnO_4$ [38,39].

(iii) Cu^{1+} based oxides: $CuAlO_2$

$CuAlO_2$ is the first reported transparent *p*-type oxide semiconductors [7]. In order to obtain *p*-type in oxides, they utilized Cu^{1+} whose 3*d* orbitals is filled with electrons, $(3d)^{10}(4s)^0$. The fully occupied 3*d* orbitals form the chemical bonding with O 2*p* orbitals, widening the valence band width. This anti-bonding raises the VBM level and decreases the hole effective mass (**Figure 12c**). Additionally, expansion of the bandgap requires shallow CBM level. For it, they weakened the bonding state of Cu 4*s* by using two dimensional structure of $CuAlO_2$. Extended from this material concept, $CuGaO_2$ [40] and $CuInO_2$ [41] are discovered. In particular, $CuInO_2$ was noted as the transparent bipolar semiconductor. Its CBM is composed of spatially spread 5*s* orbitals of In^{3+}, which is suitable for the *n*-type conductivity. This chemical bonding results in the narrow bandgap, but the optical transition of band edges is forbidden by crystal symmetry [42]. These features lead to the bipolar conduction with remaining the optical transparency. From the viewpoint of chemical bonding, the family of $CuAlO_2$ [43] are Cu_2O [44], $SrCu_2O_2$ [45,46],

LaCuOS [47], $CuInSe_2$ [48], Cu_3N [49], and CuI [50].

(iv) Sn^{2+} based oxides: SnO

SnO is one of the transparent bipolar semiconductors [51]. The electronic structure of SnO is similar to that of Cu based oxides in terms of the use of anti-bonding between cation and anion. Since the formal electronic configuration of Sn^{2+} is $(5s)^2(5p)^0$, the occupied 5*s* and unoccupied 5*p* orbitals compose the VB and CB. Its CB is mainly composed of Sn *p* orbitals and its VB is composed of the anti-bonding between Sn 5*s* orbital and O 2*p* orbitals. Although SnO is narrow-gap semiconductor, this material keeps optical transparency by indirect bandgap [52]. From the viewpoint of chemical bonding state, the family of SnO [53] are PbO [54], InI [55], and $CsPbI_3$ [56].

(v) Superdegeneracy based *n*-type transport: $SrGeO_3$

$SrGeO_3$ is the first Ge based transparent electronic conductor[57]. Conventional design for TCOs is based on the properties of elements, that is, TCO cations. However, the design of $SrGeO_3$ is based on the crystal symmetry, namely, "superdegeneracy"[58]. The superdegeneracy denotes the non-bonding between cation and anion at the specific *k* point. **Figure 13** shows the electronic structure and the schematic of orbital diagram at the Γ and X points. At the Γ point, Ge 4*s* orbital is prohibited from interacting with O 2*p* orbitals due to its local symmetry and periodicity. Additionally, the bonding state between Ge and Ge in neighboring unit cell deepens the CBM level, resulting in *n*-type conduction. In order to eliminate the anti-bonding between Ge 4*s* and O 2*p*, the high symmetry crystal structure, cubic perovskite, is important. On the other hand, at X point, the reactive anti-bonding between Ge 4*s* and O 2*p* enhances its energy level, resulting in broad bandwidth

and small effective mass of electron. Similar to other oxides, the deep VBM level O 2*p* keeps the optical transparency in the visible light.

Transition metals as cations

(vi) Ligand field and d^6 cations: $ZnRh_2O_4$

$ZnRh_2O_4$ is reported as wide-gap *p*-type oxide semiconductors[59], based on the design utilized the ligand field between Rh 4*d* orbitals and O 2*p* orbitals. The octahedral coordination (RhO_6) splits the energy levels of *d* orbital into e_g and t_{2g}. Six electrons of Rh^{3+} occupy the t_{2g} level, that is, the low-spin state of $(t_{2g})^6(e_g)^0$ due to its large ligand field[60]. The $(t_{2g})^6(e_g)^0$ electronic configuration of Rh^{3+} is similar to the $(3d)^{10}(4s)^0$ of Cu^{1+}. The *p*-type conduction is validated by experiments.

(vii) High spin state and d^5 cations: Cr_2MnO_4

Cr2MnO4 is designed as transparent p-type conductor, by utilizing the high spin state of Mn^{2+} [12]. The half-filled 3*d* orbitals of Mn^{2+}, $(3d)^5(4s)^0$, induces spin polarization state, whose up and down spin texture compose its VB and CB, respectively. The polarized state in band components leads to the forbidden transition, enhancing optical transparency. However, the strongly correlated state localizes electrons leading to flat bands and large effective mass.

(viii) Covalent bond of 5*d* orbitals: TaIrGe

TaIrGe is transparent *p*-type conductor, which is discovered by utilizing "Inverse Material Design" [14]. The crystal structure is a half Heusler and the covalent bond between Ta 5*d*, Ir 5*d*, and Ge 4*p* orbitals composes the VBM. This is a novel design because the

covalent bonding of the large extended 5*d* orbitals is utilized. This strong covalent bonding results in the small hole effective mass and the wide-gap nature in this material.

1.2.4 Summary of physical properties previously reported

In this section, the reported physical properties so far are summarized. Generally, the semiconducting properties, in particular, carrier mobility, strongly depend on its crystalline (*i.e.* growth process) [61,62,63]. Single crystalline, where electrons have long mean free path, exhibits a higher mobility than poly crystalline. **Table 1** summarizes the electrical transport properties for semiconductors representing the electronic structure shown in section 1.2.3. Although the bipolarity with wide-gap nature appears in the covalent semiconductors such as GaN, the most oxides are limited to unipolar transport.

1.3 Defect physics for semiconductors

Here, we consider the effect of defects on semiconductors. In the above, the “ideal” electronic structures were introduced. However, the real crystal usually possesses the defects such as the vacancy, interstitial atom, and antisite of atoms. These defects behave as the source of carriers or carrier-killer. Thus, this property is important for controlling electronic transport properties. As described below, the tendency of defects follows a defect formation energy. Here, the formation energy of the point defects is explained and then the empirical doping rule is introduced.

Formation energy of point defects

The point defects in ionic compounds induce the electron or hole carrier due to its

charge neutral condition. Thus, it is important to understand the behavior of point defects from the viewpoint of the control of carrier concentration and polarity. The defect formation energy, E_f, was evaluated as [64,65]

$$E_f = E_t^d - E_t^p - \sum_i \Delta n_i \mu_i + qE_F \qquad (1)$$

where E_t^d and E_t^p denote the total energies of the supercell containing a defect with the charge q and the perfect-crystal supercell, and Δn_i is the difference in the number of constituent atoms of type i before and after defects (for instance, in ZnO, $\Delta N_{Zn} = 0$ and $\Delta N_O = -1$ for the O vacancy and $\Delta N_{Zn} = 1$ and $\Delta N_O = 0$ for the Zn interstitial). μ_i and E_F are the atomic chemical potential and the Fermi energy, respectively. μ is a parameter possible to be controlled with an atmosphere of various gas.

Figure 14 shows formation energies of oxygen vacancy with q = 0, +1, and +2 as a function of the Fermi level[66]. (**a**) and (**b**) represent O-poor and O-rich limit conditions, which are different in chemical potential of oxygen. There are mainly two important things in this figure. The first one is the donor level derived from oxygen vacancy. This level is determined by the cross of formation energies with neutral and 2+ charge vacancies. Therefore, the donor level is located on the ~2.2 eV above VBM level (~1 eV below CBM level), indicating deep donor level. This denotes that the oxygen vacancy doesn't play an effective role to generate electron carrier, at least from the viewpoint of calculation. In additional explanation, at E_F = 3 eV above VBM level, the oxygen vacancy doesn't release the electron carriers because the formation energy of neutral vacancy is the smallest as shown in **Figure 14a**. The second thing is the formation energy around VBM level in O-rich condition (b). O-rich condition represents the most suitable condition for hole-doping owing to effective prevention of O vacancy. However, **Figure 14b** shows the formation energy of 2+ charge vacancy is near to zero around VBM level,

indicating small enough to behave as a hole killer. Therefore, *p*-type doping into ZnO is difficult.

Considering the example of O vacancy in ZnO, one of the important factor in (1) is the value of E_t^d - E_t^p which represents the difference in total energy of crystal between before and after defects. To prevent the ion vacancies working as carrier-killer requires the high value of E_t^d - E_t^p. Unfortunately, the law determining E_t^d - E_t^p remains unknown. However, several origins of E_t^d - E_t^p can be thought intuitively.

Estimated origin of point defects

(i) Vacancy = low coordinated or asymmetric local structure

The formation energy of vacancy depends on the coordination number and the local structure. For example, in Cu_2O, the local structure of Cu forms the dumbbell, O-Cu-O, and two atoms of O are coordinated to Cu. The low coordinated Cu is easy to become vacancy because it is easy to cut two hands of Cu-O. That is, the total energy is not much different between O-Cu-O and O-V_{Cu}-O. **Figure 15a** shows formation energies of defects in Cu_2O [9]. Clearly, the Cu vacancy possesses the low formation energy than other defects. Additionally, the acceptor level derived from Cu vacancy is located at 0.25 eV from VBM level, being shallow enough to supply hole carrier. Therefore, Cu based oxides which have the dumbbell-like local structure often exhibit intrinsic hole transport. As an another example, Sn vacancy in SnO is introduced. The local structure around Sn^{2+} in SnO is unsymmetric to c-axis direction, and four bonds of Sn-O forms only at one side. This unsymmetric structure induces the easy formation of Sn vacancy. **Figure 15b** shows formation energies of defects in SnO[67]. Both of the formation energies of Sn and O vacancies are sufficiently small. However, although the acceptor level formed by Sn

vacancy is located at the level near to VBM, the donor level originated in O vacancy is relatively deep (~0.1 eV below CBM) even in narrow bandgap (~0.3 eV including DFT error). This indicates that the Sn vacancy works as hole-doping but O vacancy doesn't generate the electron carrier. In fact, SnO intrinsically exhibits p-type conduction, and *n*-type of SnO is accomplished with heavy substitution (~8 %) of Sb^{3+} into Sn^{2+} site [51].

Generally, the low valence state such as Cu^{1+} induces the low coordination number. Thus, in order to fabricate *n*-type, low valence cation is not suitable. Conversely, the high valence state such as Y^{3+} and Zr^{4+} is useful to prevent the cation vacancy due to its high coordination number.

(ii) Antisite = two constituent atoms with similar ionic radii and local structure

Antisite occurs between atoms with similar ionic radii and local structures. CuInSe2 (CIS) is introduced as an example. The ionic radii of In^{3+} and Cu^{1+} on four coordinated site are 0.62 Å and 0.60 Å, respectively, and the site symmetry of In^{3+} and Cu^{1+} is the same. **Figure 16** shows formation energies of defects in CIS [68]. At any conditions, the antisite of In^{3+} into Cu^{1+} site (red solid line) and the Cu vacancy (blue dot line) exhibit the low formation energy. In condition of D, which is the case of Cu-rich and In-rich conditions, when E_F is around CBM level, Cu vacancy inhibits the electron doping. When E_F is around VBM level, the In_{Cu} plays a main role to prevent the hole doping. These behaviors give the birth to the pinning Fermi energy at 0.7 eV as shown in D of **Figure 16**.

When the local structure forms the tetrahedral network shown in Diamond-type structure, the antisite sometimes occurs due to the similar local structure of every component. Conversely, ionic crystal with various local structures unlimited to the tetrahedral structure is useful to prevent the antisite.

(iii) Interstitial atom = space of crystal structure that atoms can occupy

The interstitial atoms require the space that atoms can occupy. For example, in Cu_3N whose structure is ReO_3 type, the space exists in the center of cubic structure. This space can be occupied by Li^{1+} or Cu^{1+} as the interstitial cation, doping electron carrier into compound [69,70]. Therefore, the bipolar conductivity is realized in Cu_3N by these interstitial cations despite Cu based semiconductor. The large space reduces the difference in the total energy before and after interstitial atoms. Conversely, the high dense ionic crystal is effective for suppressing interstitial atoms.

Facile valence change of cations: Cu^{1+} ⇔ Cu^{2+} and Sn^{2+} ⇔ Sn^{4+}

Additionally, one of the important factors that inhibit carrier doping is facile valence state of cation such as Cu^{1+} and Sn^{2+}. The facile valence change is related to the competitive electronic configurations of the *pTM* with $(n-1)d^9ns^0$ or $(n-1)d^{10}ns^0$ for group-11 elements, such as Cu, and $(n-1)d^{10}ns^2np^0$ or $(n-1)d^{10}ns^0np^0$ for heavy group-13, 14, and 15 elements, such as In, Sn, and Pb. The two stable electronic configurations induce multiple stable phases, for example, PbO (Pb^{2+}) ↔ PbO_2 (Pb^{4+}), making carrier doping into these compounds difficult. For example, when attempting to make a Pb^{2+} vacancy in PbO to attain *p*-type conduction, a mixture of PbO and PbO_2 is obtained instead of $Pb_{1-x}O$[71]. This feature is not separated from the electronic structure of "*p*-type cations" such as Cu^{1+}, Sn^{2+}, and Pb^{2+}.

Empirical doping limit

Whether carrier doping is possible or not is determined by the battle of stability for point defects and carrier doping. As described above, the properties of point defects

strongly depend on the constituent elements and the local structure. Thus, the nature of the point defects resembles in similar compounds. As long as we consider similar compounds, we can only consider the stability of carrier, that is, the energy levels of VBM and CBM. This premise supports the validity of doping limit rule.

(i) III-V, II-VI binaries, and I-III-VI_2 ternaries

Figure 17 summarizes the doping limit rules for III-V, II-VI, and I-III-VI_2 compounds [21,72]. The dashed lines (solid line in III-V) represent the pinning energy, $E_{pin}(n)$ and $E_{pin}(p)$ denoting the *n*-type and *p*-type doping limit, respectively. When the energy level of CBM, E_{CBM}, is below $E_{pin}(n)$, the electron doping can be achieved. Conversely, *p*-type doping can be accomplished when $E_{VBM} > E_{pin}(p)$. Apparently, the range of doping limit is narrower in the case of I-III-VI_2 compounds, and in particular $E_{pin}(n)$ of I-III-VI_2 is much deeper than those of III-V and II-VI. This is consistent with the difficulty of *n*-type doping in Cu based oxides and CIGS.

(ii) Ionic compounds

Figure 18 summarizes the doping limit for ionic compounds such as oxides and chalcogenides[73]. This band alignment indicates ~4 eV and ~6 eV from vacuum level as *n*-type and *p*-type limits, respectively. Almost *p*-type material includes Cu^{1+} as cation, and therefore to obtain E_{VBM} above 6 eV requires the anti-bonding nature between Cu 3*d* and O 2*p*. However, these Cu^{1+} based compounds don't exhibit *n*-type conductivity by suffering poor doping efficiency owing to Cu^{1+} vacancy. Fundamentally, the Cu^{1+} (Sn^{2+}) vacancy and the deep VBM state composed of O 2*p* orbitals in non-Cu^{1+} (Sn^{2+}) based oxides inhibit the *n*-type and *p*-type carrier doping, respectively. These features prevent homo *p*-*n* junction devices in oxides.

1.4 Objectives of this study

1.4.1 Shift from *post* to *early* transition metals

Early transition metals (*e*TM) have received little attention so far. Most of the conventional semiconductors are based on post transition metals (*p*TM) because the chemical bonding of *p*TM atomic orbitals gives the good electric transport to semiconductors. **Figure 19** shows the comparison of band structures between ZrO_2, ZrS_2, and SnO_2. The conduction bands composed of Zr 4*d* orbitals is relatively flat than that of Sn 5*s* orbital. Therefore, by designing the chemical bonding, I need to choose the crystal structure leading to suitable electronic structure. On the other hand, the *e*TMs are useful to suppress cation vacancy generating the hole carrier because the compound of *e*TM forms a structure with high coordination number (see **Figure 20**) which have the large difference of total energy when the formation of cation vacancy.

1.4.2 Objective of the present study

The objective of the present study is to investigate the superior and clarify requirements of material design in the wide-gap semiconductors based on *e*TMs.

Target properties are “bipolar doping in wide-gap semiconductors”, namely, “the control of carrier polarity in the wide-gap semiconductors”. The bipolar doping in wide-gap leading to transparent and power electronics is challenging in fundamental research of semiconductors and is meaningful in industry..

References

(1) Bardeen, J.; Brattain, W. H. *Phys. Rev.* **1948**, *74* (2), 230.

(2) William, S. Bell System Technical Journal Vol. 28 No. 3 (July 1949) pp. 435-89.

(3) Berroth, M.; Bosch, R. *IEEE Trans. Microw. Theory Tech.* **1991**, *39* (2), 224.

(4) Ostermayer, F. W.; Kohl, P. A.; Burton, R. H. *Appl. Phys. Lett.* **1983**, *43* (7), 642.

(5) Minami, T. *MRS Bull.* **2000**, *25* (8), 38.

(6) Barsan, N.; Schweizer-Berberich, M.; Göpel†, W. *Fresenius J. Anal. Chem.* **1999**, *365* (4), 287.

(7) Kawazoe, H.; Yasukawa, M.; Hyodo, H.; Kurita, M.; Yanagi, H.; Hosono, H. *Nature* **1997**, *389* (6654), 939.

(8) Nomura, K.; Ohta, H.; Takagi, A.; Kamiya, T.; Hirano, M.; Hosono, H. *Nature* **2004**, *432* (7016), 488.

(9) Raebiger, H.; Lany, S.; Zunger, A. *Phys. Rev. B* **2007**, *76* (4), 045209.

(10) Hautier, G.; Miglio, A.; Waroquiers, D.; Rignanese, G.-M.; Gonze, X. *Chem. Mater.* **2014**, *26* (19), 5447.

(11) Hautier, G.; Miglio, A.; Ceder, G.; Rignanese, G.-M.; Gonze, X. *Nat. Commun.* **2013**, *4*, 2292.

(12) Peng, H.; Zakutayev, A.; Lany, S.; Paudel, T. R.; d'Avezac, M.; Ndione, P. F.; Perkins, J. D.; Ginley, D. S.; Nagaraja, A. R.; Perry, N. H.; Mason, T. O.; Zunger, A. *Adv. Funct. Mater.* **2013**, *23* (42), 5267.

(13) Varley, J. B.; Miglio, A.; Ha, V.-A.; van Setten, M. J.; Rignanese, G.-M.; Hautier, G. *Chem. Mater.* **2017**, *29* (6), 2568.

(14) Yan, F.; Zhang, X.; Yu, Y. G.; Yu, L.; Nagaraja, A.; Mason, T. O.; Zunger, A. *Nat. Commun.* **2015**, *6*, ncomms8308.

(15) Gaultois, M. W.; Sparks, T. D.; Borg, C. K. H.; Seshadri, R.; Bonificio, W. D.; Clarke, D. R. *Chem. Mater.* **2013**, *25* (15), 2911.

(16) Hinuma, Y.; Hatakeyama, T.; Kumagai, Y.; Burton, L. A.; Sato, H.; Muraba, Y.; Iimura, S.; Hiramatsu, H.; Tanaka, I.; Hosono, H.; Oba, F. *Nat. Commun.* **2016**, *7*, 11962.

(17) Brandt, R. E.; Stevanović, V.; Ginley, D. S.; Buonassisi, T. *MRS Commun.* **2015**, *5* (2), 265.

(18) Zhang, Y.; Wang, H.; Wang, Y.; Zhang, L.; Ma, Y. *Phys. Rev. X* **2017**, *7* (1), 011017.

(19) Jain, A.; Ong, S. P.; Hautier, G.; Chen, W.; Richards, W. D.; Dacek, S.; Cholia, S.; Gunter, D.; Skinner, D.; Ceder, G.; Persson, K. A. *APL Mater.* **2013**, *1* (1), 011002.

(20)

(21) Zunger, A. *Appl. Phys. Lett.* **2003**, *83* (1), 57.

(22) Grosso, G.; Parravicini, G. P. *Solid State Physics, Second Edition*, 2 版.; Academic Press: Amsterdam, 2013.

(23) Woodward, R. B.; Hoffmann, R. *Angew. Chem. Int. Ed. Engl.* **1969**, *8* (11), 781.

(24) Harrison, W. A. *Electronic Structure and the Properties of Solids: The Physics of the Chemical*

Bond; Courier Corporation, 2012.

(25) Kutzelnigg, W. *Angew. Chem. Int. Ed. Engl.* **1984**, *23* (4), 272.

(26) Konno, T. *Symmetry in Matter and Group Theory*.

(27) Hoffmann, R. *Angew. Chem. Int. Ed. Engl.* **1987**, *26* (9), 846.

(28) Cox, P. A. *The Electronic Structure and Chemistry of Solids*; Oxford University Press, U.S.A.: Oxford, 1987.

(29) Dresselhaus, M. S.; Dresselhaus, G.; Jorio, A. *Group Theory: Application to the Physics of Condensed Matter*; Springer Science & Business Media, 2007.

(30) Medvedeva, J. E.; Freeman, A. J. *EPL Europhys. Lett.* **2005**, *69* (4), 583.

(31) Robertson, J. *J. Phys. C Solid State Phys.* **1979**, *12* (22), 4767.

(32) Kawazoe, H.; Yanagi, H.; Ueda, K.; Hosono, H. *MRS Bull.* **2000**, *25* (8), 28.

(33) Mryasov, O. N.; Freeman, A. J. *Phys. Rev. B* **2001**, *64* (23), 233111.

(34) Schröer, P.; Krüger, P.; Pollmann, J. *Phys. Rev. B* **1993**, *47* (12), 6971.

(35) Yamaguchi, K. *Solid State Commun.* **2004**, *131* (12), 739.

(36) Jaffe, J. E.; Pandey, R.; Kunz, A. B. *Phys. Rev. B* **1991**, *43* (17), 14030.

(37) Svane, A.; Antoncik, E. *J. Phys. Chem. Solids* **1987**, *48* (2), 171.

(38) Kamiya, T.; Nomura, K.; Hosono, H. *Sci. Technol. Adv. Mater.* **2010**, *11* (4), 044305.

(39) Chen, C.; Cheng, K.-C.; Chagarov, E.; Kanicki, J. *Jpn. J. Appl. Phys.* **2011**, *50* (9R), 091102.

(40) Ueda, K.; Hase, T.; Yanagi, H.; Kawazoe, H.; Hosono, H.; Ohta, H.; Orita, M.; Hirano, M. *J. Appl. Phys.* **2001**, *89* (3), 1790.

(41) Yanagi, H.; Hase, T.; Ibuki, S.; Ueda, K.; Hosono, H. *Appl. Phys. Lett.* **2001**, *78* (11), 1583.

(42) Nie, X.; Wei, S.-H.; Zhang, S. B. *Phys. Rev. Lett.* **2002**, *88* (6), 066405.

(43) Yanagi, H.; Inoue, S.; Ueda, K.; Kawazoe, H.; Hosono, H.; Hamada, N. *J. Appl. Phys.* **2000**, *88* (7), 4159.

(44) Ruiz, E.; Alvarez, S.; Alemany, P.; Evarestov, R. A. *Phys. Rev. B* **1997**, *56* (12), 7189.

(45) Ohta, H.; Orita, M.; Hirano, M.; Yagi, I.; Ueda, K.; Hosono, H. *J. Appl. Phys.* **2002**, *91* (5), 3074.

(46) Robertson, J.; Peacock, P. W.; Towler, M. D.; Needs, R. *Thin Solid Films* **2002**, *411* (1), 96.

(47) Kamiya, T.; Ueda, K.; Hiramatsu, H.; Kamioka, H.; Ohta, H.; Hirano, M.; Hosono, H. *Thin Solid Films* **2005**, *486* (1), 98.

(48) Jaffe, J. E.; Zunger, A. *Phys. Rev. B* **1983**, *28* (10), 5822.

(49) Hou, Z. F. *Solid State Sci.* **2008**, *10* (11), 1651.

(50) Ferhat, M.; Zaoui, A.; Certier, M.; Dufour, J. P.; Khelifa, B. *Mater. Sci. Eng. B* **1996**, *39* (2), 95.

(51) Hosono, H.; Ogo, Y.; Yanagi, H.; Kamiya, T. *Electrochem. Solid-State Lett.* **2011**, *14* (1), H13.

(52) Ogo, Y.; Hiramatsu, H.; Nomura, K.; Yanagi, H.; Kamiya, T.; Hirano, M.; Hosono, H. *Appl.*

Phys. Lett. **2008**, *93* (3), 032113.

(53) P. Allen, J.; O. Scanlon, D.; J. Piper, L. F.; W. Watson, G. *J. Mater. Chem. C* **2013**, *1* (48), 8194.

(54) Watson, G. W.; Parker, S. C.; Kresse, G. *Phys. Rev. B* **1999**, *59* (13), 8481.

(55) Kolinko, M. I. *J. Phys. Condens. Matter* **1994**, *6* (1), 183.

(56) Gao, W.; Gao, X.; Abtew, T. A.; Sun, Y.-Y.; Zhang, S.; Zhang, P. *Phys. Rev. B* **2016**, *93* (8), 085202.

(57) Mizoguchi, H.; Kamiya, T.; Matsuishi, S.; Hosono, H. *Nat. Commun.* **2011**, *2*, 470.

(58) Hughbanks, T. *J. Am. Chem. Soc.* **1985**, *107* (24), 6851.

(59) Mizoguchi, H.; Hirano, M.; Fujitsu, S.; Takeuchi, T.; Ueda, K.; Hosono, H. *Appl. Phys. Lett.* **2002**, *80* (7), 1207.

(60) Mansourian-Hadavi, N.; Wansom, S.; Perry, N. H.; Nagaraja, A. R.; Mason, T. O.; Ye, L.; Freeman, A. J. *Phys. Rev. B* **2010**, *81* (7), 075112.

(61) Fortunato, E.; Barquinha, P.; Martins, R. *Adv. Mater.* **2012**, *24* (22), 2945.

(62) Wang, Z.; Nayak, P. K.; Caraveo-Frescas, J. A.; Alshareef, H. N. *Adv. Mater.* **2016**, *28* (20), 3831.

(63) Yu, X.; Marks, T. J.; Facchetti, A. *Nat. Mater.* **2016**, *15* (4), 383.

(64) Van de Walle, C. G.; Neugebauer, J. *J. Appl. Phys.* **2004**, *95* (8), 3851.

(65) Oba, F.; Togo, A.; Tanaka, I.; Paier, J.; Kresse, G. *Phys. Rev. B* **2008**, *77* (24), 245202.

(66) Oba, F.; Choi, M.; Togo, A.; Tanaka, I. *Sci. Technol. Adv. Mater.* **2011**, *12* (3), 034302.

(67) Togo, A.; Oba, F.; Tanaka, I.; Tatsumi, K. *Phys. Rev. B* **2006**, *74* (19), 195128.

(68) Pohl, J.; Albe, K. *Phys. Rev. B* **2013**, *87* (24), 245203.

(69) Hou, Z. F. *Solid State Sci.* **2008**, *10* (11), 1651.

(70) Blucher, J.; Bang, K.; Giessen, B. C. *Mater. Sci. Eng. A* **1989**, *117* (Supplement C), L1.

(71) Mizoguchi, H.; Kawazoe, H.; Hosono, H. *Chem. Mater.* **1996**, *8* (12), 2769.

(72) Zhang, S. B.; Wei, S.-H.; Zunger, A. *J. Appl. Phys.* **1998**, *83* (6), 3192.

(73) Hosono, H. *Jpn. J. Appl. Phys.* **2013**, *52* (9R), 090001.

(74) Geballe, T. H.; Hull, G. W. *Phys. Rev.* **1955**, *98* (4), 940.

(75) Wang, Z.; Wang, S.; Obukhov, S.; Vast, N.; Sjakste, J.; Tyuterev, V.; Mingo, N. *Phys. Rev. B* **2011**, *83* (20), 205208.

(76) Ilegems, M.; Montgomery, H. C. *J. Phys. Chem. Solids* **1973**, *34* (5), 885.

(77) Hurwitz, E. N.; Asghar, M.; Melton, A.; Kucukgok, B.; Su, L.; Orocz, M.; Jamil, M.; Lu, N.; Ferguson, I. T. *J. Electron. Mater.* **2011**, *40* (5), 513.

(78) Walsh, A.; Da Silva, J. L. F.; Wei, S.-H.; Körber, C.; Klein, A.; Piper, L. F. J.; DeMasi, A.; Smith, K. E.; Panaccione, G.; Torelli, P.; Payne, D. J.; Bourlange, A.; Egdell, R. G. *Phys. Rev. Lett.* **2008**, *100* (16), 167402.

(79) Preissler, N.; Bierwagen, O.; Ramu, A. T.; Speck, J. S. *Phys. Rev. B* **2013**, *88* (8), 085305.

(80) Samson, S.; Fonstad, C. G. *J. Appl. Phys.* **1973**, *44* (10), 4618.
(81) Marley, J. A.; Dockerty, R. C. *Phys. Rev.* **1965**, *140* (1A), A304.
(82) Ueda, K.; Hiramatsu, H.; Hirano, M.; Kamiya, T.; Hosono, H. *Thin Solid Films* **2006**, *496* (1), 8.
(83) Hiramatsu, H.; Ueda, K.; Ohta, H.; Orita, M.; Hirano, M.; Hosono, H. *Appl. Phys. Lett.* **2002**, *81* (4), 598.
(84) Zhang, S. B.; Wei, S.-H.; Zunger, A. *J. Appl. Phys.* **1998**, *83* (6), 3192.
(85) Neumann, H.; Hörig, W.; Reccius, E.; Möller, W.; Kühn, G. *Solid State Commun.* **1978**, *27* (4), 449.
(86) Hörig, W.; Neumann, H.; Sobotta, H.; Schumann, B.; Kühn, G. *Thin Solid Films* **1978**, *48* (1), 67.
(87) Wasim, S. M. *Sol. Cells* **1986**, *16* (Supplement C), 289.
(88) Zakutayev, A.; Caskey, C. M.; Fioretti, A. N.; Ginley, D. S.; Vidal, J.; Stevanovic, V.; Tea, E.; Lany, S. *J. Phys. Chem. Lett.* **2014**, *5* (7), 1117.
(89) Králik, B.; Chang, E. K.; Louie, S. G. *Phys. Rev. B* **1998**, *57* (12), 7027.
(90) Moustafa, M.; Zandt, T.; Janowitz, C.; Manzke, R. *Phys. Rev. B* **2009**, *80* (3), 035206.

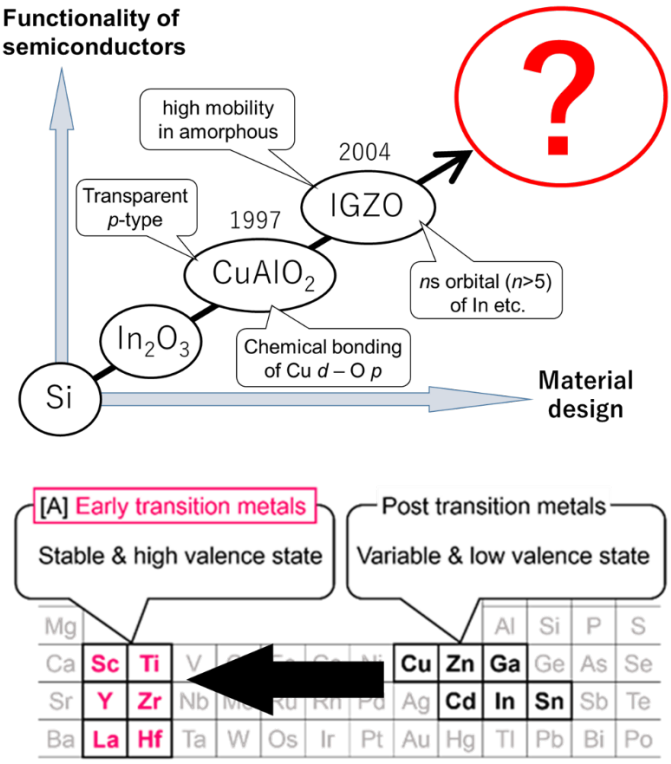

Figure 1. History of design for wide-gap semiconductors. In 1997, the novel design of semiconductors based on Cu^{1+} have been proposed and created wide-gap *p*-type oxides, where previous materials cannot contribute. In 2004, it is reported that the excellent high electron mobility is realized in amorphous In-Ga-Zn-O (IGZO) system. These properties are based on the novel material design, as described in text. Most of the previous wide-gap semiconductors have been composed of post transition metals or *p*-block elements. In this study, early transition metals (*e*TMs) are adopted to prevent the defects. The property of *e*TMs will provide the efficient electron dopability and the high stability of their compounds to carrier doping.

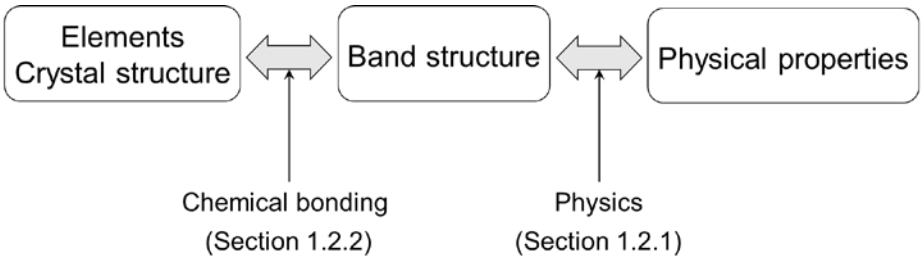

Figure 2. Bridge between constituent elements and crystal structure, electronic structure, and physical properties of semiconductors. Elements and crystal structure must be chosen to obtain electronic structure suitable for desired functionality.

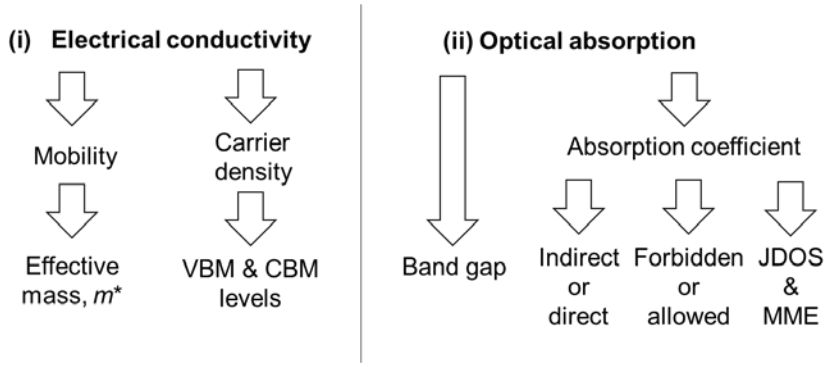

Figure 3. Factors of band structure for physical properties of semiconductors

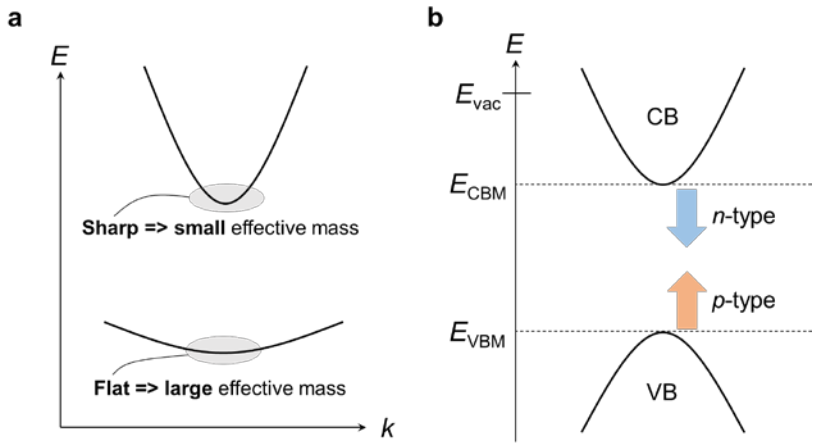

Figure 4. Schematic of band structure related to electrical transport properties. **a.** Relationship between band curvature and effective mass. **b**. Relationship between energy levels of CBM and VBM and carrier dopability.

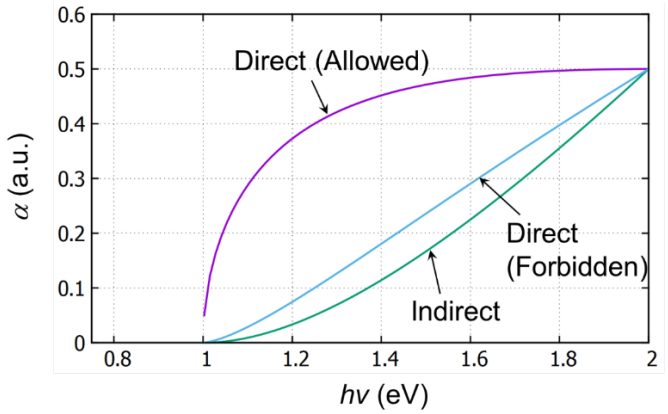

Figure 5. Schematic absorption spectrum around edge (E_g = 1 eV). This spectrum plots $\alpha = (h\nu\text{-}1)^n/h\nu$ with n = 2, 3/2, and 1/2 for Direct(Allowed), Direct(Forbidden), and Indirect, respectively.

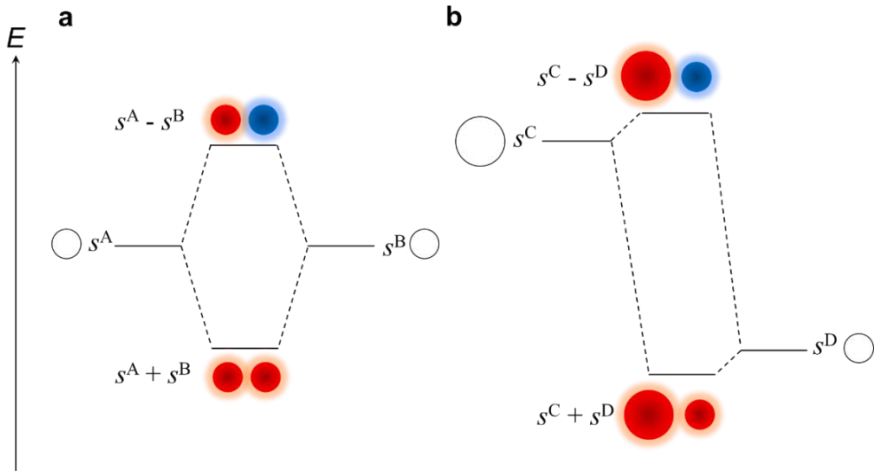

Figure 6. Molecular orbital diagram of two atomic orbitals with equal (a) and different (b) polarity. Red and blue circles represent the positive and negative phases of *s* orbital, respectively.

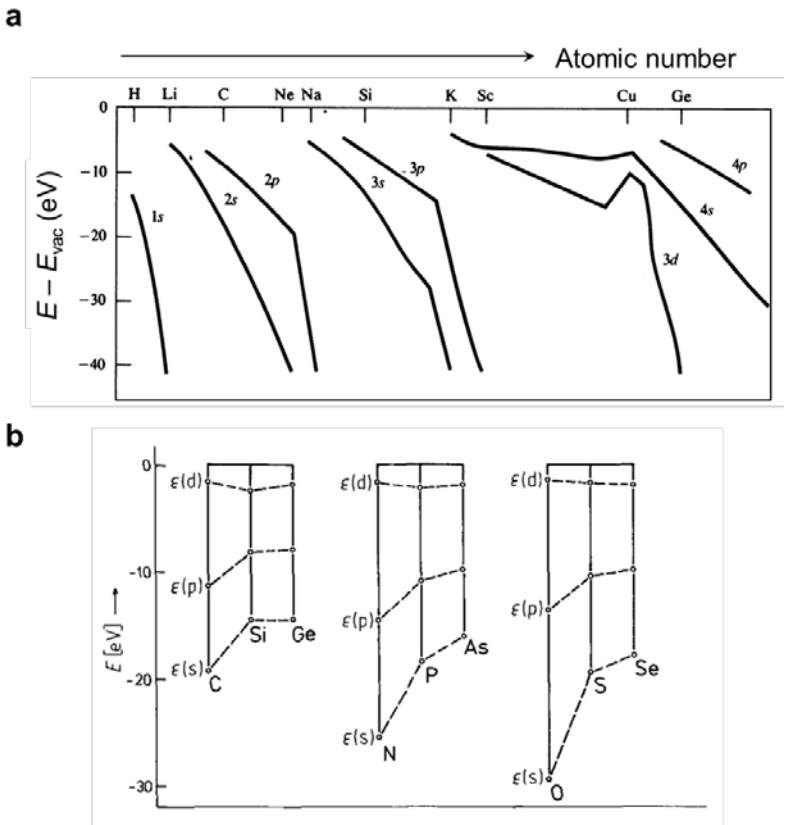

Figure 7. Energy level of atomic orbitals as a function of atomic number (a) and period (b). The figures of (a) and (b) refers to references 24 and 25, respectively.

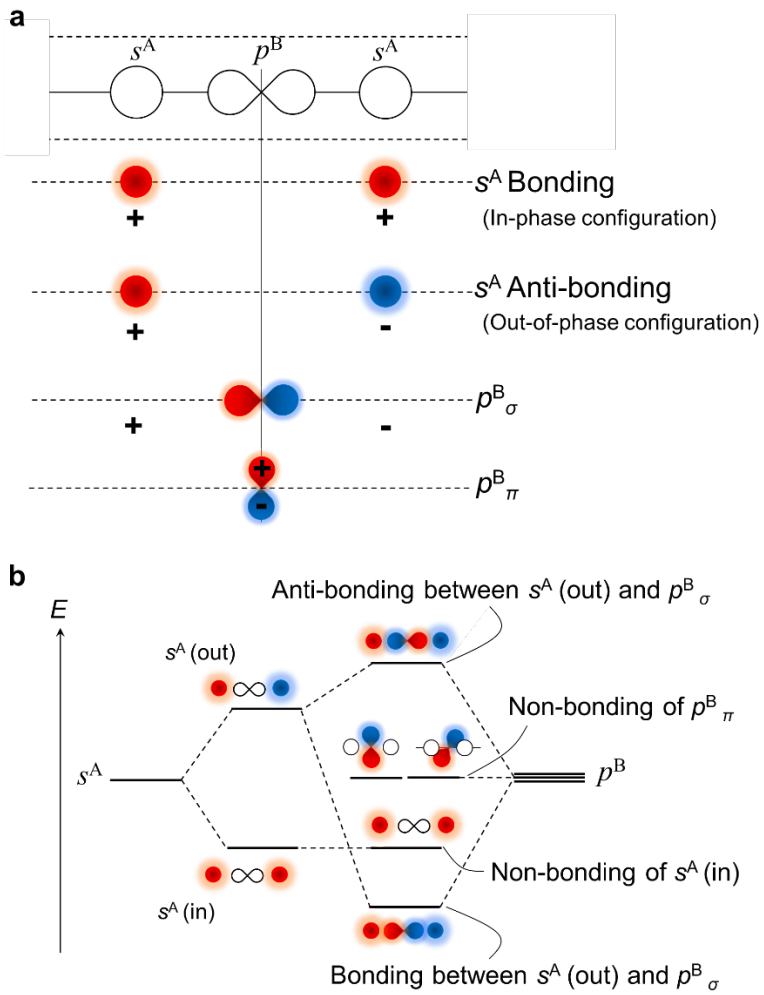

Figure 8. Real space location (a) and its molecular orbital diagram (b) for chain structure composed of two *s* orbitals and one *p* orbital in unit cell. The s^A(in) and s^A(out) represent the in-phase and out-of-phase configurations, respectively.

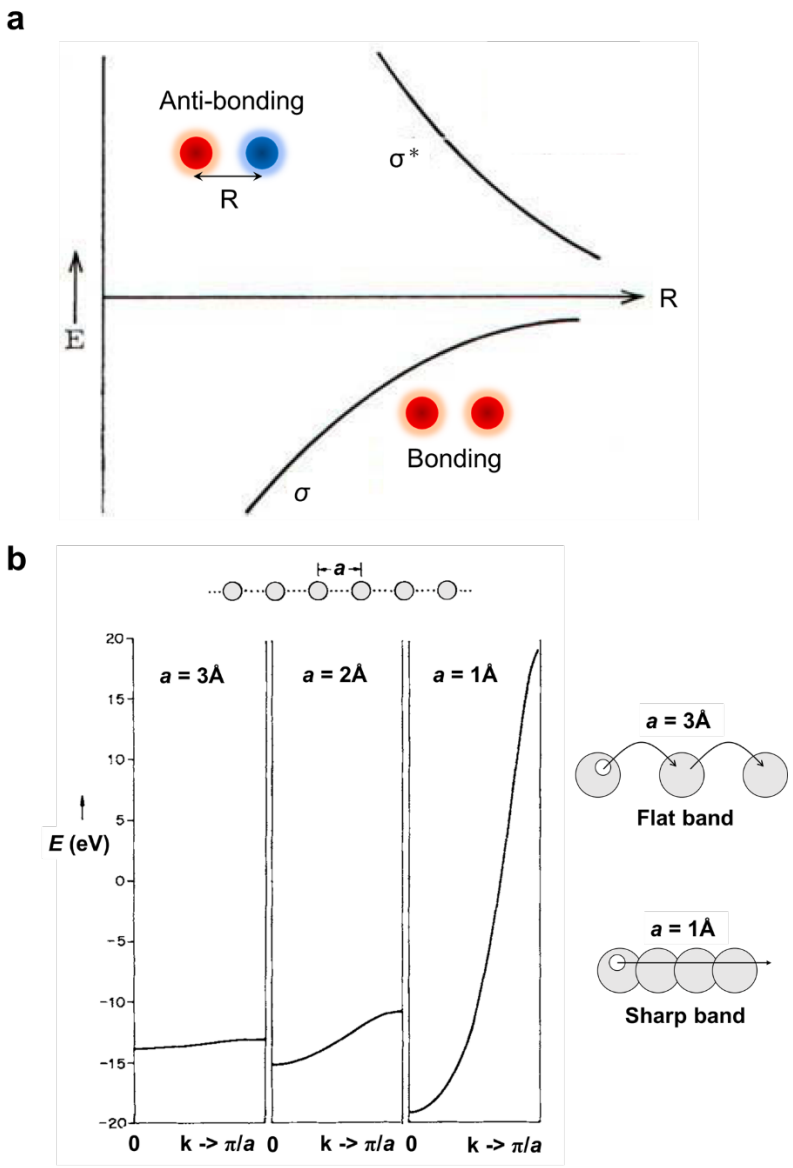

Figure 9. Energy separation derived from chemical bonding between hydrogen atoms. **a**. The energy of bonding and anti-bonding state between two hydrogens as a function of H-H distance. **b**. The band width of hydrogen chain with distances of 3, 2, and 1Å to nearest atoms. Right figure shows the electron road in the case of a = 3Å and 1Å. White and grew bolls represents electron and H 1*s* orbital, respectively. The figures of (a) and (b) refer to reference 23 and 27, reapectively.

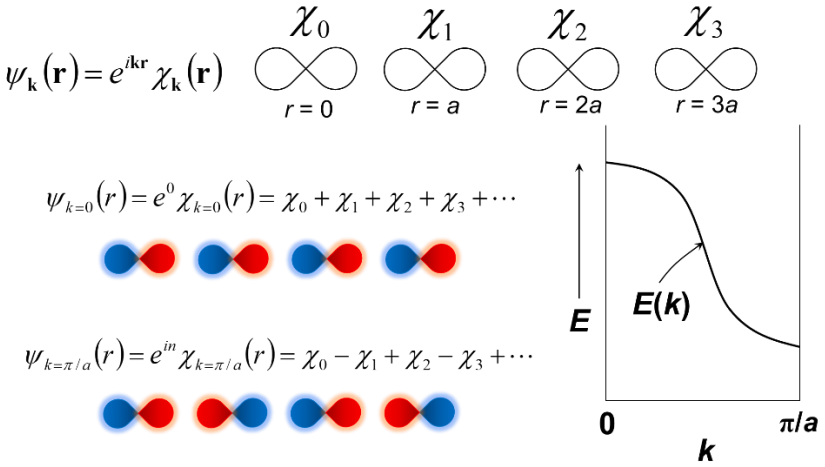

Figure 10. Chemical bonding state dependent on *k* space. The chain structure of *p* orbitals with lattice constant *a* is introduced. At $k = 0$ (Γ point), the periodical phase factor $e^{i\mathbf{kr}}$ is 1 with constant. At $k = \pi/a$ (X point), $e^{i\mathbf{kr}}$ is $(-1)^n$ at $r = na$. The orbital phase of neighboring *p* orbital is periodically inverted. Bonding state appear at $k = \pi/a$, decreasing energy level.

a

D_{4h}	A_{1g}	A_{1u}	A_{2g}	A_{2u}	B_{1g}	B_{1u}	B_{2g}	B_{2u}	E_u	E_g
A_{1g}	A_{1g}	A_{1u}	A_{2g}	A_{2u}	B_{1g}	B_{1u}	B_{2g}	B_{2u}	E_u	E_g
A_{1u}		A_{1g}	A_{2u}	A_{2g}	B_{1u}	B_{1g}	B_{2u}	B_{2g}	E_g	E_u
A_{2g}			A_{1g}	A_{1u}	B_{2g}	B_{2u}	B_{1g}	B_{1u}	E_u	E_g
A_{2u}				A_{1g}	B_{2u}	B_{2g}	B_{1u}	B_{1g}	E_g	E_u
B_{1g}					A_{1g}	A_{1u}	A_{2g}	A_{2u}	E_u	E_g
B_{1u}						A_{1g}	A_{2u}	A_{2g}	E_g	E_u
B_{2g}							A_{1g}	A_{1u}	E_u	E_g
B_{2u}								A_{1g}	E_g	E_u
E_u									$A_{1g}+A_{2g}+B_{1g}+B_{2g}$	$A_{1u}+A_{2u}+B_{1u}+B_{2u}$
E_g										$A_{1g}+A_{2g}+B_{1g}+B_{2g}$

b

D_{2d}	A_1	A_2	B_1	B_2	E
A_1	A_1	A_2	B_1	B_2	E
A_2		A_1	B_2	B_1	E
B_1			A_1	A_2	E
B_2				A_1	E
E					$A_1+A_2+B_1+B_2$

Figure 11. Multiplication table of Irrep for the group D_{4h} (4/mmm) and D_{2d} (-42m) to show selection rule. This matrix denotes the direct product between band states having a row of Irrep and a column of Irrep (e.g., $B_{1g} \otimes A_{1u} = B_{1u}$ in D_{4h}). This matrix M_{ij} is symmetric: $M_{ij} = M_{ji}$, so that the below left panels are not shown. The Irrep of p_x (p_y) and p_z polarizations of the light are A_{2u} and E_u in D_{4h} group, respectively. And the Irrep of p_x (p_y) and p_z polarizations of the light are B_2 and E in D_{2d} group, respectively. Blue and orange colors represent the direct products with the allowed transition by the p_x (p_y) and p_z polarizations of the light, respectively. For example, in D_{4h}, the transition between E_u and A_{2g} is allowed only with the p_x (p_y) polarization and the transition between E_u and B_{2u} is forbidden even with any polarization of light.

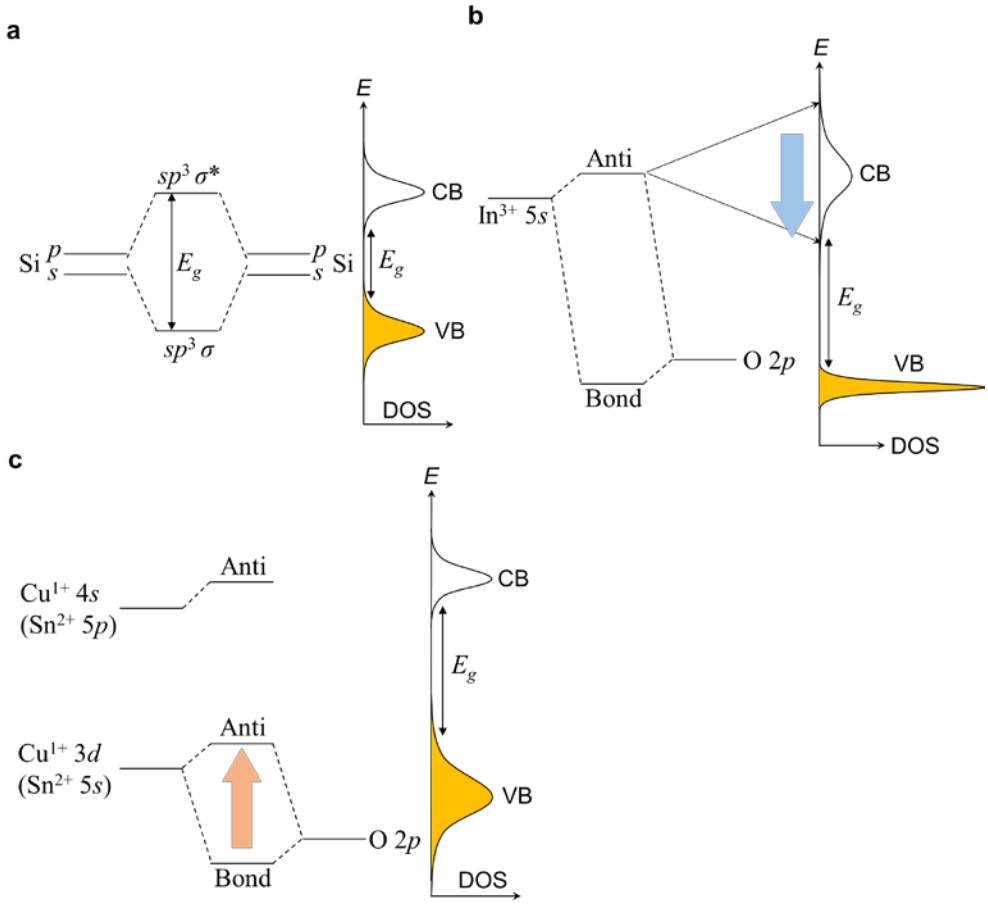

Figure 12. Orbital diagrams and electronic structures of Si (a), In_2O_3 (b), and Cu_2O (c). The origin of bandgap for Si is the difference in energy between bonding and anti-bonding. On the other hand, the ionic semiconductor such as In_2O_3 possesses wide bandgap derived from the difference in polarity between cation and anion. Additionally, a large overlap of In 5*s* orbital leads to broad band width (DOS), resulting in deep CBM and small effective mass of electron. In (c), electronic structure of Cu_2O is introduced as representative of Cu^{1+} (Sn^{2+}) based ionic semiconductor. Anti-bonding character occur between Cu 3*d* and O2*p* orbitals, resulting in the shallow VBM level and small effective mass of hole.

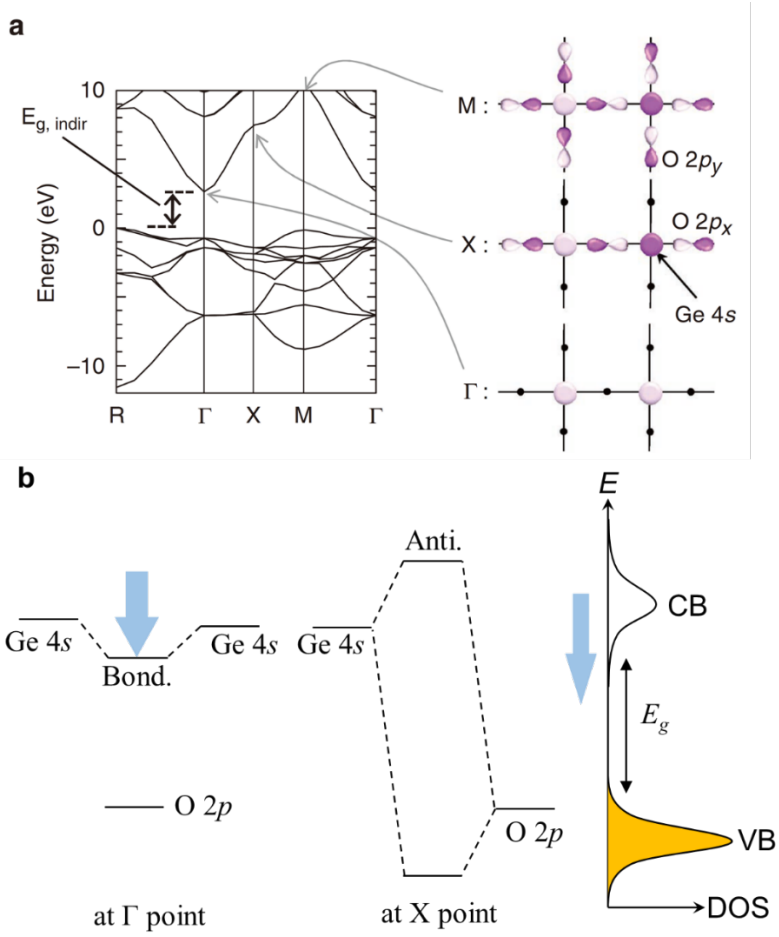

Figure 13. Electronic structure[57], chemical bonding picture[57], and orbital diagram for $SrGeO_3$. At Γ point, Ge 4*s* orbital can't interact with O 2*p* orbitals owing to local structure and periodicity. The CBM state is perfectly composed of Ge 4*s* orbital bonding with nearest Ge 4*s* orbital. This chemical bonding nature is useful to deepen the CBM state. On the other hand, except for Γ point, the anti-bonding between Ge and O appear, resulting in the sharp curvature of conduction band.

Table 1. Electrical transport properties of semiconductors representing the electronic structure shown in section 1.2.3. E_g, σ, μ, n, and S represent bandgap, electrical conductivity, mobility, carrier concentration, and Seebeck coefficient, respectively. CIS and CGS stand for $CuInSe_2$ and $CuGaSe_2$, respectively.

Material	**Carrier polarity**	***E*g (eV)**	**σ (S/cm)**	**μ (cm^2/Vs)**	***n*** **(cm^{-3})**	***S*** **(μV/K)**
Si	bipolar	1.1 (indirect)		*n*: 1450 [22]	10^{17} [74,75]	-600 [74,75]
GaN	bipolar	3.4 (direct)		*n*: 440 [76]	10^{16} [77]	-300 [77]
In_2O_3	*n*	2.9 (forbidden) [78]		*n*: 50-250 [79]	10^{19} [79]	-200 [79]
SnO_2	*n*	3.5 [80]		*n*: 50-200 [81]	10^{16} - 10^{17} [81]	-200 [81]
$CuAlO_2$	*p*	3.5 [7]	1 [7]	*p*: 10.4 [7]	1.3×10^{17} [7]	+183 [7]
LaCuOS	*p*	3.1 [82]	0.7 [83]	*p*: 0.5 [83]	10^{19} [83]	+200 [83]
$Cu(In,Ga)Se_2$	*p* (E_g > 1.2)[84] bipolar (< 1.2)[84]	CGS: 1.62 [85] CIS: 1.0 [86]		*p*: 50-500 (CIS) [87]		
$CuInO_2$	bipolar	1.2 (forbidden) [42]	2.8×10^{-3} [41]			+480 [41]
Cu_3N	bipolar	1.2 (indirect) [88]	0.1 [88]	*p*: 1-10 [88]	10^{16} - 10^{17} [88]	+200 [88]
SnO	bipolar	0.6 (indirect) [52] 2.9 (direct) [52]		*p*: 2 [51]	2×10^{17} [51]	+479 [51]
$SrGeO_3$	*n*	3.45 (direct) [57]	5 [57]	*n*: 11.6 [57]	2.2×10^{20} [57]	-10 [57]
$ZnRh_2O_4$	*p*	2 [59]	1 [59]			+140 [59]
TaIrGe	*p*	3.36 (direct) [14]	0.5 [14]	*p*: 2730 [14]	0.8×10^{15} [14]	+82 [14]

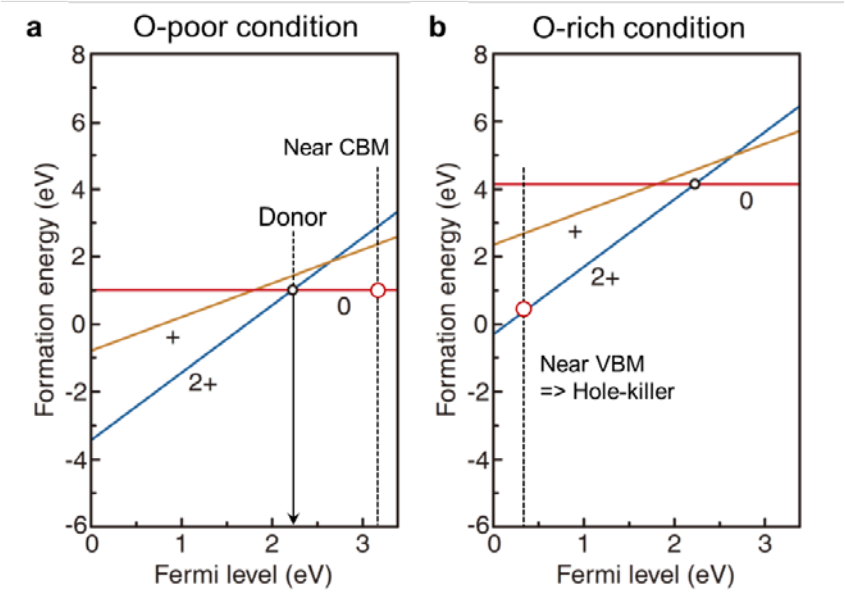

Figure 14. Formation energies of the O vacancy in neutral, +, and 2+ charge states in ZnO as a function of the Fermi level, obtained using the HSE hybrid functional[66]. **a.** O-poor (Zn-rich) limit. **b.** O-rich (Zn-poor) limit.

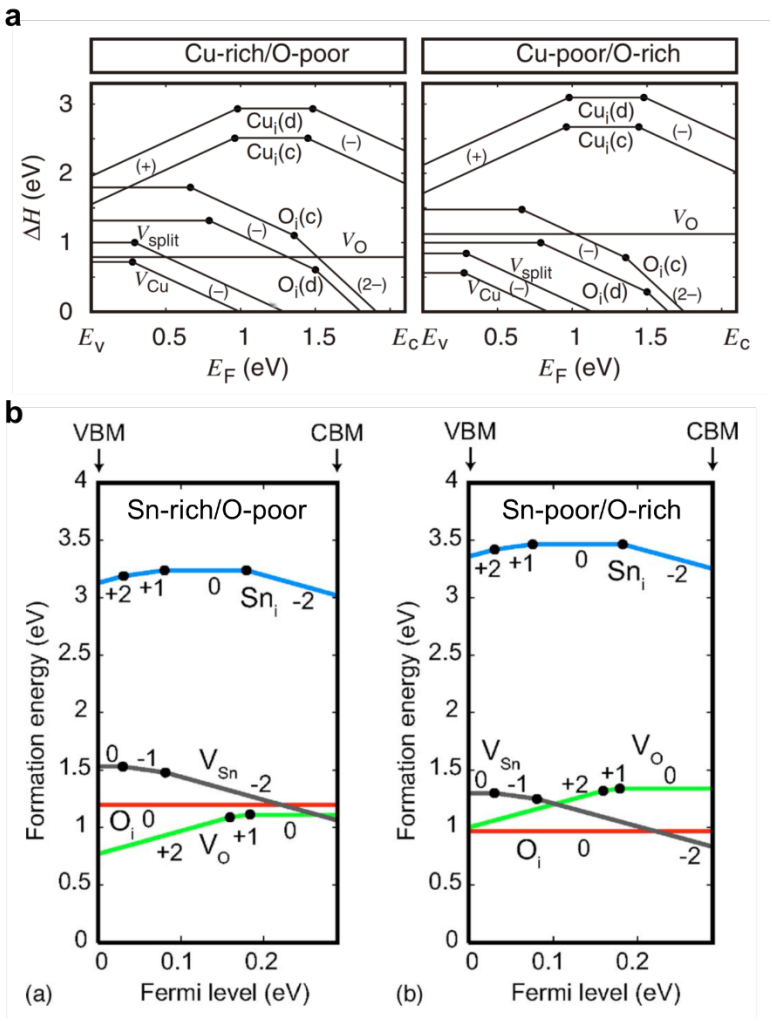

Figure 15. Formation enegies of defects in Cu_2O (a) and SnO (b) as a function of Fermi level. **a.** Case of Cu_2O in Cu-rich/O-poor and Cu-poor/O-rich conditions[9]. **b.** Case of SnO in Sn-rich and O-rich limits[67]. Ionization level are indicated with a dot.

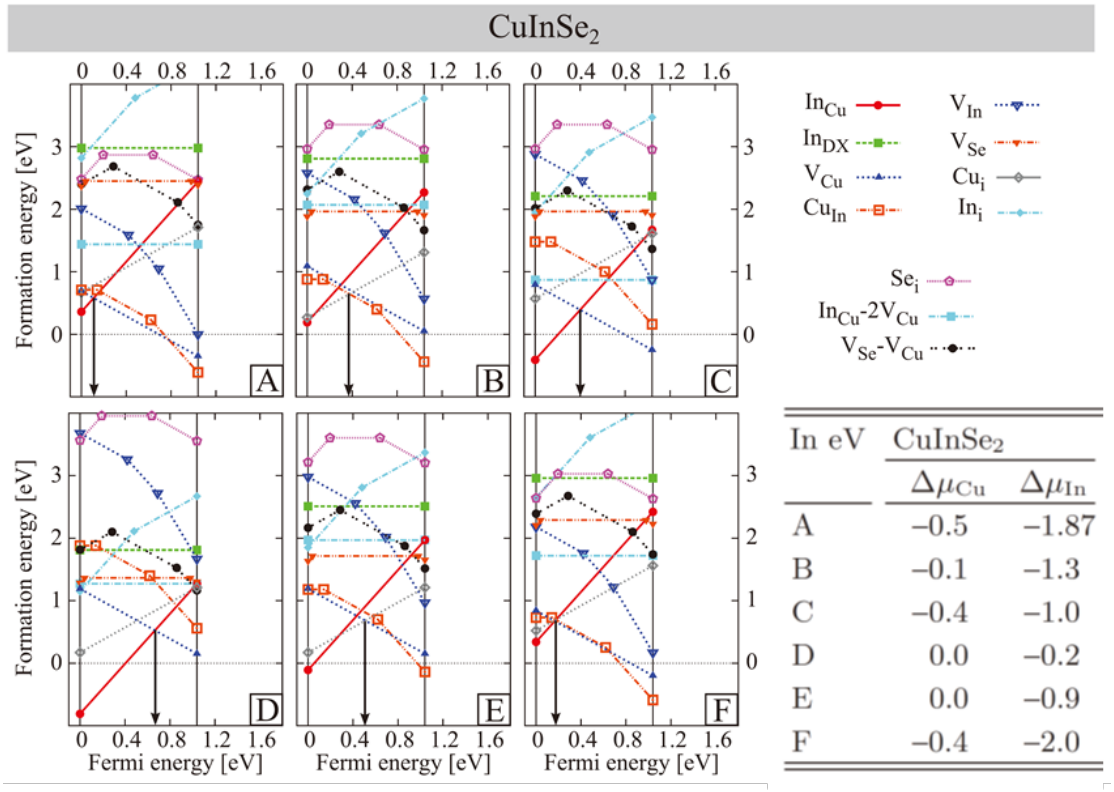

In eV	$CuInSe_2$	
	$\Delta\mu_{Cu}$	$\Delta\mu_{In}$
A	−0.5	−1.87
B	−0.1	−1.3
C	−0.4	−1.0
D	0.0	−0.2
E	0.0	−0.9
F	−0.4	−2.0

Figure 16. Defect formation energy in $CuInSe_2$ for various condition (chemical potential shown in right below) as a function of Fermi level[68]. Each ionization energies are indicated with points having the color and shape indicated in right above.

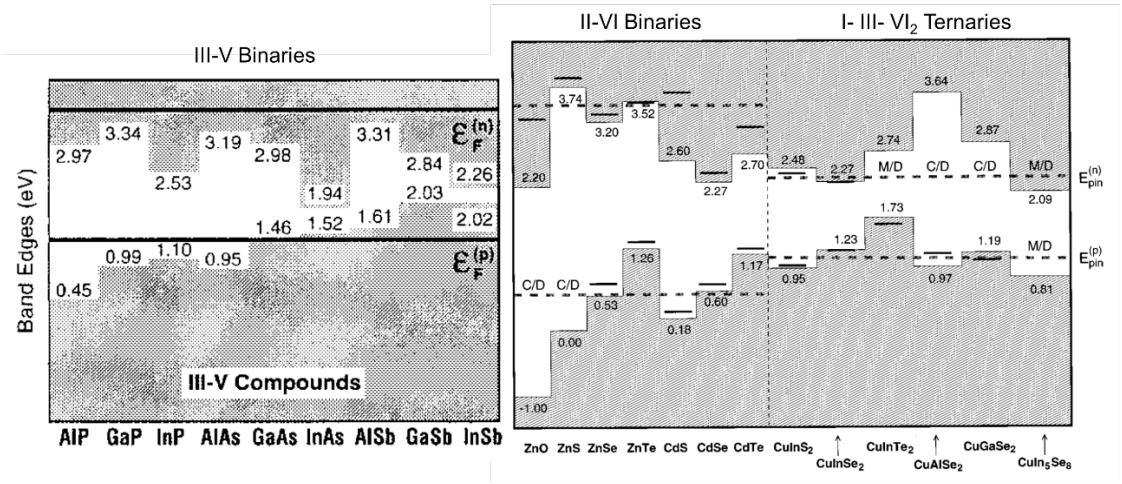

Figure 17. Empirical carrier doping limit relative to the energy of VBM and CBM levels for III-V[21], II-VI[72], and I-III-VI_2[72] compounds. The *n*-type pinning energy, $\varepsilon_F^{(n)}$ and $E_{pin}^{(n)}$, and *p*-type pinning energy, $\varepsilon_F^{(p)}$ and $E_{pin}^{(p)}$, are indicated.

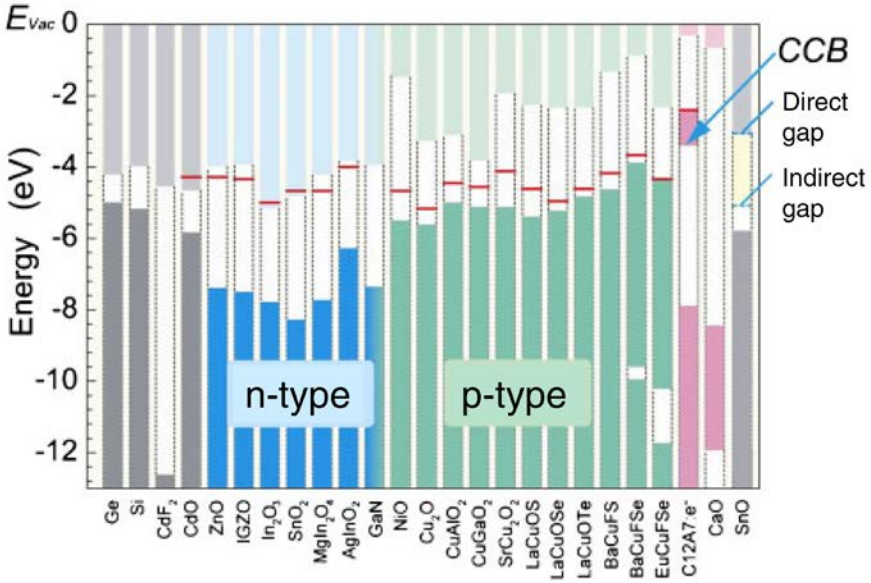

Figure 18. Band alignment of oxides and chalcogenides semiconductors and related materials[73]. Solid red line represents the Fermi level of measured samples.

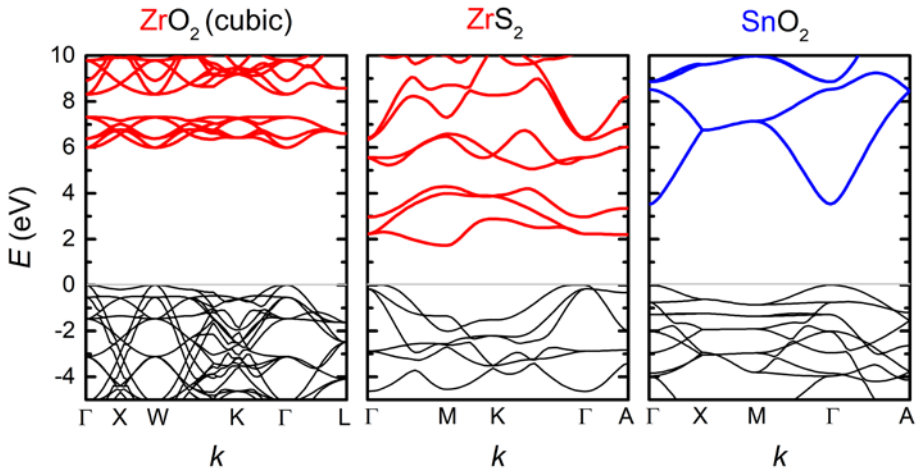

Figure 19. Comparison of band structures between ZrO_2 (cubic), ZrS_2, and SnO_2. Red and blue colors in band represent conduction band for Zr and Sn based semiconductors, respectively. These bandgap values refer to experimental values; ~6 eV for ZrO_2[89], ~1.7 eV for ZrS_2[90], and ~3.5 eV for SnO_2[80].

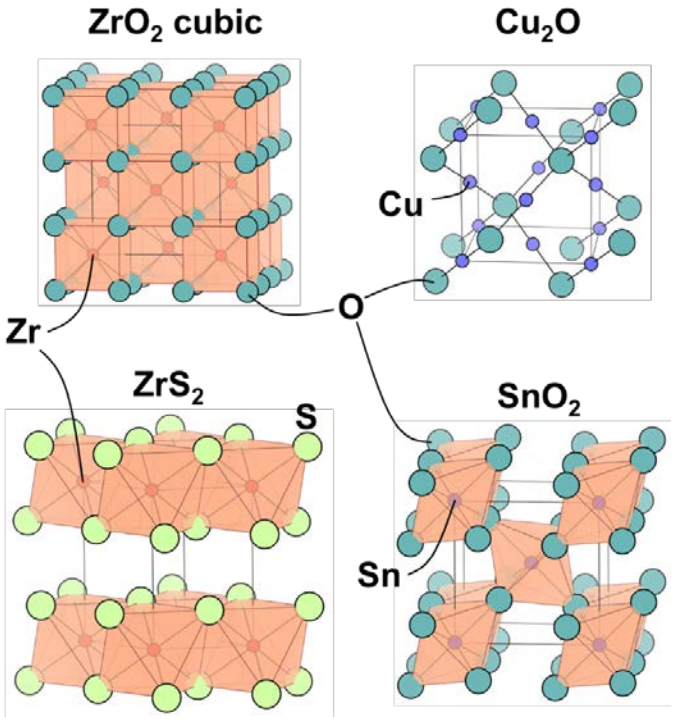

Figure 20. Crystal structures of ZrO_2 (cubic), ZrS_2, Cu_2O, and SnO_2. Light blue, blue, red, grew, and light yellow spheres represent Cu, Sn, Zr, O, and S, respectively. The coordination numbers of cations are 8 for ZrO_2, 6 for ZrS_2, 2 for Cu_2O, and 6 for SnO_2.

Chapter 2. Design of transparent bipolar semiconductor: ZrOS

2.1 Introduction

Strategy to design transparent bipolar semiconductors (TBSCs), tetragonal phase of ZrOS, is described in this chapter. TBSCs play an important role in next-generation optoelectronic devices and flexible displays. However, designing TBSCs is fundamentally difficult because of a dilemma between optical transparency and bipolar nature.

As described in chapter 1, carrier doping requires that stability of carrier is higher than that of point defects. The stability of cation vacancy formation decreases by using early transition metals (*e*TM) inducing crystal structure with high coordination number. On the other hand, improvement in the carrier stability requires to make CBM deep and VBM shallow relative to vacuum level. Deep CBM and shallow VBM are satisfied by designing chemical bonding of cation and anion. Finally, a direct forbidden bandgap keeps the optical transparency. Three guidelines result in tetragonal phase of ZrOS. This material design is summarized in **Figure 1**.

Tetragonal ZrOS is the first *e*TM based bipolar semiconductor and demonstrates the potential of semiconductor based on *e*TMs. This material opens up a frontier to the functional semiconductor based on *e*TMs.

2.2 Material design

Early transition metals to improve carrier dopability

Early transition metal (*e*TM) cations, such as Y^{3+}, La^{3+}, Zr^{4+}, and Hf^{4+}, are chosen as constituents to improve carrier dopability. Previous semiconductors based on post transition metals (*p*TM) have suffered from a poor doping efficiency originating from the

low formation energy of a metal-vacancy and a facile valence change between two stable valence states, for example, $Sn^{2+} \leftrightarrow Sn^{4+} + 2e^{-}$ and $Cu^{1+} \leftrightarrow Cu^{2+} + e^{-}$, as described in section 1.3. However, contrary to the *p*TM ions, *e*TM cations occupy a high coordination numbers (CN) site and form a single stable ionic compound owing to their high and single valence states, which prevents the formation of a cation vacancy and a valence change in their compounds.

However, these *e*TM elements are yet to attract interest as a constituent of the *n*- and *p*-type semiconductors. Unlike the *p*TM compounds, the relatively localized *d* orbital of *e*TM compounds forms a shallow CBM level, and the *e*TM has no appropriate orbitals making the VBM level shallower, which contrasts with the 3*d* orbital of Cu^{1+} or 5*s* orbital of Sn^{2+}. Therefore, semiconductors with high carrier controllability based on *e*TM have not reported so far. To solve the problematic band alignment of *eTM* compounds, the chemical bonding state is designed to form an electronic structure suitable for both *n*- and *p*-doping.

Non-bonding state for n-type

To deepen the CBM, introducing a non-bonding state between cation and anion would be effective, while an anti-bonding state between anions will increase the VBM (strategy [B]). Basically, the conduction band (CB) and the valence band (VB) of conventional semiconductors are, respectively, composed of anti-bonding and bonding states between the unoccupied orbitals of the metal and the occupied orbital of the anion, as shown in Figure 1b (left). If the nonbonding state is introduced to the CB at a specific *k* point, the energy level at the *k* point decreases, and the effective electron mass is reduced owing to the large energy difference between the deep nonbonding and the shallow antibonding

states (see the right of Figure 1b)[1], as described in SrGeO3 of section 1.2.3.

How can we explore non-bonding state? Generally, non-bonding state appears between relevant orbitals with a different irreducible representation (Irrep). The Irrep of orbital is characterized by a space group, an atomic site symmetry, a character of electron orbitals, and *k* point in reciprocal space, as described in Irrep of section 1.2.2. In principle, the number of Irrep in point group is equal to its number of symmetry operations. As the point group is classified as the higher symmetry (*i.e.*, D_{2h}, D_{4h}, D_{6h}, and O_h), the number of Irrep is increased, and thus relevant orbitals in its point group tend to be classified as a different Irrep. Furthermore, the class of Irrep is determined with the character of electron orbital and the atomic site symmetry. For example, *s* orbital on a site of multiplicity one is the totally symmetric state (*i.e.*, A_1 or A_{1g}), whereas in the case of a site of multiplicity two where the electron orbitals are allowed to form in-phase and out-of-phase configurations in the unit cell, the out-of-phase configuration of *s* orbitals on such site can be the state with no inversion symmetry. Considering above mentions, the non-bonding state often appears between relevant orbitals in the high symmetry point groups, with the different orbital character (*s*, *p*, or *d* orbital) and on the low multiplicity site. Some related examples are shown in appendix.

Enhancement of anti-bonding for p-type

The anti-bonding between anions, which increases the energy level of the VBM, is an analogy of the cation-anion antibonding that is evident in Cu^{1+} and Sn^{2+}-based materials. Generally, as an anion has a larger ionic radius and are less ionic (*e.g.*, from oxygen to tellurium in group 4), the energy levels of the *p* orbitals are increased, which, in turn, results in a shallow VBM (energy levels described in section 1.2.2).[2] Therefore,

chalcogenide ions are more suitable for hole conduction than an oxide ion. Moreover, a short separation between neighboring anions is critical because the stronger interaction between these anions' *p* orbitals raises the VBM derived from the anion-anion anti-bonding level and enhances the band dispersion (analogy of short separated H-chain as seen in section 1.2.2).

Forbidden transition for optical transparency

Finally, it is desirable to keep the visible transparency of the semiconductor with a deep CBM and shallow VBM resulting in a narrow bandgap, empirically, below ~2 eV.[3] Thus, semiconductors that have a direct allowed type band-to-band transition are eliminated as candidate materials. The low absorption coefficient in the energy range of visible light is sufficient for practical thin film applications. Thus, candidate materials must have an indirect or direct forbidden-type band-to-band transition (strategy [C]) (see section 1.2.1 and selection rule for band structure of section 1.2.2).

2.3 Candidate Material

Tetragonal ZrOS (*t*-ZrOS) is proposed as a candidate for TBSCs. The *t*-ZrOS meets the requirements described above; a high coordination number around Zr^{4+} cations preventing the formation of a metal vacancy, a short S-S distance suitable for shallow VBM, and a non-bonding Zr $4d_{x2-y2}$ orbital for a deep CBM.

Crystal structures

Figure 2a shows the crystal structure of *t*-ZrOS and **Table 1** summarizes distances of nearest atoms for ZrOS. Five S and four O atoms are bonded to Zr (below the Figure

2a). The nearest neighbor O-O and S-S bond lengths of 2.51 and 3.02 Å, respectively, are shorter than the summation of each ionic radius at the corresponding sites. This fact suggests a strong interaction between neighboring anion *p* orbitals. For comparison, we also show the crystal structure of cubic ZrOS (*c*-ZrOS) in **Figure 2b**. The structure of *c*-ZrOS is regarded as a distorted fluorite structure, where the Zr-centered polyhedra, ZrO_3S_4, correspond to the Ca-centered cubes, CaF_8, in fluorite. The nearest neighbor Zr-Zr bond length in the *c*-ZrOS of 3.58 Å is comparable with that in *t*-ZrOS (3.52 Å), whereas their O-O and S-S lengths of 3.52 and 3.54 Å, respectively, are significantly longer than those in the tetragonal phase.

Irreducible representation

Table 2 summarizes the irreducible representations (Irrep) of *t*-ZrOS at the Γ point. The *P*4/*nmm* space group of *t*-ZrOS belongs to the high symmetry point group D_{4h}, and, furthermore, the site symmetry of each constituent is high (the low multiplicity), thus is suitable for forming a non-bonding state. Each atomic orbital has two configurations, in-phase and out-of-phase, in the unit cell, and then the Irrep is assigned to each configuration. In principle, the orbitals with the same Irrep can interact with each other. Hence, according to **Table 2**, it is found that the out-of-phase of Zr $4d_{x2-y2}$ and both phases of Zr $4d_{xy}$ form a non-bonding state, that is, they cannot interact with any *p* orbitals of S and O at the Γ point.

2.4 Validation from theoretical calculation

Band structures

Figure 3a and **3b** show the band structures of *t*-ZrOS and *c*-ZrOS, respectively. Here,

the energy level of *c*-ZrOS was aligned to the S 3*s* level of *t*-ZrOS located at $E - E_{VBM}$ ~−12 eV as seen in **Figure 4**. These calculated band structures reveal that the CBM and VBM of *t*-ZrOS are deeper by 2 eV and shallower by 0.7 eV than those of *c*-ZrOS, respectively, yielding the benefit of the emergence of a bipolar nature. The deep CBM at the Γ point purely consists of the out-of-phase configuration of the Zr $4d_{x2-y2}$ orbital. This means that the Zr $4d_{x2-y2}$ orbital forms a non-bonding state, which is consistent with the symmetry analysis based on **Table 2** (This chemical bonding is discussed below.). Away from the Γ point, the Zr $4d_{x2-y2}$ orbital cancels the non-bonding state and eventually forms an anti-bonding state with O 2*p* orbitals at another *k* point, such as the M point, which shapes a highly dispersed band with a small effective mass (m_e* along the Γ-M line is ~0.36m_0, m_0; a free electron mass). In contrast, the CB of *c*-ZrOS is flat and shallow owing to an anti-bonding nature between Zr *d* and anion *p* orbitals at the whole reciprocal space. As for the VB, S $3p_{x/y}$ orbitals of *t*-ZrOS form a shallower and sharper VBM (a light hole effective mass; m_h*(Γ-M) ~ 0.24m_0) relative to that of *c*-ZrOS (a light hole effective mass; m_h*(Γ-M) ~ 0.37m_0). This profound difference in the VB of *t*- and *c*-ZrOS originates from the S-S separation in both phases.

Transition probability

To examine the optical properties, we calculated the matrix elements for direct interband transitions between band edge states. **Figure 3c** and **3d** show the *k* dependences of the transition matrix element (P^2) between the band edge states. They reveal that direct transitions between CBM and VBM at the Γ point are forbidden in *t*-ZrOS because the Irrep of CBM and VBM have the same parity (Γ_{4-} for CBM and Γ_{5-} for VBM).[4] However, in the *c*-ZrOS, the optical transitions at the band edges are allowed at all *k* points (**Figure**

3d).

2.5 Experimental validation

Sample characterization

Figure 5 shows powder X-ray diffraction pattern for *t*-ZrOS (a) and *c*-ZrOS (b). In this figure, impurity phases such as ZrO_2 and ZrS_2 are slightly observed. However, these impurities are electrical insulators and therefore don't work as contaminations for transport measurements. **Figure 6** shows lattice constants as a function of amounts of Y and F doping in *t*-ZrOS. In the case of Y doping, the increase of lattice constants demonstrates the successful doping of yttrium. Additionally, the amounts of yttrium for Y doped *t*-ZrOS are determined by using the electron probe micro analyzer. **Figure 7** shows atomic core levels measured by utilizing hard X-ray photoemission spectroscopy (HAXPES). The observed F 1*s* peak in F doped *t*-ZrOS is direct evidence of F substitution.

Transport properties

Figure 8a and **8b** show the electrical conductivity σ as a function of temperature for yttrium and fluorine-doped *t*-ZrOS (*t*-ZrOS:Y and *t*-ZrOS:F, respectively). The temperature dependences of σ are not largely changed except for small substitution, indicating that acceptor and donor levels are stable to chemical doping. **Figure 8c** and **8d** show the thermoelectric measurements for *t*-ZrOS:Y and *t*-ZrOS:F at room temperature. **Figure 9a** and 9**b** show the doping dependences of σ and S of *t*-ZrOS:Y and *t*-ZrOS:F at room temperature. For the undoped *t*-ZrOS, a much lower conductivity of ~10^{-7} S cm^{-1} was achieved. Once the Y or F was doped, the conductivity was steeply enhanced to 10^{-2} S cm^{-1}, and simultaneously, an inversion of the Seebeck coefficient sign was also

confirmed from *p*-type for *t*-ZrOS:Y to *n*-type for *t*-ZrOS:F. The low conductivity in the undoped sample and the easy controllability of the carrier-polarity in the doped *t*-ZrOS indicate the high formation energy of an atomic vacancy, anti-site, and/or interstitial-site, which is in contrast to the conventional wide-gap semiconductors based on a *pTM* cation. The donor and acceptor levels estimated from the activation energy of the conductivity measurement were 100 meV for the F 2.0 mol% doped sample and 130 meV for the Y 2.2% doped sample as shown in **Figure 10**.

Hard X-ray photoemission spectroscopy

Figure 9c shows the comparison between the hard X-ray photoemission spectrum and the atom-projected density of state (PDOS) for *t*-ZrOS. The observed spectra for the VB agrees well with the calculated electronic structure. Moreover, **Figure 9d**, where 0 eV sets to Fermi level, shows the shift of the band edges with doping, from *t*-ZrOS:Y to *t*-ZrOS:F. The edge of spectra for *t*-ZrOS:Y is near to Fermi level, directly verifying *p*-type semiconductor. Conversely, the observed spectra for *t*-ZrOS:F is located away from the Fermi level, being consistent to *n*-type nature. Additionally, the energy difference in band edge between both spectrum is 1.4 eV, corresponding to the calculated bandgap of 1.5 eV, shown in **Figure 3a**.

Absorption property

Figure 9e and **9f** show the calculated and experimental absorption coefficients α of *t*-ZrOS, respectively. Owing to the direct forbidden transition between the band edge states, the α of *t*-ZrOS is as low as ~10^4 cm^{-1} below 2.5 eV, as shown in **Figure 9e**. Above that, the α is sharply raised at $h\nu$ = 2.5 eV ($E_g^{\text{direct allowed}}$), owing to the direct allowed

transition from the VBM to the second lowest conduction band at the Γ point. The direct forbidden bandgap was experimentally estimated to be 1.5 eV ($E_g^{\text{direct fobbiden}}$) from the $(h\nu\alpha/s)^{2/3}$ plot in **Figure 9f**, which is consistent with the calculated bandgap and the energy shift of 1.4 eV, observed in the hard X-ray photoemission measurements.

Band alignment

Figure 11 shows the experimentally determined band alignment of *t*-ZrOS, *c*-ZrOS, and relevant semiconductors. According to an empirical doping rule in ionic semiconductors, the lower limit of the electron affinity (CBM position from the vacuum level ($E_{\text{vac.}}$)) for successful electron-doping is ~−4 eV, while the higher limit of the ionization potential (VBM from the $E_{\text{vac.}}$) for hole-doping is ~−6 eV. Since the CBM and VBM of *t*-ZrOS are located at −4.1 eV and −5.6 eV, respectively, it is evident that the band alignment of *t*-ZrOS is suitable for bipolar conductivity. Note that even though the 3*p* orbitals of sulfur form shallower energy levels compared with the 2*p* orbitals of O, the VBMs of *c*-ZrOS and ZnS are located below the *p*-type doping limit, which supports that the strong interaction between neighboring anions plays a vital role to increase the VBM level. This result demonstrates that the short anion-anion separation will be a new way to raise the VBM without *pTM* cations, such as Cu^{1+} and Sn^{2+}.

2.6 Discussion

Symmetry analysis for optical transition

The selection rule of a interband transition of a band structure is derived from a triple direct product among an initial state, a final state, and a direction of polarity of electromagnetic radiation. When the triple direct product includes the totally symmetric

representation (A_1 and A_{1g}), its transition is allowed. In the case of tetragonal ZrOS (*t*-ZrOS) which is classified as the D_{4h} group, the Irrep of the CBM and VBM states are respectively represented as B_{2u} (G_{4-}) and E_u (G_{5-}), and the Irrep of p_x (p_y) and p_z polarizations of the light are classified as E_u and A_{2u}, respectively. The triple direct products of the transition between the CBM and the VBM for *t*-ZrOS can be written as

$$B_{2u} \otimes E_u \otimes E_u = E_g \otimes E_u = A_{1u} + A_{2u} + B_{1u} + B_{2u} \quad (1)$$

$$B_{2u} \otimes E_u \otimes A_{2u} = E_g \otimes A_{2u} = E_u \quad (2)$$

for the p_x (p_y) (1) and p_z (2) polarizations of the light. Both results don't include the totally symmetric class A_{1g} and the interband transition is therefore forbidden.

Energy level and orbital symmetry in t-ZrOS

Both orbitals of Zr $4d_{x2-y2}$ and $4d_{xy}$ in *t*-ZrOS don't interact any anion *p* orbitals due to its local symmetry. Why is the CBM state composed of Zr $4d_{x2-y2}$, not Zr $4d_{xy}$ orbitals? **Figures 14d** shows the chemical bonding picture of CBM state completely constituted from the out-of-phase configuration of Zr $4d_{x2-y2}$ orbital. The translational symmetry at the Γ point results in a σ bonding between associated orbitals. However, nearest Zr $4d_{x2-y2}$ orbital correlates as δ-like bonding of corresponding orbitals, resulting in little benefit to deepen CBM state because of the δ-like bonding. **Figure 14e** represents 2nd lowest conduction band composed of the in-phase configuration of Zr $4d_{xy}$ orbitals. The d_{xy} orbital is rotated 45 degrees from the d_{x2-y2} orbital. Therefore, the σ bonding seen in the d_{x2-y2} orbital disappears at the d_{xy} orbital, resulting in a shallow CB. As a summary, the origin, where the CBM is formed by the out-of-phase configuration of Zr $4d_{x2-y2}$ orbital, is σ bonding with orbitals of nearest unit cells.

Additionally, **Figures 15a** and **15b** show the contribution of various orbitals in the

CB and VB, respectively. The large contribution of Zr 4d_{x2-y2} appears at the Γ point of the CB without that of any anion *p* orbitals. This represents non-bonding state. However, leaving from the Γ point, the Zr 4d_{x2-y2} orbital becomes gradually small in contribution and finally forms the anti-bonding with the 2$p_{x,y}$ orbital of O at the M point. **Figures 15c** and **15d** show the chemical bonding pictures of anti-bonding between the Zr 4d_{x2-y2} and O 2p_x at the M point. These two states are degenerate from the viewpoint of chemical bonding and band structure. At the M point, the phase of Zr 4d_{x2-y2} orbital is inverted in the nearest unit cells, resulting in overlap of negative and positive phases between Zr and O. In **Figure 15b**, the VBM is mainly contributed from short separated S 3$p_{x,y}$ orbitals. Similar to the CB, the chemical bonding largely varies depending on the *k* point, resulting in the wide band width. Therefore, crystal structure, where the chemical bonding state changes with the *k* point, is useful for improving the electron transport property.

2.7 Conclusion

In conclusion, a novel design concept for transparent bipolar semiconductors is proposed. The essential difference from the bipolar semiconductors reported so far is to use an early transition metal, rather than a post-transition metal. The effectiveness of this approach was demonstrated through experiments and calculations of tetragonal ZrOS with a non-bonding Zr *d* orbital and a short S-S separation. This material has an appropriate direct forbidden-type bandgap (~2.5 eV) and exhibits clear bipolarity upon substitutional doping.

2.8 Appendix

Emergence of mid-gap state in c-ZrOS

Figure 16 shows experimental data and schematic of electronic structure for undoped *c*-ZrOS. These data were obtained from the same sample. The seebeck coefficient is approximately 21 μV/K, indicating a high carrier concentration. Corresponding to it, the electronic conductivity is high value and its temperature dependence is small relative to *t*-ZrOS. However, as shown in Figure 3c, HAXPES demonstrates that the Fermi energy of *c*-ZrOS is located at ~1.5 eV above VBM level. These results indicate that the *p*-type conduction of *c*-ZrOS originates from a mid-gap state in the bandgap.

Some materials composing non-bonding state

Here, some materials forming non-bonding state between cation and anion are introduced. As mentioned above, the non-bonding state often appears when three requirements are satisfied; (1) high symmetry point groups (D_{2h}, D_{4h}, D_{6h}, and O_h), (2) different orbital character (*s*, *p*, or *d* orbital) and (3) low multiplicity components. Additionally, three conditions for exploration are introduced: (4) binary or ternary compounds, (5) *e*TM (Y, Zr, La, and Hf) based semiconductors, and (6) N, S, and Se as anions. Based on these criteria, four materials are discovered (possibly, not completely); hexagonal LaSeF, hexagonal ZrS_2, tetragonal Ba_2ZrS_4, and orthogonal ZrNI as shown in **Tables 3-6**. The hexagonal LaSeF has the unique band edges that both states are composed of non-bonding state between cation and anion. Then, the tetragonal Ba_2ZrS_4 forms the layered perovskite structure whose high symmetry induces non-bonding state of CBM, with an analogy of $SrGeO_3$ (cubic perovskite).

2.9 Experimental section

Sample preparation

Polycrystalline samples of *t*-ZrOS were synthesized by solid-state reactions using starting materials ZrO_2, ZrS_2, ZrS_3, Y-substituted ZrO_2, and ZrF_4 under 5 GPa at 1200 °C for 1 hour. The ZrO_2 was prepared by heating a Zr foil (99.98%) at 1000 °C in air for 2 days, while the ZrS_2 and ZrS_3 were synthesized by heating the stoichiometric mixture of Zr foil and S grains (99.9999%) at 450 °C for 1 day and 1000 °C for 2 days in an evacuated silica glass tube. For the Y-substituted ZrO_2, we mixed the $ZrCl_2O{\cdot}8H_2O$ and $Y(NO_3)_3{\cdot}6H_2O$ in water with a magnetic stirrer for 20 minutes and neutralized it with ammonia, then, the resultant salt was filtered by pure water. Finally, the final product was obtained by annealing the salt at 600 °C for 10 hours. A polycrystalline sample of *c*-ZrOS was synthesized by heating the stoichiometric mixture of ZrO_2 and ZrS_2 at 1000 °C for 5 days in a silica glass tube filled argon.

Structural and chemical analyses

The crystal structure of the samples was analyzed by powder X-ray diffraction (D8ADVANCE-TXS Bruker AXS) using Cu *Kα* radiation (power: 45 kV × 360 mA) and equipped with a position sensitive detector. The amount of Y in the *t*-ZrOS:Y was measured by an electron probe micro analyzer (EPMA), while the nominal composition was adopted for the F content in *t*-ZrOS:F because of the difficulty to measure a reliable F content by the EPMA.

Transport measurements

The electrical conductivity was measured by the van der Pauw method with a sputtered Pt electrode (for *p*-type and un-doped *t*-ZrOS) or a Ag electrode paste (for *n*-type) using a physical property measurement system (PPMS Quantum Design). The Seebeck

coefficient was obtained from the gradient of the slope for the thermovoltage versus temperature relationship at room temperature.

Ultraviolet photoemission spectroscopy (UPS)

The energy levels of the CBM and the VBM from the $E_{vac.}$, which correspond to the electron affinity, χ, and ionization potential, I_p, respectively, were measured by UPS (excited by He I and II light sources). To prepare chemically pure surfaces, the dense *t*-ZrOS:F pellet was cleaved in a globe box that was directly connected to the UPS chamber. The χ was calculated using the measured optical bandgap by $\chi = I_p - E_g$. The UPS measurement was performed at ~2×10^8 Pa.

Hard X-ray photoemission spectroscopy

Hard X-ray photoemission measurements at room temperature were performed at the BL15XU undulator beamline (the excitation X-ray energy: $h\nu$ = 5950.05 eV) of SPring-8.[5] The binding energy was calibrated with the Fermi level of an evaporated Au thin film, and the total energy resolution was set to 240 meV, which was confirmed by the Fermi cut-off of the Au film. To obtain a clean sample surface, samples were cleaved in a preparation chamber.

Diffuse reflection measurement

Diffuse reflectance spectra R_{obs} were measured with powder samples, and calibrated by measuring a reference material (MgO powder) at the same time. The absorption coefficient α was obtained by using the Kubelka–Munk theory $(1-R_{obs})^2/(2R_{obs}) = \alpha/s$ (s is the scattering coefficient).[6] The direct allowed, indirect, and direct forbidden bandgaps

were estimated by $(h\nu\alpha/s)^2$, $(h\nu\alpha/s)^{1/2}$, and $(h\nu\alpha/s)^{2/3}$ versus $h\nu$, respectively.

Theoretical calculations

The electronic structures of *t*-ZrOS and *c*-ZrOS were derived by using the generalized gradient approximation Perdew–Burke–Ernzerhof (GGA-PBEsol) functional[7] and the full-potential linearized augmented plane wave with WIEN2k code.[8] The mesh samplings in the Brillouin zone (BZ) were 5 × 5 × 5 for the *t*-ZrOS and *c*-ZrOS. To correct the error of the bandgap derived from the GGA-PBEsol method, the bandgap of *t*-ZrOS was calculated by HSE06[9] with the VASP code and the bandgap of *c*-ZrOS was taken from Ref. [10] where the bandgap was calculated by GW method. The energy of the conduction band was shifted to match the correlated bandgap value. The absorption coefficient and the transition probability were calculated with WIEN2k code.[11] The edge of the absorption spectrum was shifted by the scissors operator to fit the bandgap estimated by the diffuse reflectance. The broadening parameter Γ was set zero in every absorption spectra. Maximally localized Wannier functions as projected functions were constructed from Zr 4*d*, S 3*p*, S 3*s*, and O 2*p* states within an energy window from −15 eV to approximately 7.5 eV.[12]

References

(1) Mizoguchi, H.; Kamiya, T.; Matsuishi, S.; Hosono, H. *Nat. Commun.* **2011**, *2*, 470.

(2) Kutzelnigg, W. *Angew. Chem. Int. Ed. Engl.* **1984**, *23* (4), 272.

(3) Hosono, H. *Jpn. J. Appl. Phys.* **2013**, *52* (9R), 090001.

(4) Dresselhaus, M. S.; Dresselhaus, G.; Jorio, A. *Group Theory: Application to the Physics of Condensed Matter*; Springer Science & Business Media, 2007.

(5) Ueda, S.; Katsuya, Y.; Tanaka, M.; Yoshikawa, H.; Yamashita, Y.; Ishimaru, S.; Matsushita, Y.; Kobayashi, K. *AIP Conf. Proc.* **2010**, *1234* (1), 403.

(6) Paul Kubelka; Franz Munk. *Z Tech Phys* **1931**, *12*, 593.

(7) Perdew, J. P.; Ruzsinszky, A.; Csonka, G. I.; Vydrov, O. A.; Scuseria, G. E.; Constantin, L. A.; Zhou, X.; Burke, K. *Phys. Rev. Lett.* **2008**, *100* (13), 136406.
(8) Blaha, P.; Schwarz, K.; Madsen, G.; Kvasnicka, D.; Luitz, J. **2001**.
(9) Heyd, J.; Scuseria, G. E.; Ernzerhof, M. *J. Chem. Phys.* **2003**, *118* (18), 8207.
(10) Hautier, G.; Miglio, A.; Ceder, G.; Rignanese, G.-M.; Gonze, X. *Nat. Commun.* **2013**, *4*, 2292.
(11) Ambrosch-Draxl, C.; Sofo, J. O. *Comput. Phys. Commun.* **2006**, *175* (1), 1.
(12) Mostofi, A. A.; Yates, J. R.; Lee, Y.-S.; Souza, I.; Vanderbilt, D.; Marzari, N. *Comput. Phys. Commun.* **2008**, *178* (9), 685.
(13) Persson, C.; Platzer-Björkman, C.; Malmström, J.; Törndahl, T.; Edoff, M. *Phys. Rev. Lett.* **2006**, *97* (14), 146403.

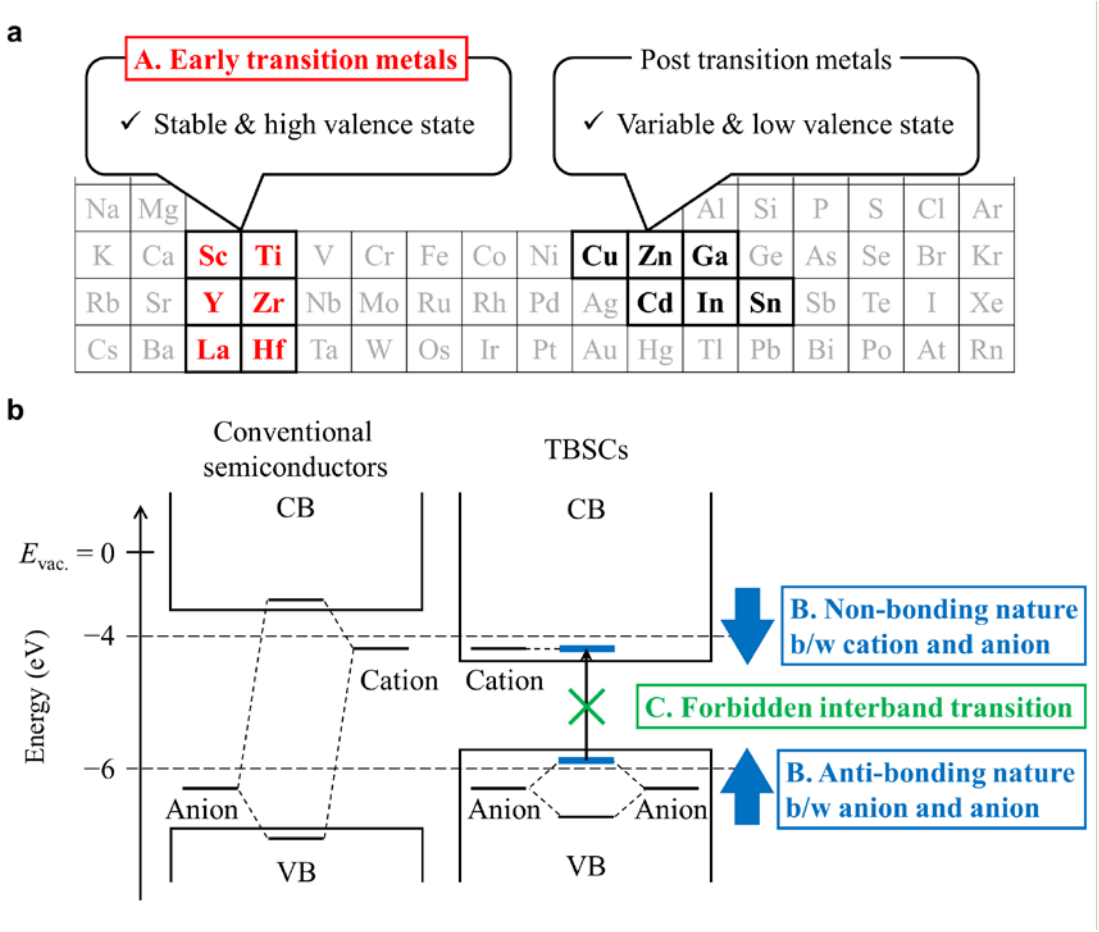

Figure 1. Material design concept for bipolar ionic semiconductor with optical transparency. **a.** Comparative atomic features of early and post transition metal (*eTM* and *pTM*). The valence state of *eTM* cations is stable and high relative to that of *pTM* cations, stabilizing a single phase and inducing a high coordination number (CN). These chemical and structural properties are expected to encourage an efficient carrier doping into *eTM* based compounds. **b.** The schematic chemical bonding diagrams of conventional ionic semiconductor and TBSCs. The CBM level below ~−4 eV and VBM level above ~−6 eV, relative to the vacuum level, are empirical requirements for *n*-type and *p*-type doping, respectively, in the ionic semiconductors.[3] The material design concept consists of three

requirements; [A] use of the *eTM* to improve the carrier doping efficiency, [B] non-bonding between a cation and an anion for *n*-type doping and anti-bonding between anions for *p*-type doping, [C] the forbidden band-edge transition to attain a low absorption coefficient in the energy range of visible light.

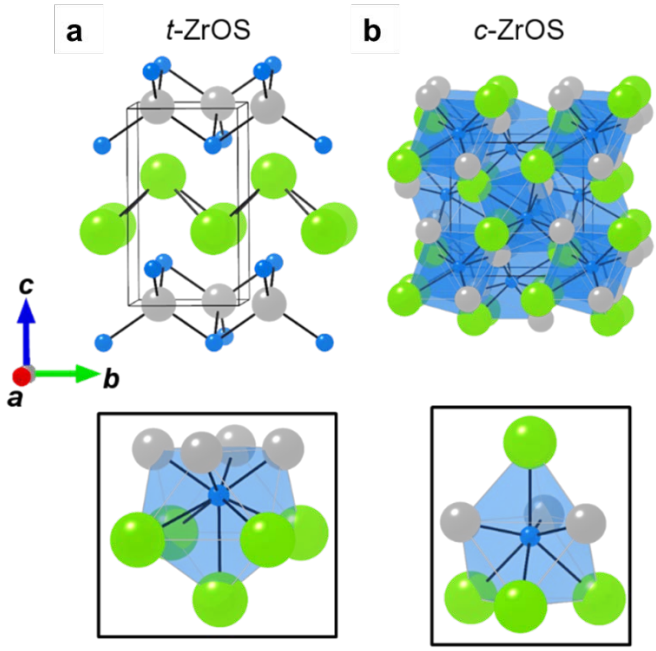

Figure 2. Crystal structures of *t*-ZrOS (**a**) and *c*-ZrOS (**b**). Blue, green, and grey spheres represent Zr, S, and O, respectively. Each local structure around Zr is shown below the crystal structure.

Table 1. Distances (Å) between nearest atoms for ZrOS. “Ionic” represents the distance estimated from summation of ionic radii.

	Zr-Zr	O-O	S-S	Zr-O	Zr-S	O-S
t-ZrOS	3.52	2.51	3.02	2.16	2.74	2.92
c-ZrOS	3.58	3.52	3.54	2.08	2.56	2.96
“Ionic”	1.78	2.76	3.68	2.27	2.73	3.22

Table 2. Irreducible representations (Irrep) of the in-phase and out-of-phase orbital configurations at the Γ point.

Atom	Site (Site symmetry)	Orbital	Irrep	
			In-phase	Out-of-phase
Zr	2*c* (4*mm*)	d_{x2-y2}	Γ_{3+}	Γ_{4-}
		d_{z2}	Γ_{1+}	Γ_{2-}
		d_{xy}	Γ_{4+}	Γ_{3-}
		d_{yz}/d_{zx}	Γ_{5+}	Γ_{5-}
S	2*c* (4*mm*)	p_x/p_y	Γ_{5-}	Γ_{5+}
		p_z	Γ_{2-}	Γ_{1+}
O	2*a* (-4*m*2)	p_x/p_y	Γ_{5-}	Γ_{5+}
		p_z	Γ_{2-}	Γ_{3+}

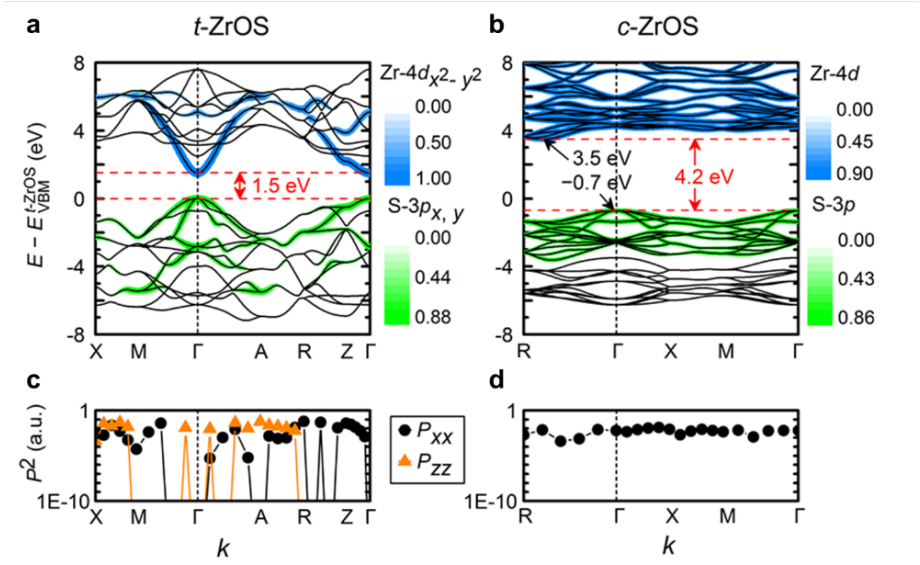

Figure 3. Calculated electronic structures of *t*-ZrOS and *c*-ZrOS. **a, b.** The band structures of *t*-ZrOS (**a**) and *c*-ZrOS (**b**). The vertical axes are aligned respective to the energy level of S-3*s* as shown in **Figure 4**. Blue and green in (**a**) denote the contributions from Zr-4d_{x2-y2} and S-3$p_{x, y}$, respectively, while those in **Figure 3b** from Zr-4*d* and S-3*p*, respectively. Here, the *x* and *y* axes are chosen along *a* and *b* crystallographic axes of the tetragonal unit cell. **c, d.** The *k*-dependences of transition matrix elements P^2 between the band edge states of *t*-ZrOS (**c**) and *c*-ZrOS (**d**). For the *t*-ZrOS, the P^2 are anisotropic because of the tetragonal symmetry.

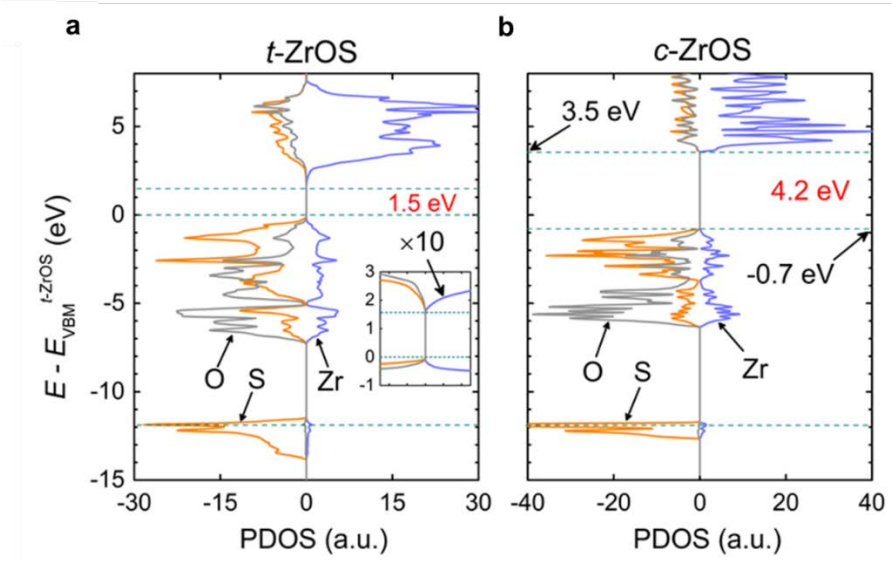

Figure 4. Atom-projected density of state (PDOS) for tetragonal (**a**) and cubic (**b**) phase of ZrOS (*t*-ZrOS and *c*-ZrOS, respectively). Blue, orange, and grey lines represent Zr, S, and O, respectively. The energy of DOS is aligned respective to the energy level of S-3*s* (~−12 eV) and the PDOS of *c*-ZrOS is shifted.

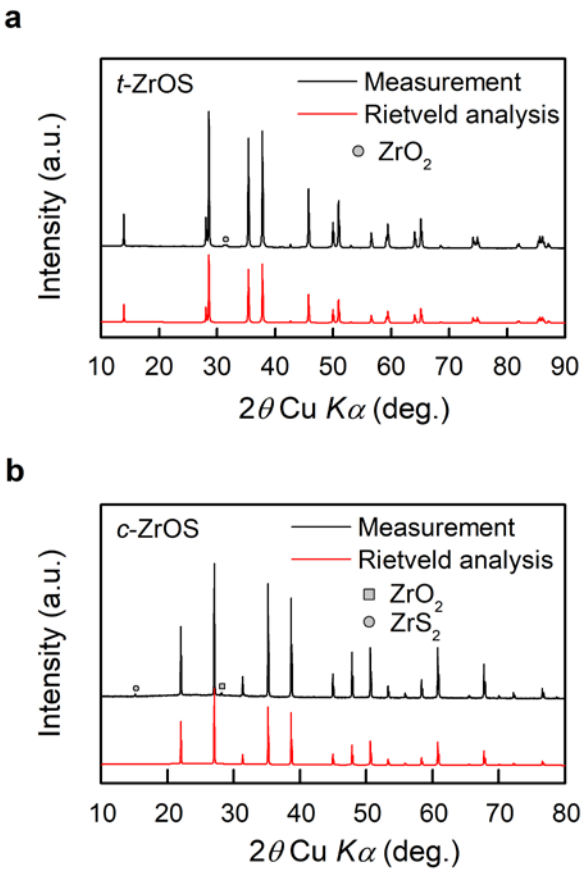

Figure 5. a, b. Powder X-ray diffractions (XRD) and result of Rietveld analysis for *t*-ZrOS (**a**) and *c*-ZrOS (**b**). The black and red line show the measured XRD pattern and the simulated XRD pattern, respectively. A little bit ZrO_2 and ZrS_2 were observed in both of phases, but these insulating impurity phases don't contribute the electrical conductivity of samples.

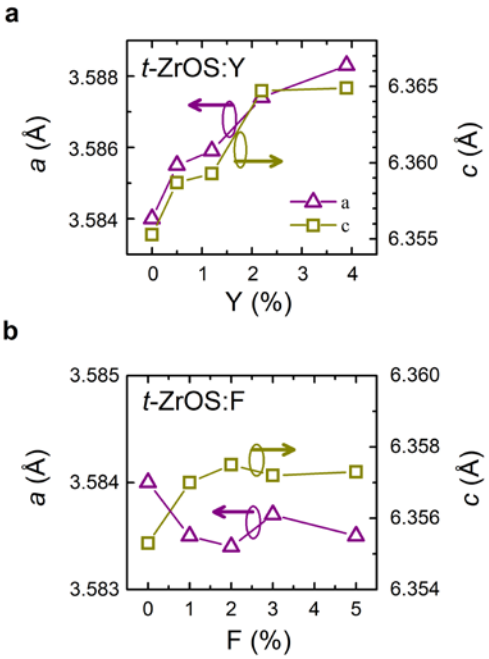

Figure 6. The chemical doping dependences of the lattice constant *a* and *c* for *t*-ZrOS. **a, b.** The lattice constant of Y (**a**) and F (**b**) doped *t*-ZrOS (*t*-ZrOS:Y and *t*-ZrOS:F, respectively). The monotonous increase of its lattice constant was clearly observed in *t*-ZrOS:Y, demonstrating the succession of yttrium substitution.

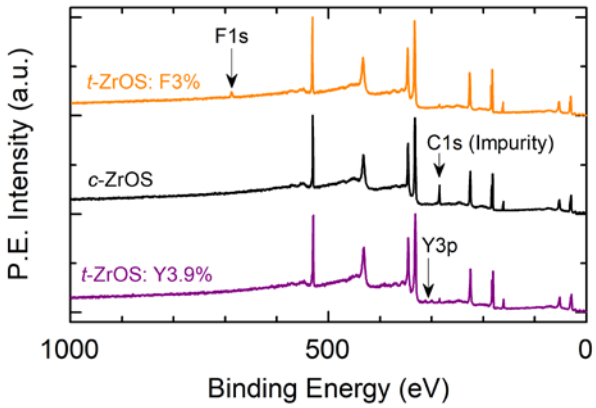

Figure 7. Atomic core levels measured with Hard X-ray Photoemission Spectroscopy (HAXPES) for *t*-ZrOS:F, *c*-ZrOS, and *t*-ZrOS:Y. The spectrum of F 1*s* and Y 3*p* levels were observed in *t*-ZrOS:F and Y, respectively, directly demonstrating the succession of chemical doping.

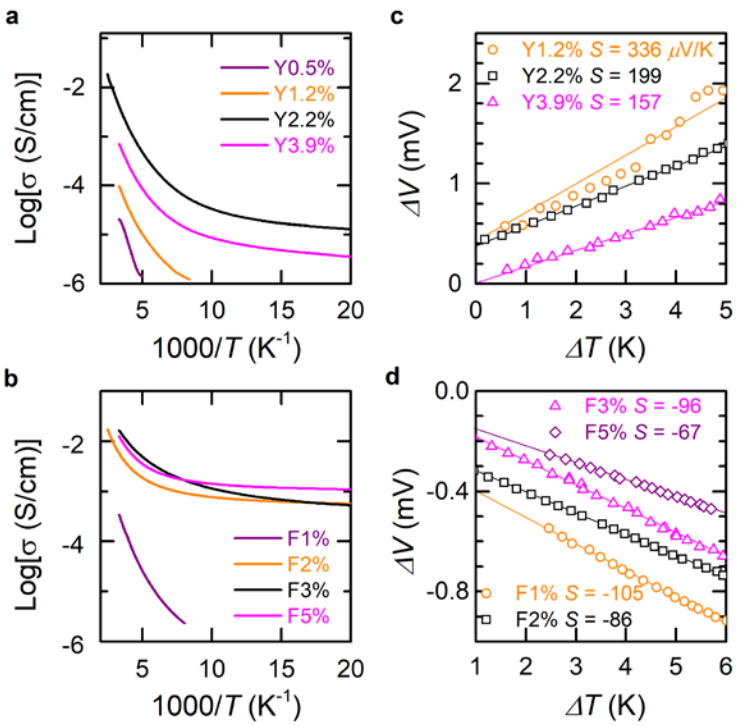

Figure 8. The results of transport measurement for *t*-ZrOS. **a, b.** The temperature dependence of the electrical conductivities for *t*-ZrOS:Y (**a**) and F (**b**). **c, d.** The thermopower measurements at room temperature for *t*-ZrOS:Y (**c**) and F (**d**). These voltage difference ΔV are arbitrarily shifted (here, no importance of absolute values). The Seebeck coefficients are derived from the slope of the thermopower measurements.

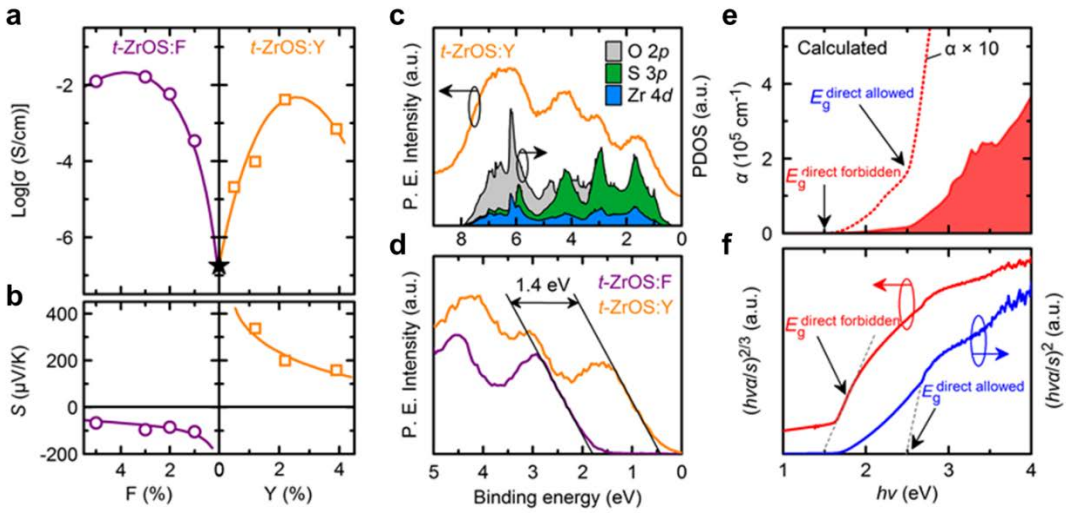

Figure 9. Electrical transport properties, hard X-ray photoemission spectra, and absorption coefficient of *t*-ZrOS. **a.** Doping dependence of conductivity of *t*-ZrOS:F and *t*-ZrOS:Y. Black filled star, open purple circle, and orange square represent the conductivity of non-doped *t*-ZrOS, *t*-ZrOS:F, and *t*-ZrOS:Y, respectively. The solid lines are guides for the eye. **b.** Doping dependence of Seebeck coefficient, *S*, of *t*-ZrOS:F and *t*-ZrOS:Y. **c.** Observed hard X-ray photoemission spectrum for *t*-ZrOS:Y and calculated atom-projected density of states (PDOS). **d.** Comparison of the spectra of *t*-ZrOS:F and *t*-ZrOS:Y. **e.** Calculated absorption coefficient, α, of *t*-ZrOS. Red dashed line is the α multiplied by 10 for clarity. **f.** Absorption spectra of *t*-ZrOS derived from diffuse reflectance spectra at 300 K and the Kubelka–Munk relation, where α, *s*, and *hν* are the absorption coefficient, scattering factor, and photon energy, respectively.[6] The vertical axis for direct allowed transition and direct forbidden transition are $(h\nu\alpha/s)^{2/3}$ and $(h\nu\alpha/s)^2$, respectively.

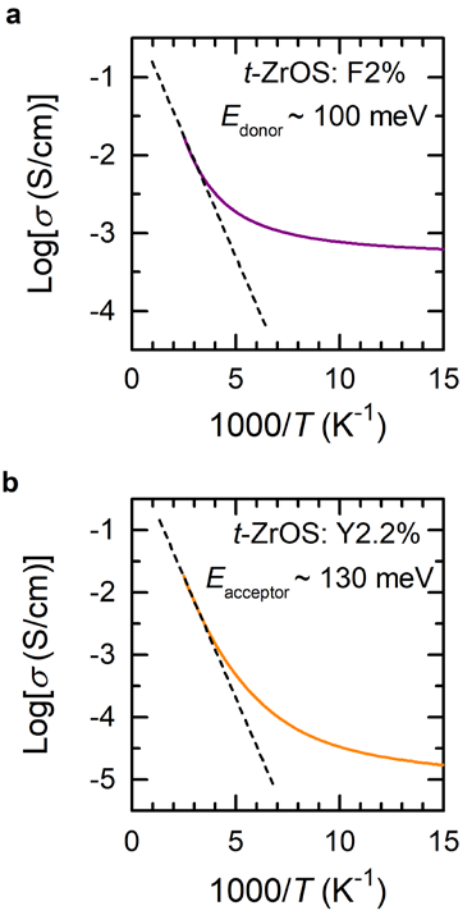

Figure 10. a, b. Arrhenius plots of the electrical conductivity for the F 2 mol% (**a**) and the Y 2.2 mol% (**b**) doped *t*-ZrOS. Fitting temperature range of both plots is from 2.5 (400 K) to 3.3 (~ 300 K). The activation energies were estimated as ~100 meV and ~130 meV in the F 2 mol% and Y 2.2 mol% doped *t*-ZrOS, respectively.

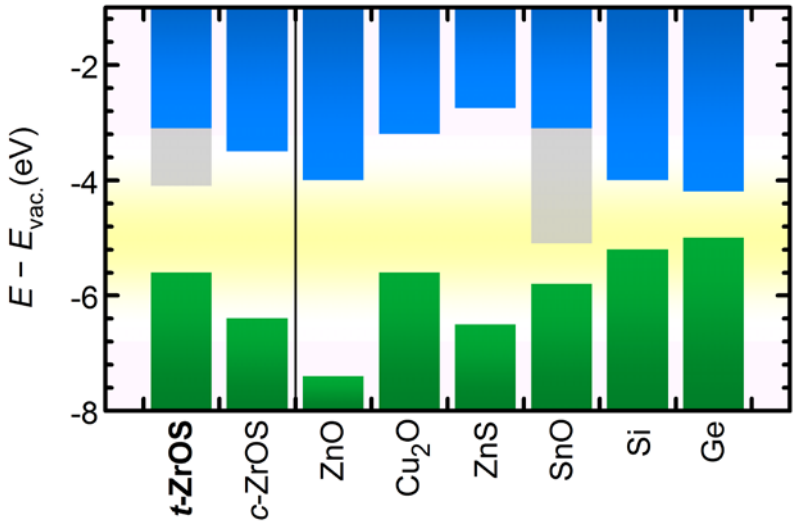

Figure 11. Band alignment of *t*-ZrOS, *c*-ZrOS, and related semiconductors. The ionization potentials and electron affinity for *t*-ZrOS and *c*-ZrOS are determined by combining ultraviolet photoemission spectroscopy, hard X-ray photoemission spectroscopy and diffuse reflection measurement (see **Figures 12 and 13**), while the data of other semiconductors except for ZnS were taken from Ref. 3 and the CBM and VBM level of ZnS were determined relative to those of ZnO, which is attained from Ref. 13. The gray region in *t*-ZrOS and SnO expresses the energy difference of their fundamental bandgap and the direct allowed bandgap. The energy window for bipolar doping is denoted as the yellow color area between ~－4 eV and ~－6 eV.

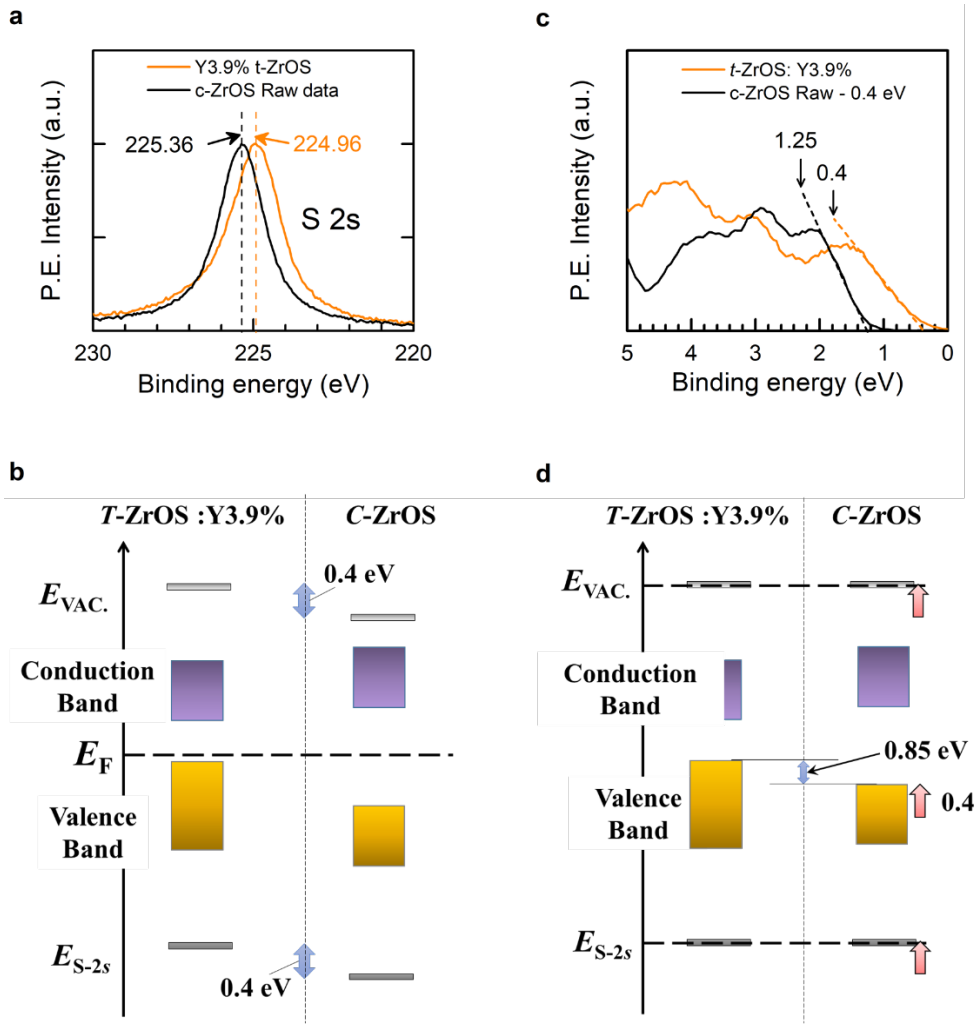

Figure 12. Spectrum of S 2*s* and valence band for *t*-ZrOS:Y and *c*-ZrOS measured with HAXPES and schematic picture to compare the energy levels of VBM from the vacuum level between *t*-ZrOS:Y and *c*-ZrOS. **a, b.** The comparison of the raw spectrum of S 2*s* level (**a**) and schematic energy level diagram (**b**) between *t*-ZrOS:Y and *c*-ZrOS. The difference of the both peaks was 0.4 eV. As illustrated in (**b**), assuming the consistency of the energy between the S 2*s* level and the vacuum level, the VBM levels of *t*-ZrOS:Y and *c*-ZrOS can be directly compared from the vacuum level when the spectra of *c*-ZrOS is shifted to shallower level (-0.4 eV). **c, d.** The comparison of spectrum of the valence band (**c**) and schematic energy band diagram (**d**) between the raw spectra

of *t*-ZrOS:Y and the 0.4 eV up-shifted spectra of *c*-ZrOS. **Figure 12c** shows that the difference of the valence band edge is 0.85 eV, denoting that the VBM of *c*-ZrOS is deeper by 0.85 eV than that of *t*-ZrOS as illustrated in (**d**).

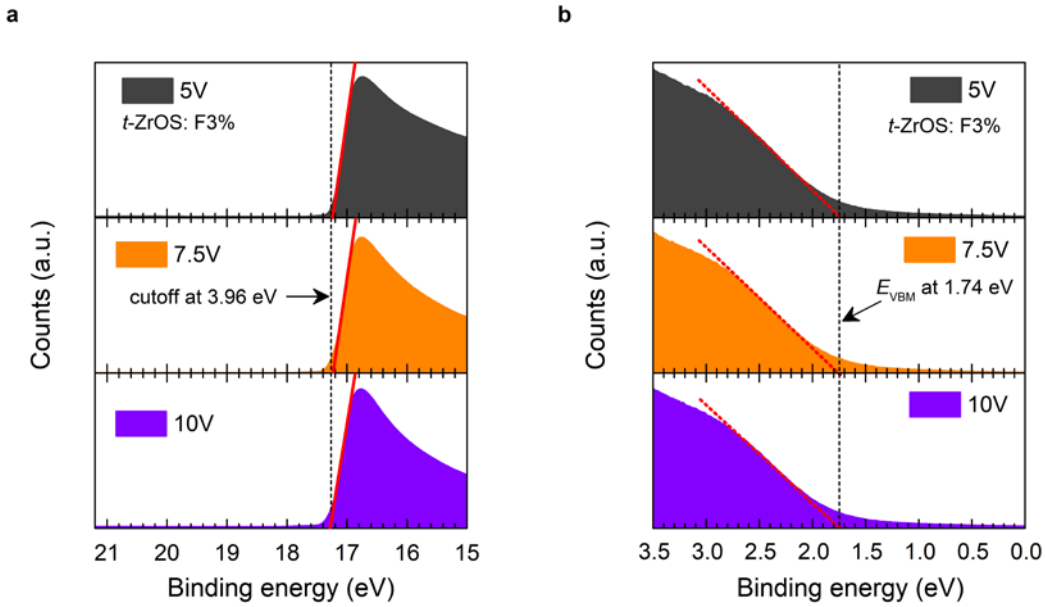

Figure 13. The results of ultraviolet photoelectron spectroscopy (UPS) measurements for *t*-ZrOS:F. The He I (21.22 eV) UPS spectrum are obtained with the various bias (5V, 7.5V, 10 V) applied to the sample. **a.** The spectrum in the cutoff region. Its estimated cutoff energy is 3.96 eV (= 21.22eV – 17.26 eV). **b.** The spectrum near the Fermi energy. The energy of VBM is 1.74 eV, and the ionization energy of *t*-ZrOS is thus 5.7 eV (= 3.96 eV + 1.74 eV).

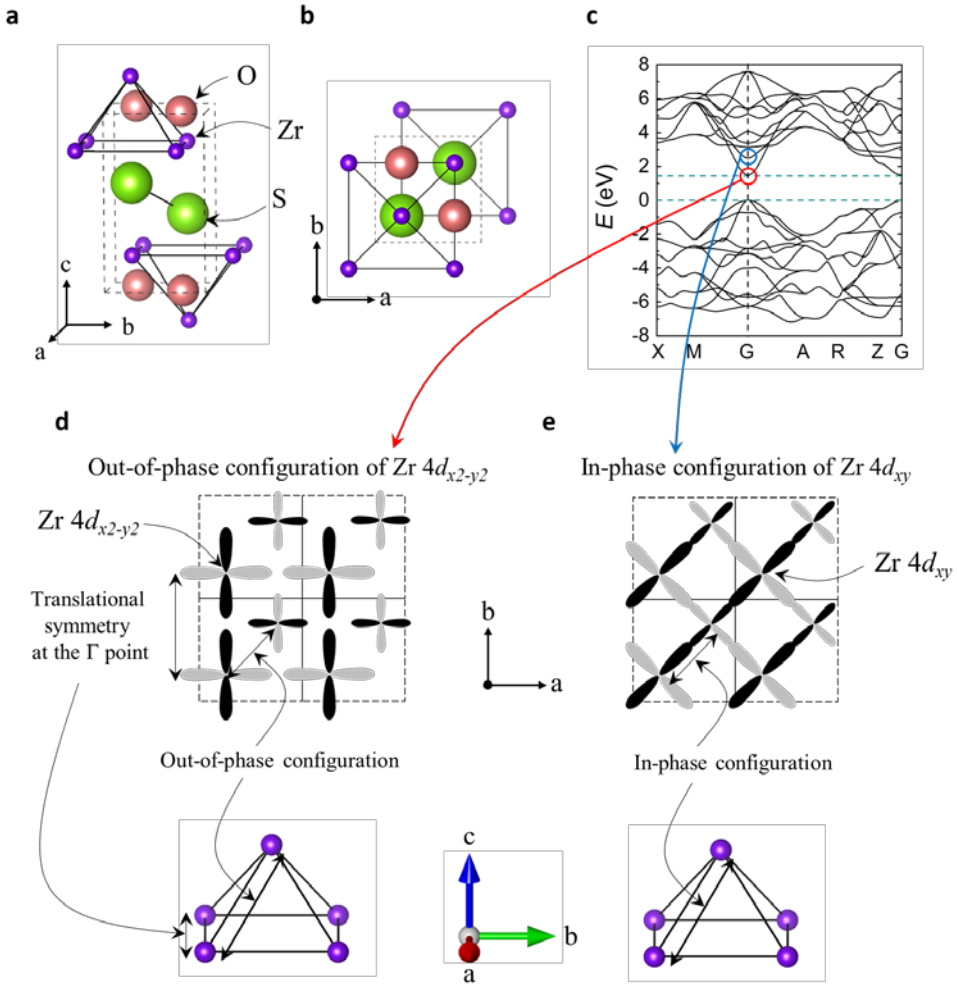

Figure 14. Crystal structure, band structure, and chemical bonding picture of *t*-ZrOS; **a, b.** The crystal structure of *t*-ZrOS. Blue, green, and grew spheres represent Zr, S, and O, respectively and dashed line represents unit cell in which there are each two atoms of Zr, S, and O. **c.** The band structure of *t*-ZrOS. **d, e.** The chemical bonding pictures of the CBM state (**d**) and the second lowest conduction band state (**e**) at the Γ point. Their schematically same size denotes that its electron orbitals are located with parallel on the same *ab* plain.

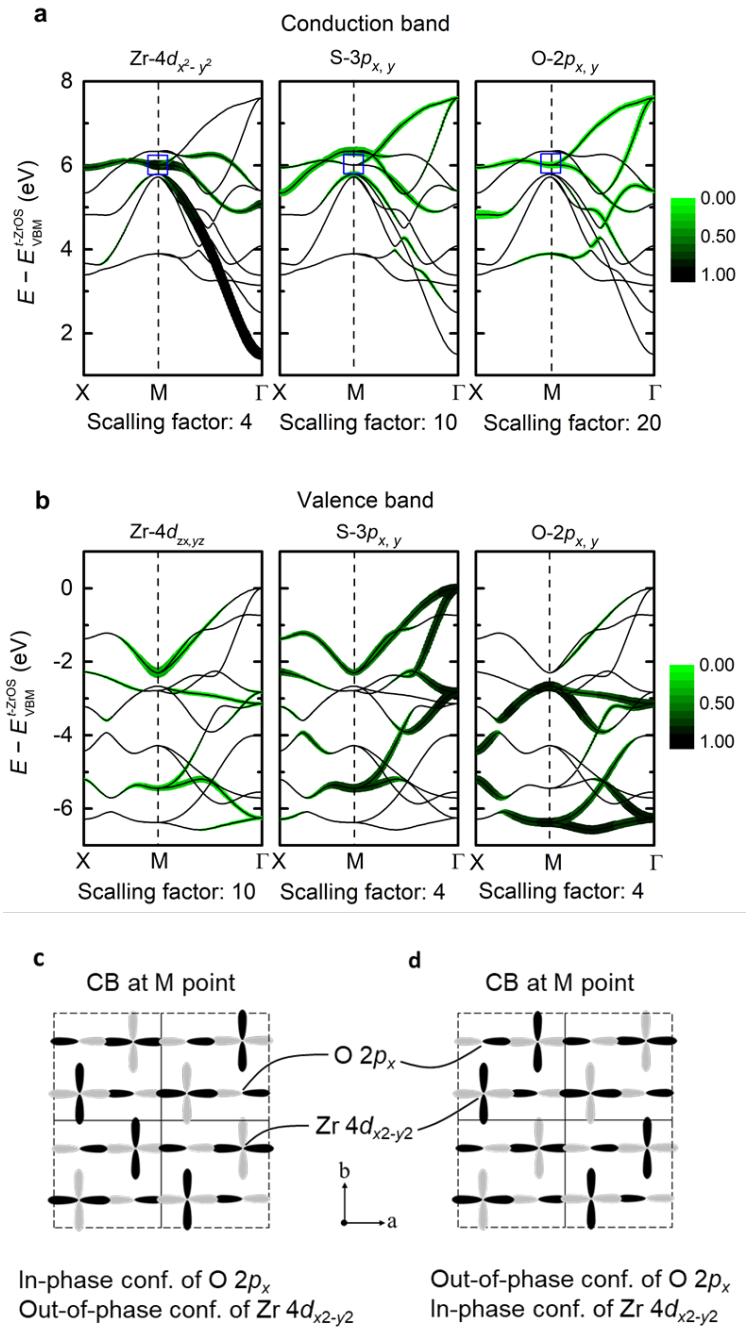

Figure 15. Band structures with the contribution of various orbitals for CB (**a**) and VB (**b**) and (**c, d**) chemical bonding pictures of CB at the M point (state corresponding to blue square in (**a**)). **a, b.** Gradual color from yellow to black represents the change from low to high value in contribution.

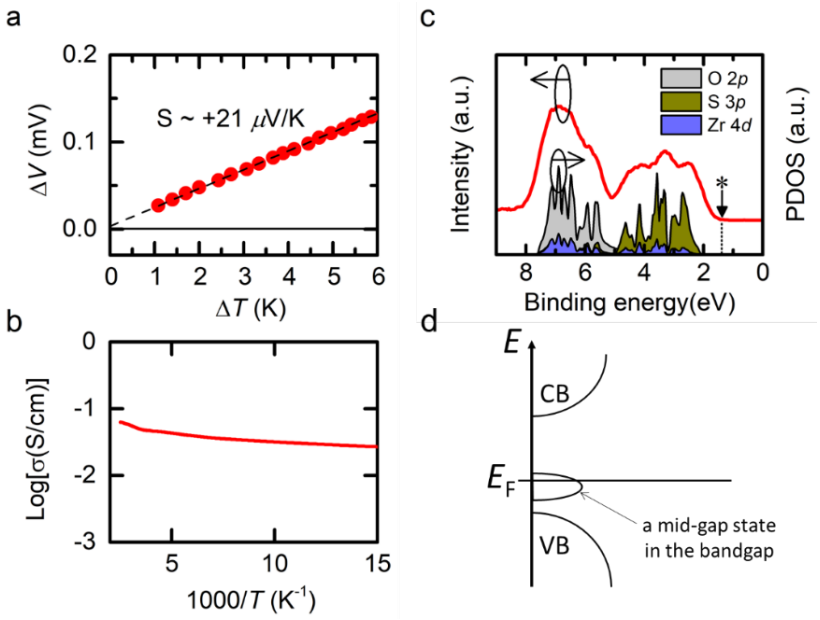

Figure 16. Experimental data and schematic of electronic state for undoped *c*-ZrOS. These data were obtained from the same sample. **a.** The thermopower measurement at room temperature. **b.** The temperature dependence of the electrical resistivity. **c.** Observed hard X-ray photoemission spectrum and calculated atom-projected density of state (PDOS). The observed spectra for the VB agrees well with the calculated electronic structure of *c*-ZrOS. The Fermi energy is located at approximately 1.5 eV above the valence band maximum (indicated by asterisk). **d.** Schematic of electronic state expected from the experimental data.

Table 3. Irreducible representations (Irrep) of each constitute of hexagonal LaSeF at the Γ point: its space and point groups are $P6_3/mmc$ and D_{6h}, respectively. The irrep of CBM and VBM are G_{1+} (La d_{z2}) and G_{2-} (Se p_z), respectively. The CBM is composed of only Zr d_{z2} orbital and the VBM is composed of Se p_z and F p_z orbital. Both states are non-bonded state between anion and cation.

Atom	Site (site symmetry)	Orbital	Irrep	
			In-phase	Out-of-phase
La	2*c* (-6m2)	d_{x2-y2}/d_{xy}	G_{6+}	G_{5-}
		d_{z2}	**G_{1+}**	G_{4-}
		d_{yz}/d_{zx}	G_{5+}	G_{6-}
Se	2*a* (-3*m*.)	p_x/p_y	G_{5-}	G_{6-}
		p_z	**G_{2-}**	G_{4-}
F	2*d* (-6*m*2)	p_x/p_y	G_{5-}	G_{6+}
		p_z	G_{2-}	G_{3+}

Table 4. Irrep of each constitute of hexagonal ZrS_2 at the Γ point: its space and point groups are *P*-3*m*1 and D_{3d}, respectively. The irrep of VBM is G_{2-} (S p_z), which denotes the non-bonding state with Zr *d* orbitals. The CBM is not at the Γ point due to indirect bandgap.

Atom	Site (site symmetry)	Orbital	Irrep	
			In-phase	Out-of-phase
Zr	1*a* (-3*m*)	d_{x2-y2}/d_{xy}	G_{1+}	
		d_{z2}	G_{3+}	
		d_{yz}/d_{zx}	G_{3+}	
S	2*d* (3*m*)	p_x/p_y	G_{3-}	G_{3+}
		p_z	**G_{2-}**	G_{1+}

Table 5. Irrep of each constitute of orthogonal ZrNI at the Γ point: its space and point groups are *Pmmn* and D_{2h}, respectively. The irrep of the CBM and the VBM are G_{2+} (Zr d_{xy}) and G_{3-} (N and I p_x), respectively. The CBM is composed of only Zr d_{xy} orbital, which denotes no contribution of anion *p* orbitals.

Atom	Site (site symmetry)	Orbital	Irrep	
			In-phase	Out-of-phase
Zr	2*b* (*mm*2)	d_{x2-y2}/d_{z2}	G_{1+}	G_{2-}
		d_{xy}	**G_{2+}**	G_{1-}
		d_{yz}	G_{3+}	G_{4-}
		d_{zx}	G_{4+}	G_{3-}
N and I	2*a* (*mm*2)	p_x	**G_{3-}**	G_{4+}
		p_y	G_{4-}	G_{3+}
		p_z	G_{2-}	G_{1+}

Table 6. Irrep of each constitute of tetragonal Ba_2ZrS_4 at the Γ point: its space and point groups are *I*4/*mmn* and D_{4h}, respectively. The irrep of the CBM is G_{4+} (Zr d_{xy}), which denotes the non-bonding state with S *p* orbitals. The VBM is not at the Γ point due to indirect bandgap.

Atom	Site (site symmetry)	Orbital	Irrep	
			In-phase	Out-of-phase
Zr	2*a* (4/*mmm*)	d_{x2-y2}	G_{2+}	
		d_{z2}	G_{1+}	
		d_{xy}	**G_{4+}**	
		d_{yz}/d_{zx}	G_{5+}	
Ba and S	4*e* (4*mm*)	*s*	G_{1+}	G_{3-}
		p_x/p_y	G_{5-}	G_{5+}
		p_z	G_{3-}	G_{1+}
S	4*c* (*mmm*)	p_x/p_y	G_{5-}	
		p_z	G_{3-}	G_{4-}

Chapter 3. Inversion of carrier polarity with polymorph change in LaSeF

3.1 Introduction

Carrier doping and control of carrier polarity are key technical issues in the creation of novel semiconductors. Wide bandgap semiconductors are in demand for applications in power electronics and optoelectronics[1,2,3,4]. However, control of carrier polarity, which is required for the realization of bipolar semiconductors, is a major challenge for wide gap semiconductors.

Tetragonal phase of ZrOS gives important insights to next material design.

(1) Early transition metal plays a key role to improve carrier dopability.

(2) Non-bonding state between cation and anion is useful to reduce the effective mass.

Considering the above insights, hexagonal phase of LaSeF (*h*-LaSeF) is a candidate for a wide-gap bipolar semiconductor. The *h*-LaSeF possesses the unique band edge states composed of non-bonding state between cation and anion. These states decrease the effective mass of electron and hole. Additionally, fluorine, which is highest electronegativity element, widens bandgap because of high Madelung potential. Therefore, combined with *e*TM effect, *h*-LaSeF is expected to become the wide-gap bipolar semiconductor. This design is summarized in **Figure 1**.

However, a polymorphic change from hexagonal to tetragonal phases is observed, accompanying a major carrier switch induced by doping of LaSeF. The *h*-LaSeF exhibits *p*-type conduction when Ca is doped into La sites. Cl doping into Se sites stabilizes the tetragonal phase (*t*-LaSeF) and *n*-type conduction is realized. This experimental fact is consistent with the small difference in total energies between both structures. Furthermore,

the calculation reveals that orbital symmetry is a key factor for controlling the band edge levels in different polymorphs.

LaSeF realizes inversion of carrier polarity with keeping wide-gap nature. This is a rare case of a change in polymorph and carrier polarity induced by impurity doping. By also considering the case of ZrOS, it is concluded that polymorph in *e*TM based compositions largely changes electronic structures based on its orbital symmetry. These findings will provide new insights into the design of wide-gap semiconductors.

3.2 Results

Crystal structures and irreducible representations

Figures 2a and 2b show the crystal structures of hexagonal and tetragonal LaSeF, whose structure types are ZrBeSi (*P*63/*mmc*) and PbClF (*P*4/*nmm*), respectively. In both structures, the coordination number around La^{3+} is 9. In the hexagonal phase, the honeycomb $[LaF]^{2+}$ layer is separated by the larger Se^{2-} anions. In the tetragonal phase, a PbO-type $[LaF]^{2+}$ layer is sandwiched by the Se^{2-}. Lattice constants are shown in **Figures 3** and **4**. Most of them are consistent with the sum of the ionic radii, which indicates that they are ionic compounds. **Tables 1** and **2** shows irreducible representations (Irrep) at Γ point for *h*-LaSeF and *t*-LaSeF, respectively. In **Table 1**, the Irrep of La 5d_{z2}, G_{1+}, doesn't match the Irrep of other atomic orbitals, resulting in the non-bonding state between cation (La) and anions (Se and F). Similarly, the out-of-phase configuration of Se p_z orbital forms the non-bonding with La 5*d* orbitals because of its unique Irrep, G_{2-}. On the other hand, in *t*-LaSeF (see **Table 2**), non-bonding state emerges only in *d* orbitals of La. The Irrep of *t*-LaSeF is consistent with that of *t*-ZrOS owing to the same structure type, PbClF.

Band structures

Figures 5a and **5b** show band structures of the *h*-LaSeF and *t*-LaSeF, respectively. The calculated band gaps of the *h*-LaSeF and *t*-LaSeF were notably different at 1.73 and 1.03 eV, respectively. Note that the calculated band gaps are likely to under estimate the experimental values because we used an LDA functional. The states of CBM and VBM for *h*-LaSeF are composed of non-bonding La $5d_{z2}$ and Se $4p_z$ orbitals, respectively. Both orbitals largely extend in the *z*-axis direction. These feature are found in the sharp dispersion of bands and small effective mass along Γ-A, as shown in **Figures 5a** and **Table 3.** As shown in **Table 3**, the hole effective mass for the *h*-LaSeF is ~0.24 m_0 along the Γ-A line and ~0.83 m_0 along Γ-K, while the electron effective mass is ~0.57 m_0 along the Γ-A line and ~0.71 m_0 along Γ-K. On the other hand, the band edges of *t*-LaSeF are constituted of La $5d_{x2-y2}$ and Se $4p_{x/y}$ orbitals as CBM and VBM, respectively. Therefore, large effective mass and flat bands appear along Γ-Z line as shown in **Figure 5b** and **Table 3**. As described in **Table 3**, the mass of holes in the tetra-phase is relatively heavy, at ~0.99 m_0 along the Γ-M and ~4.35 m_0 along Γ-Z. The electron effective mass is similar, ~0.45 m_0 along the Γ-M line and ~1.34 m_0 along Γ-Z line. Symmetry analysis[5] revealed the bang gap of the hexa-phase at the Γ point is a direct-allowed type (from Γ_{2-} to Γ_{1+}), while that of the tetra-phase is a forbidden-type (from Γ_{5-} to Γ_{4-}).

Sample characterization and optical property

Figures 6a and **6b** show the XRD pattern of non-doped sample and analyzed Ca-content by EPMA, respectively. The diffraction patterns of the un-doped and Ca-doped samples were indexed as a hexagonal lattice. As the nominal Ca content increased, the

analyzed Ca content in the LaSeF grains monotonically increased to ~2%, and then remained at a constant value above 2%. Similarly, the lattice constant, *c*, decreased as the Ca-content was increased to 2% (**Figure 6c**), indicating that the Ca solubility limit is located at approximately 2%. Hereafter, we use the nominal content for simplicity. The diffuse reflection spectra of the non-doped and 1%-Ca doped samples showed steep absorption jumps at 2.89 and 2.91 eV as seen in **Figure 6d**, respectively. This observation is consistent with the allowed transition nature of the *h*-LaSeF. Unlike the Ca-doped samples, 1%-Cl doping considerably changed the XRD pattern, as shown in **Figure 6e**, which is indexed as a tetragonal PbClF-type structure. The analyzed Cl content linearly increased with the nominal Cl content (**Figure 6f**), and the lattice constants decreased (**Figure 6g**). The decrease of lattice constant indicates substitution of Cl for Se sites, rather than F sites, because the ionic radius[6] of Cl (1.8Å) is larger than that of F (1.3) but smaller than that of Se (2.0). The absorption of the Cl-doped sample begins gently at a lower energy of $h\nu$ = 2.2 eV (**Figure 6h**), which is also consistent with the nature of the forbidden optical transition at the Γ point.

Transport properties

Figure 7a shows the results of typical thermopower measurements for the Ca-doped *h*-LaSeF and Cl-doped *t*-LaSeF. Thermopower is a reliable physical quantity for determining the carrier polarity, particularly for disordered materials, such as polycrystalline bulk and amorphous materials, though the Hall voltage gives the reverse sign in many cases[7]. It is evident that the sign of the Seebeck coefficient *S* at room temperature changes from positive in the Ca-doped *h*-LaSeF to negative in the Cl-doped *t*-LaSeF. **Figures 7b** and **7c** summarize the doping dependence of *S* and the electrical

conductivity σ at 300 K, respectively. The non-doped *h*-LaSeF exhibited high resistivity ~10^9 Ω cm. For the Ca-doped sample, the conductivity was enhanced to over 10^2 S cm^{-1} at a Ca content of 3%. The Cl-doped *t*-LaSeF showed a much higher conductivity than that of the Ca-doped *h*-LaSeF. **Figures 8a-8c** show the conductivity for Ca doped *h*-LaSeF as a function of temperature. Band transport occur when the electron is thermally excited to the CB from donor level or from the VB to acceptor level. As shown in **Figure 8a**, the acceptor level of Ca 3% doped *h*-LaSeF is approximately 23 meV, estimated from Arrhenius plot. However, as shown in **Figure 8b**, the electrical conductivity approaches a constant value as temperature decreases below 100K, which indicates the variable range hopping (VRH) conductivity at low temperature. The mechanism based on VRH brings the temperature dependence of $T^{-1/4}$ to the σ. As shown in **Figure 8c**, the conductivity of *h*-LaSeF is linear as a function of $T^{-1/4}$ in the region below 100K. On the other hand, Cl doped *t*-LaSeF indicates the band transport even at low temperature. **Figures 8d-8f** show the conductivity for Cl doped *t*-LaSeF as a function of temperature. The donor level of Cl 1% doped *t*-LaSeF is ~19 meV as indicated in **Figure 8d**. **Figure 8e** and **8f** show that the electrical conductivity strongly depends on $1/T$ even at low temperature. This result suggests that the band transport is realized even at low temperature. Finally, we compare the mobility of electrons and holes which are estimated from σ and *S*, where *S* corresponds to the carrier concentration. The *S* is ~+85 μV/K and ~-70 μV/K for Ca 3% doped *h*-LaSeF and Cl 3% doped *t*-LaSeF, respectively, indicating that their carrier concentration is similar value. Then, their σ also have similarity, ~0.035 S/cm for Ca 3% doped *h*-LaSeF and ~0.022 S/cm for Cl 3% doped *h*-LaSeF. Therefore, it is concluded that the mobilities of electrons and holes are roughly the same value.

3.3 Discussion

Polymorph for material design

Material design based on polymorphic control has attracted much attention in recent years[8,9]. However, polymorph of LaSeF is a rare case where structural change corresponds to its functionality. For example, the hole effective mass of *h*-LaSeF is smaller than that of *t*-LaSeF. Conversely, the electron effective mass of *t*-LaSeF is smaller than that of *h*-LaSeF. That is, the polymorphic change improves the transport properties in this system. Therefore, this study suggests the new design that semiconducting properties are improved through polymorphic change.

Orbital symmetry and band edge states

Here, we discuss the origin of alternation of electronic structures based on polymorphic change and reveal the relationship between chemical bonding state and the functionality. **Figure 9a** shows the density of states (DOS) of the *h*-LaSeF and *t*-LaSeF, where the energy is aligned at the La 5*s* levels located approximately 32−33 eV below their VBM. We found that the E_{CBM} of the *t*-LaSeF is deeper and that the VBM is shallower compared with those of *h*-LaSeF. The difference of the CBM between the two polymorphs is attributed to the chemical bonding states between the La 5*d* orbitals. The electron density distributions at the CBM of *h*-LaSeF and *t*-LaSeF are shown in **Figure 9b**. In the hexa-phase, a La $5d_{z2}$ orbital pointing along the *c* axis mainly contributes to the CBM state and the lobe is parallel to the neighboring $5d_{z2}$ orbital in the nearest unit cell, in a similar arrangement to a π-bonding interaction. In the *t*-LaSeF, the $5d_{x2-y2}$ orbitals point toward each other in a σ-bonding arrangement.

In **Figures 9c** and **9d**, the corresponding bonding and anti-bonding states are shown

for *h*-LaSeF and *t*-LaSeF respectively. Because the unit cell of LaSeF has two chemical formulae, there are two configurations of the La 5*d* orbital, *i.e.*, in-phase and out-of-phase configurations. The orbital configuration and corresponding band structure of La $5d_{z2}$ orbital are the same as the π and π^* bonding of C $2p_z$ in graphene[10,11]. The in-phase configuration of the La $5d_{z2}$ orbital at the Γ point forms a bonding state, which has its lowest energy in the La $5d_{z2}$ orbital-based bands. The out-of-phase configuration at the Γ point corresponds to the anti-bonding state, which has the highest energy because the phase of the La $5d_{z2}$ orbital is inverted with respect to both the nearest (4.22Å) and next nearest neighbor (4.76Å) La-sites. The CBM of the tetragonal phase is composed of out-of-phase La $5d_{x2-y2}$ orbitals, in which the nearest neighbor $5d_{x2-y2}$ orbitals (4.14Å) form σ-bonding interactions, while the next nearest neighbor $5d_{x2-y2}$ (4.28Å) takes a π-bonding configuration. The highest energy configuration of La-$5d_{x2-y2}$ appears at the M point, where both the in-phase and out-of-phase configurations form a σ-anti-bonding state (σ*) and those energy levels are degenerate. The corresponding eigenvalues, $E(k)$, of the bonding and anti-bonding states are indicated by open circles and squares, respectively, in **Figure 5a** for the hexagonal and **Figure 5b** for the tetragonal phase. Owing to the lower orbital overlap for the π-like configuration[12], the band width of the La $5d_{z2}$ orbitals in the hexa-phase is only ~2 eV, which is narrower than the σ band derived from the La $5d_{x2-y2}$ in the tetra-phase.

Finally, the concepts obtained from the present findings are summarized in **Figure 10**. The formation of bonding and antibonding states between cations and anions is responsible for the band gap in ionic semiconductors and insulators (**Figure 10a**)[13]. However, if hybridization of the relevant orbitals in cations and anions is forbidden by symmetry at a specific *k* point, the cation-cation bonding and anion-anion antibonding

states are the main contributor to E_{CBM} and E_{VBM}[14], respectively, as shown in **Figures 10b** and **10c**. According to the irreducible representation of La 5*d*, Se 4*p*, and F 2*p* at the Γ point **(**see **Table 1** and **2**), we found that the La 5d_{z2} and Se 4p_z orbitals in the *h*-LaSeF can interact only with themselves but cannot achieve bonding and anti-bonding states with other anion *p* and La 5*d* orbitals at the Γ point. Therefore, the bonding state between the La 5d_{z2} orbitals and the anti-bonding state between Se 4p_z orbitals constitute the CBM and the VBM, respectively. Thus, the energy levels simply depend on the orbital overlap between the La 5d_{z2} orbitals or Se 4p_z orbitals. Alternatively, the CBM in the tetra-phase is composed of La 5d_{x2-y2} and the VBM state is composed of the Se 4$p_{x/y}$ and La 5$d_{xz/yz}$ orbitals. Because the CBM of *eTM*-based semiconductors is composed of cation *d* orbitals, the crystal structure and orbital configuration have a more notable effect on the energy level of the CBM than those effects on *pTM* semiconductors, for which the CBM usually consists of spherical *s* orbitals of the metal[15]. This effect is clearly demonstrated by the shallower CBM formed from π-type La 5d_{z2} bonding in the *h*-LaSeF and the deeper CBM from the σ-type La 5d_{x2-y2} bonding in the *t*-LaSeF. Therefore, proper choice of parent materials is the key to achieving wide-gap bipolar conduction in *eTM*-based semiconductors.

AXY compounds

The AXY (A = rare earth, X = halogen, and Y = chalcogen) compounds are fascinating to form a high symmetry crystal structure. **Figure 11** shows the structure map of mixed anion AXY for two cases, where seven different structure types appear, *i.e.*, YOF, PbClF, FeOCl, SmSI, YSF, YSeF, and ZrBeSi-type. In these structure types, non-bonding between cation and anion appear in cation d_{x2-y2} in PbClF, cation d_{z2} and anion p_z in

ZrBeSi, and cation d_{xy} in FeOCl. This indicates that the electronic structure of AXY varies based on the orbital symmetry.

Additionally, as shown in **Figure 11a**, LaSeF is located at a boundary between ZrBeSi and PbClF-type structures. We calculated the internal energy difference between two structure types for compounds located at the boundary, and found a small energy difference in the case of LaSeF (PbClF *vs* ZrBeSi) and LaTeCl (PbClF *vs* $PbCl_2$), indicating that these crystal structures could easily transform into each other (See **Table 4**).

Origin of polymorphic change

Next we discuss the origin of the structural change from the *h*-LaSeF to *t*-LaSeF upon Cl-doping. Cl substitution into Se sites could have two possible effects on the electronic and crystal structures of the hexa-phase; chemical pressure derived from the difference of the ionic radius and electron doping into the conduction band. According to the structural map shown in **Figure 11**, a positive chemical pressure, such as that introduced by substitution of smaller Cl^- ions into larger Se^{2-} ion sites, would lead to a structural change of the tetragonal PbClF-type structure as illustrated in **Figure 12b**. Electron doping into the deeper CBM of the tetra-phase is energetically more favorable than into the shallower CBM of the hexa-phase. We examined substitution with 1% S^{2-}, which has almost the same size as Cl^-, into Se^{2-} sites of the hexa-phase and found a similar stabilization of the tetra-phase without electron-doping. This result clarified that the positive pressure effect was the main reason for the phase transition in the present case.

3.4 Conclusion

In conclusion, we examined structural and chemical bonding effects on the electronic structure, transport and optical properties of hexagonal and tetragonal LaSeF. We found that the Ca substitution for La sites of the hexagonal phase was effective for obtaining *p*-type conduction, and Cl 1% substitution at Se sites induced a structural change from the hexagonal to tetragonal phase. Inversion of carrier polarity from *p*-type in the Ca-doped hexagonal phase to *n*-type in the Cl-doped tetragonal phase was confirmed by Seebeck coefficient measurements, and the band gap of the hexagonal phase also changed considerably from 2.9 to 2.2 eV for the tetragonal phase. The conductivity changed from 10^{-9} S cm^{-1} for the non-doped hexa-phase to over 10^{-2} S cm^{-1} for both the Ca-d and Cl-doped samples. Band structure calculations revealed the tetragonal phase has a deeper CBM than that of the hexagonal phase, which is consistent with the experimental finding of *n*-type conduction in the tetragonal phase. From the chemical bonding analysis, we concluded that the change of the carrier polarity and reduction of the band gap can be attributed to differences in the orbital configuration at the CBM. Namely, the shallower CBM in the hexagonal phase is based on the π-type La $5d_{z2}$ bonding state with low orbital overlap and the deeper CBM is related to the σ-type La $5d_{x2-y2}$ bonding state in the tetragonal phase. These results demonstrated that the proper choice of chemical bonding at the band edge state is key to achieving wide-gap bipolar conduction in *eTM*-based semiconductors.

3.5 Experimental section

Synthesis and characterization

Non-doped samples were synthesized by solid-state reactions using La_2Se_3 and LaF_3.

The mixed starting material was sealed with a silica glass tube filled with Ar gas, and the tube was heated at 900°C for 18 h. Samples doped with Ca at La sites were prepared from La_2Se_3, LaF_3, CaSe, and Se by the same procedures. To compensate for the Se-deficiency, the resulting sample was placed in an evacuated silica tube with a small amount of Se, and subsequently the tube was heated at 400°C for 4 h. Cl-doped samples were prepared from La_2Se_3, LaF_3, $LaCl_3$, and LaH_2 by the same procedures. X-ray diffraction (XRD) of the samples was measured by D8ADVANCE-TXS (Bruker AXS) with CuKα radiation (power: 45 kV × 360 mA) equipped with a position sensitive detector. The structural parameters were refined using TOPAS code[16]. The amounts of Ca and Cl in LaSeF were determined by an electron probe micro analyzer (EPMA). The quantitative analyses with the EPMA were conducted with atomic number, absorption, and fluorescence correction against standard samples of LaAs for La, ZnSe for Se, BaF_2 for F, $CaSiO_3$ for Ca, and NaCl for Cl.

Transport measurement

The electrical conductivity was measured by the van der Pauw method, with a sputtered Pt electrode (for *p*-type materials and un-doped hexagonal LaSeF) or an Ag electrode paste (for *n*-type), with the use of a physical property measurement system (PPMS Quantum Design). The Seebeck coefficient was obtained from the gradient of the slope for the thermovoltage versus temperature relationship at room temperature.

Diffuse reflection measurement

Diffuse reflectance spectra R_{obs} were measured on powdered samples, and calibrated against a reference material (MgO powder). The absorption coefficient α was obtained by Kubelka–Munk theory $(1-R_{obs})^2/(2R_{obs}) = \alpha/s$ (where s is the scattering coefficient)[17]. The direct allowed and direct forbidden band gaps were estimated from plots of $(h\nu\alpha/s)^2$ and

$(h\nu\alpha/s)^{2/3}$ versus $h\nu$, respectively.

Theoretical calculation

The electronic structure calculations were performed using the projected augmented-wave method as implemented in the VASP code[18], and a local density approximation (LDA) + U[19] (where U = 13 eV for *f*-orbital of La to construct a Wannier orbital from the 5*d* orbital of La) was used. A 500-eV cutoff in the plane wave expansion ensured that the calculations converged to 10^{-6} eV. For total energy calculations, the lattice parameters and atomic positions were fully relaxed by a structural optimization procedure minimizing the total energy (< 10^{-6} eV) and force (< 10^{-5} eV/Å). We used an 8 × 8 × 6 Monkhorst–Pack grid Brillouin zone sampling throughout all of calculations. Maximally localized Wannier functions were constructed from La 5*d*, Se 4*p*, and F 2*p* states as projection functions using Wannier90 code[20].

References

(1) Morkoç, H.; Strite, S.; Gao, G. B.; Lin, M. E.; Sverdlov, B.; Burns, M. *J. Appl. Phys.* **1994**, *76* (3), 1363.

(2) Baliga, B. J. *IEEE Electron Device Lett.* **1989**, *10* (10), 455.

(3) Yu, X.; Marks, T. J.; Facchetti, A. *Nat. Mater.* **2016**, *15* (4), 383.

(4) Ginley, D. S.; Bright, C. *MRS Bull.* **2000**, *25* (8), 15.

(5) Dresselhaus, M. S.; Dresselhaus, G.; Jorio, A. *Group Theory: Application to the Physics of Condensed Matter*; Springer Science & Business Media, 2007.

(6) Shannon, R. D. *Acta Crystallogr. A* **1976**, *32* (5), 751.

(7) Elliott, S. R. *Physics of Amorphous Materials*; Longman: London, 1984.

(8) Scanlon, D. O.; Walsh, A. *Acta Crystallogr. Sect. B Struct. Sci. Cryst. Eng. Mater.* **2015**, *71* (6), 702.

(9) Buckeridge, J.; Butler, K. T.; Catlow, C. R. A.; Logsdail, A. J.; Scanlon, D. O.; Shevlin, S. A.; Woodley, S. M.; Sokol, A. A.; Walsh, A. *Chem. Mater.* **2015**, *27* (11), 3844.

(10) DiVincenzo, D. P.; Mele, E. J. *Phys. Rev. B* **1984**, *29* (4), 1685.

(11) Ohta, T.; Bostwick, A.; Seyller, T.; Horn, K.; Rotenberg, E. *Science* **2006**, *313* (5789), 951.
(12) Hoffmann, R. *Angew. Chem. Int. Ed. Engl.* **1987**, *26* (9), 846.
(13) Kamiya, T.; Hosono, H. *NPG Asia Mater.* **2010**, *2* (1), 15.
(14) Mizoguchi, H.; Kamiya, T.; Matsuishi, S.; Hosono, H. *Nat. Commun.* **2011**, *2*, 470.
(15) Eng, H. W.; Barnes, P. W.; Auer, B. M.; Woodward, P. M. *J. Solid State Chem.* **2003**, *175* (1), 94.
(16) TOPAS, Version 3, Brucker AXS, Karlsruhe, Germany, 2005.
(17) Paul Kubelka; Franz Munk. *Z Tech Phys* **1931**, *12*, 593.
(18) Kresse, G.; Furthmüller, J. *Phys. Rev. B* **1996**, *54* (16), 11169.
(19) Anisimov, V. I.; Zaanen, J.; Andersen, O. K. *Phys. Rev. B* **1991**, *44* (3), 943.
(20) Mostofi, A. A.; Yates, J. R.; Lee, Y.-S.; Souza, I.; Vanderbilt, D.; Marzari, N. *Comput. Phys. Commun.* **2008**, *178* (9), 685.
(21) Hulliger, F.; Lévy, F. A. *Structural Chemistry of Layer-Type Phases*, 1976 edition.; Springer: Place of publication not identified, 2011.
(22) Bergmann, H. *Sc, Y, La-Lu Rare Earth Elements: C 9 Compounds with Se*, 8th ed. 1985 edition.; Springer: Berlin, 1985.
(23) Widerøe, M.; Fjellvåg, H.; Norby, T.; Willy Poulsen, F.; Willestofte Berg, R. *J. Solid State Chem.* **2011**, *184* (7), 1890.
(24) Schleid, T.; Folchnandt, M. *Z. Für Anorg. Allg. Chem.* **1996**, *622* (3), 455.
(25) Inorganic Crystal Structure Database https://icsd.fiz-karlsruhe.de/search/index.xhtml.

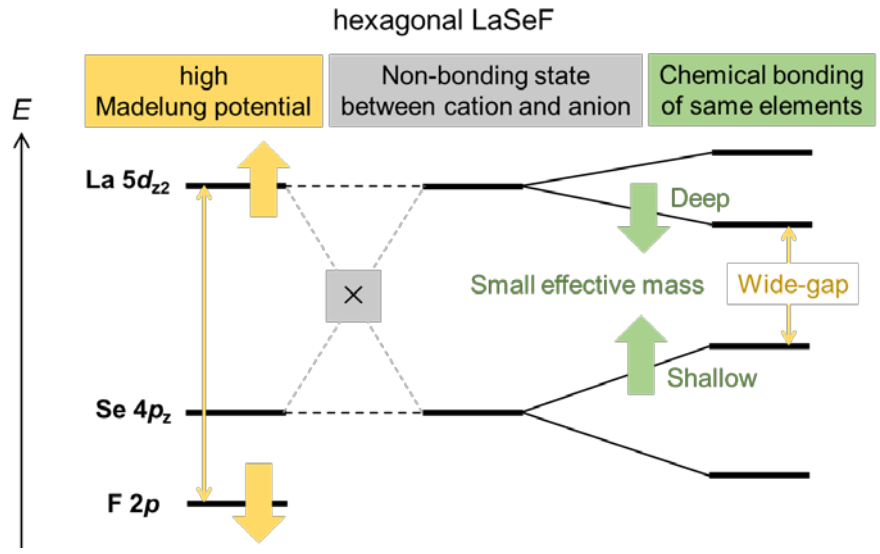

Figure 1. Design for wide-gap bipolar semiconductor. In the case of hexagonal LaSeF, the high Madelung potential between La and F ions induces the wide-gap state. Then, the non-bonding state between La 5*d* and Se 4*p* orbitals prevents the CB and VB from being flat band. Finally, the chemical bonding between same elements, La-La and Se-Se, establishes the electronic structure suitable for bipolarity.

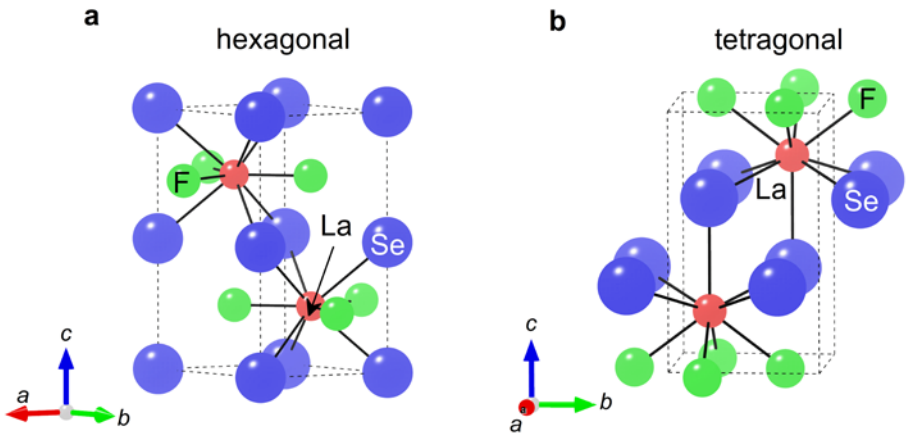

Figure 2. Crystal structures of hexagonal and tetragonal LaSeF. **a**, **b.** Crystal structures of *h*-LaSeF (**a**) and *t*-LaSeF (**b**). Red, blue, and green spheres represent La, Se, and F atoms, respectively.

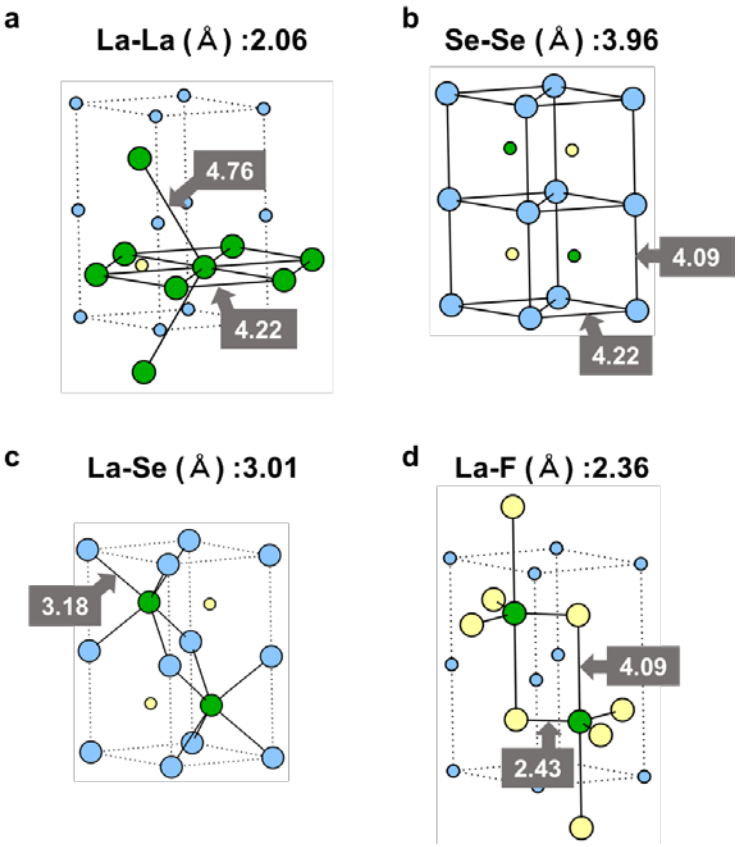

Figure 3. Distances of each atom for hexagonal phase of LaSeF. The distance estimated from ionic radius are represented on right of name of relevant distance (*e.g.* 2.06 Å for La-La). Red, blue, and green spheres represent La, Se, and F atoms, respectively. The distances correspond to the separation of La and La (**a**), Se and Se (**b**), La and Se (**c**), and La and F (**d**).

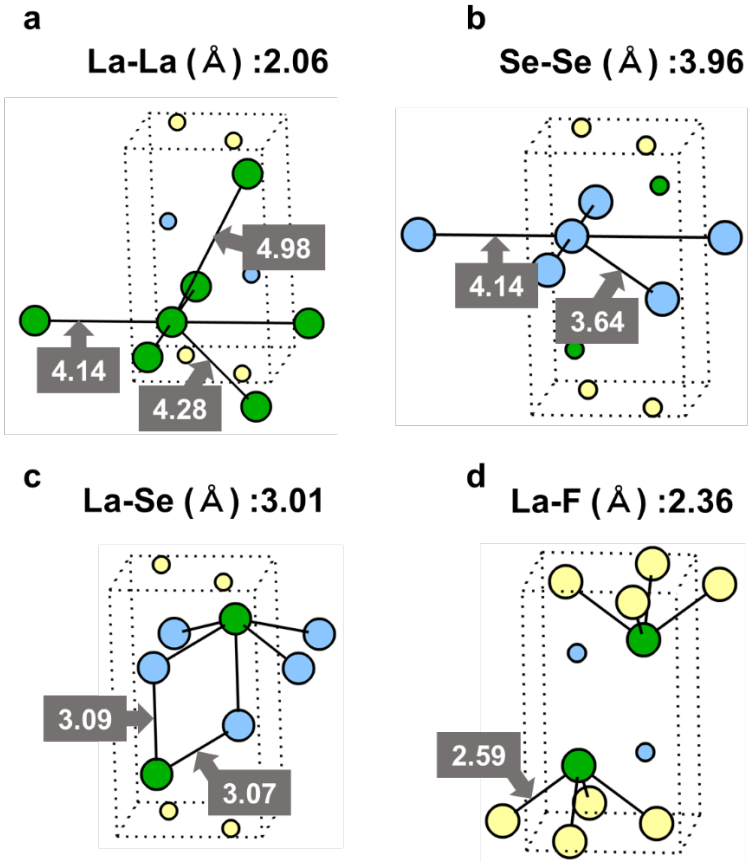

Figure 4. Distances of each atom for tetragonal phase of LaSeF. The distance estimated from ionic radius are represented on right of name of relevant distance (*e.g.* 2.06 Å for La-La). Red, blue, and green spheres represent La, Se, and F atoms, respectively. The distances correspond to the separation of La and La (**a**), Se and Se (**b**), La and Se (**c**), and La and F (**d**).

Table 1. Irreducible representations (Irrep) of each constitute of hexagonal LaSeF at the Γ point: its space and point groups are $P6_3/mmc$ and D_{6h}, respectively. The irrep of CBM and VBM are G_{1+} (in-phase configuration of La d_{z2} orbital) and G_{2-} (in-phase configuration of Se p_z orbital), respectively.

Atom	Site (site symmetry)	Orbital	Irrep	
			In-phase	Out-of-phase
La	2*c* (-6m2)	d_{x2-y2}/d_{xy}	G_{6+}	G_{5-}
		d_{z2}	**G_{1+}**	G_{4-}
		d_{yz}/d_{zx}	G_{5+}	G_{6-}
Se	2*a* (-3*m*.)	p_x/p_y	G_{5-}	G_{6-}
		p_z	**G_{2-}**	G_{4-}
F	2*d* (-6*m*2)	p_x/p_y	G_{5-}	G_{6+}
		p_z	G_{2-}	G_{3+}

Table 2. Irrep of each constitute of tetragonal LaSeF at the Γ point: its space and point groups are $P4/nmm$ and D_{4h}, respectively. The irrep of CBM and VBM are G_{4-} (out-of-phase configuration of La d_{x2-y2} orbital) and G_{5-} (in-phase configuration of Se p_x/p_y orbitals), respectively.

Atom	Site	Orbital	Irrep	
	(Site symmetry)		In-phase	Out-of-phase
La	2*c* (4*mm*)	d_{x2-y2}	G_{3+}	**G_{4-}**
		d_{z2}	G_{1+}	G_{2-}
		d_{xy}	G_{4+}	G_{3-}
		d_{yz}/d_{zx}	G_{5+}	G_{5-}
Se	2*c* (4*mm*)	p_x/p_y	**G_{5-}**	G_{5+}
		p_z	G_{2-}	G_{1+}
F	2*a* (-4*m*2)	p_x/p_y	G_{5-}	G_{5+}
		p_z	G_{2-}	G_{3+}

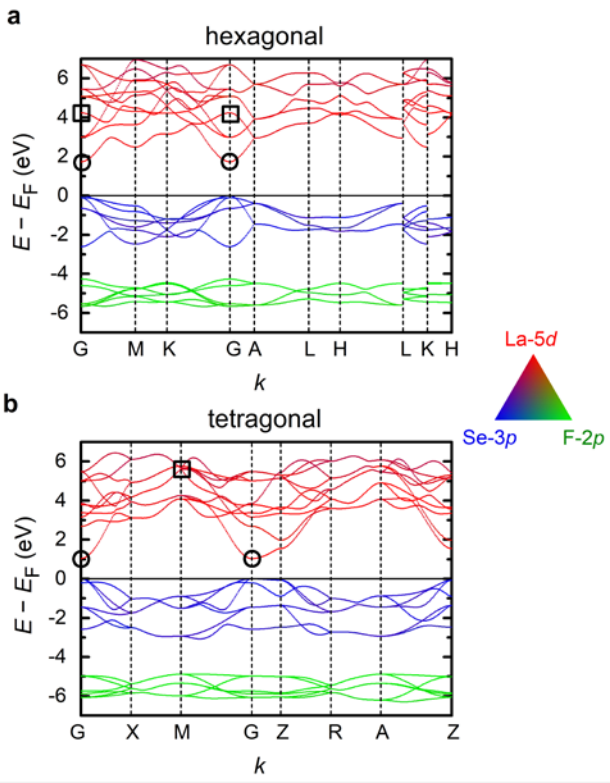

Figure 5. Band structures of *h*-LaSeF (**a**) and *t*-LaSeF (**b**). Red, blue, and green colors denote the character of the bands by projections of the wave function on the La-5*d*, Se-4*p* and F-2*p* Wannier orbitals as shown by the triangle color bar. The black open circles and squares in the band structure indicate the bonding and anti-bonding states, respectively, based on La-5d_{z2} orbitals for *h*-LaSeF and La-5d_{x2-y2} orbitals for *t*-LaSeF.

Table 3. Electron and hole effective masses of each *k*-path for *h*-LaSeF and *t*-LaSeF.

	hexagonal		tetragonal	
	G-K	G-A	G-M	G-Z
m_e^* (m_0)	0.71	0.57	**0.45**	**1.34**
m_h^* (m_0)	**0.83**	**0.24**	0.99	4.35

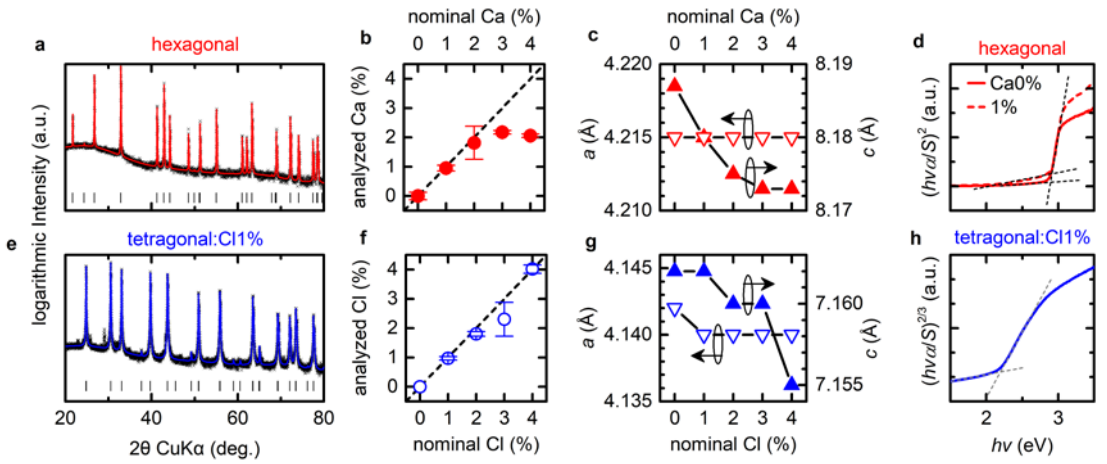

Figure 6. Structural, chemical, and optical properties of LaSeF. **a, e.** XRD patterns of non-doped *h*-LaSeF (**a**) and Cl1%-doped *t*-LaSeF (**e**). Black symbols and red/blue solid line represent the experimental data and Rietveld fitting patterns, respectively. The black tick marks below the patterns indicate the peak positions of *h*-LaSeF and *t*-LaSeF. **b, f.** Relationship between nominal and analyzed content of Ca in *h*-LaSeF (**b**) and Cl in *t*-LaSeF (**f**). The black dashed line denotes the ideal line calculated assuming the nominal content is equal to the analyzed content. **c, g.** Doping dependence of lattice constants. Filled and open symbols denote *a*- and *c*-axis lengths, respectively. **d, h.** Absorption spectra of *h*-LaSeF (**d**) and *t*-LaSeF (**h**) derived from diffuse reflectance spectra at 300 K and the Kubelka−Munk relation, where α, s, and $h\nu$ are the absorption coefficient, scattering factor, and photon energy, respectively. The vertical axis for direct allowed transition and direct forbidden transition are $(h\nu\alpha/s)^2$ and $(h\nu\alpha/s)^{2/3}$, respectively. The black dashed lines are a guide for the eyes.

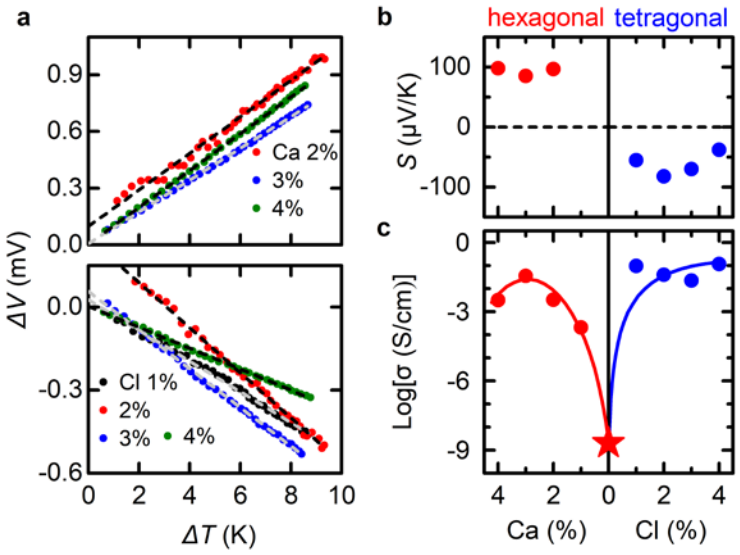

Figure 7. Transport properties of LaSeF. **a.** Results of thermopower measurements for Ca-doped *h*-LaSeF (upper) and Cl-doped *t*-LaSeF (bottom). The dashed line indicates linear fitting results. **b.** Doping dependence of the Seebeck coefficient at T = 300 K. **c.** Doping dependence of conductivity at T = 300 K. The solid line is a guide for the eyes.

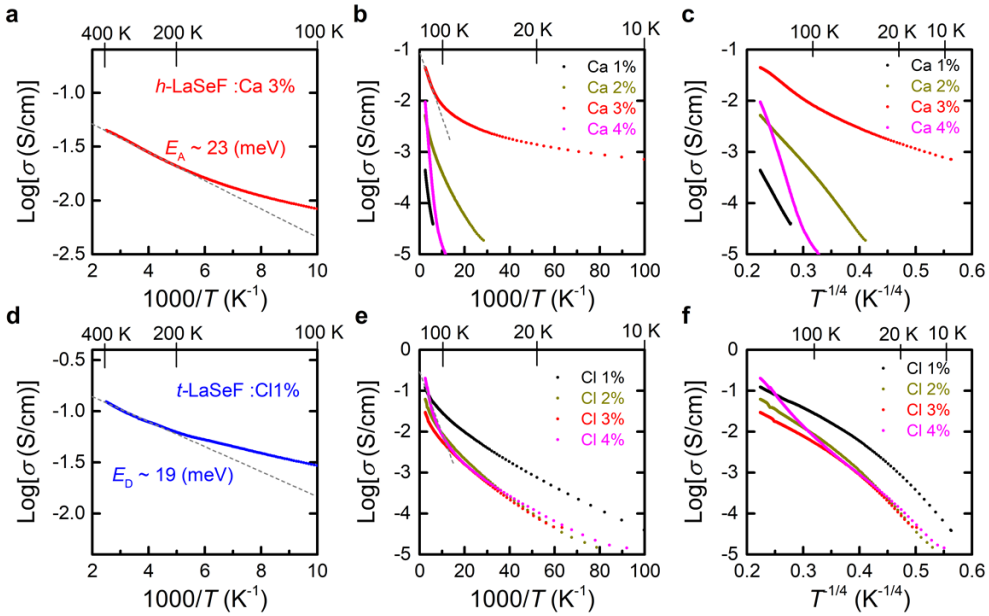

Figure 8. Electrical conductivity as a function of temperature. **a, d.** Electrical conductivity of Ca 3% doped *h*-LaSeF (**a**) and Cl 1%-doped *t*-LaSeF (**d**). The range of both fitting is from 2 (T = 400 K) to 5 (T = 200 K). **b, e.** Electrical conductivity including low temperature region for Ca doped *h*-LaSeF (**b**) and Cl doped *t*-LaSeF (**e**). **c, f.** $T^{-1/4}$ plot for electrical conductivity of Ca doped *h*-LaSeF (**c**) and Cl doped *t*-LaSeF (**f**).

Table 4. Total energies of two competing structure in various compositions.

Composition	LaSeF		YOCl		YSF		LaTeCl		YSeF	
Structure-type	PbClF	ZrBeSi	PbClF	SmSI	PbClF	YSF	PbClF	PbCl2	PbClF	YSeF
Total energy/atoms, E (eV/atom)	-6.280	-6.284	-7.846	-7.858	-7.481	-7.408	-5.619	-5.622	-7.123	-7.112
$E_{PbFCl} - E_{polymorph}$ (meV/atom)	4		12		-73		3		-11	

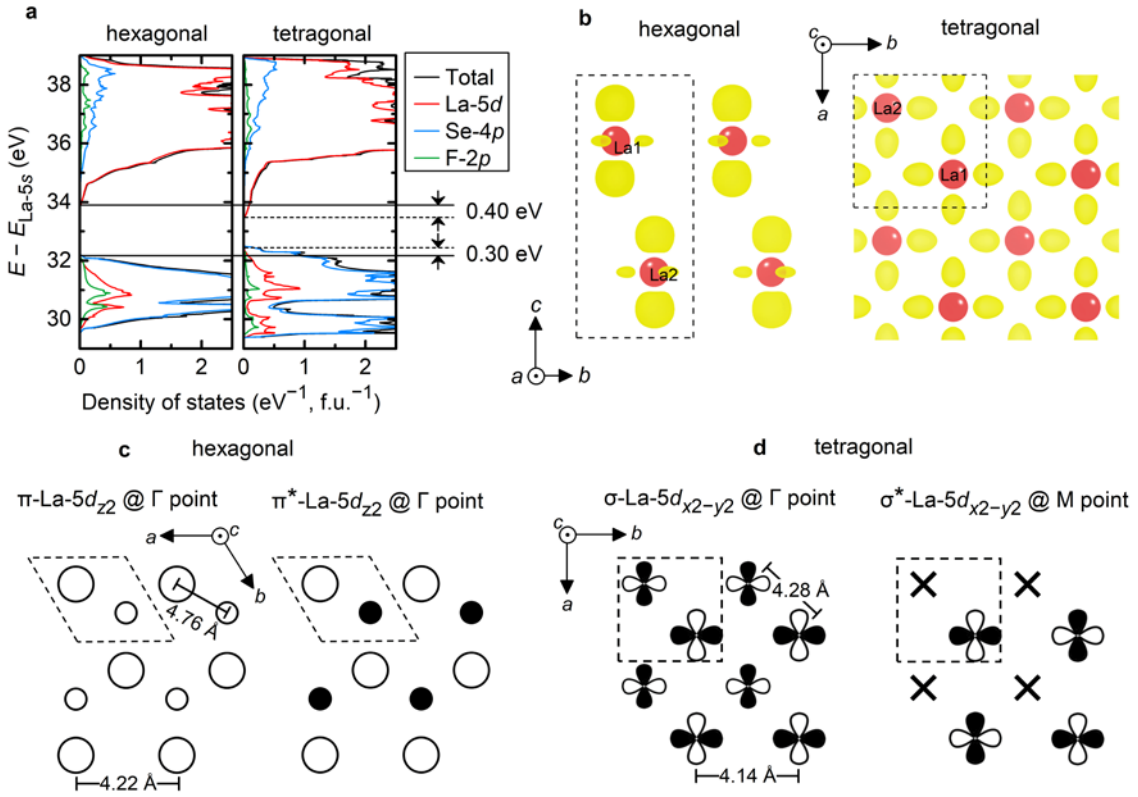

Figure 9. Comparison of electronic structures and chemical states of hexagonal and tetragonal phases. **a.** DOS of *h*-LaSeF (left) and *t*-LaSeF (right). The vertical axis is aligned by the La-5*s* levels located approximately 32−33 eV below their VBM. **b.** Electron density mapping at the CBM state of *h*-LaSeF (left) and *t*-LaSeF (right). Although the two La atoms in the unit cell are crystallographically identical, here we denote the La atom at *z* 0.75−0.80 as La1 and that at 0.20−0.25 as La2 for clarity. **c, d.** Orbital configuration of bonding and anti-bonding states of La-5d_{z2} in *h*-LaSeF (**c**) and La-5d_{x2-y2} for *t*-LaSeF (**d**). The black dashed line denotes the unit cell. The orbital in the La2 site is drawn lightly. The cross sign in right panel of **Figure 4d** indicates non-bonding states because La-5d_{x2-y2} orbitals at this site cannot form any bonding or anti-bonding states with neighboring orbitals.

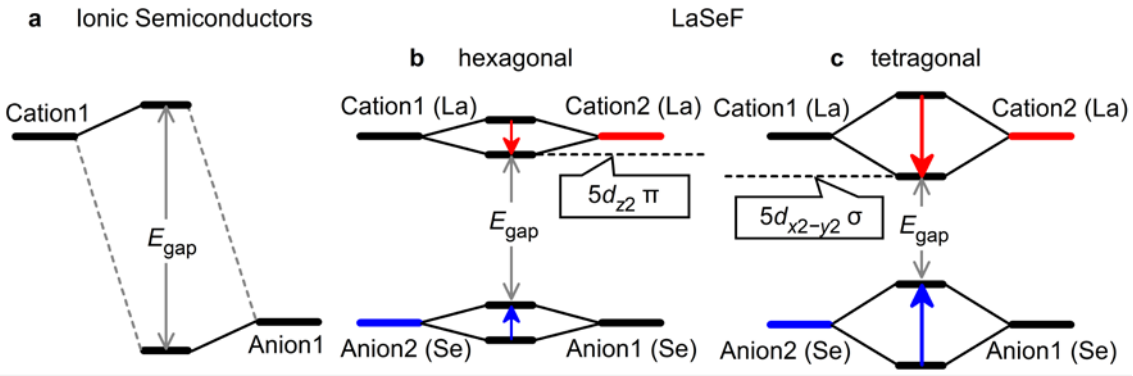

Figure 10. Schematic molecular orbital diagram of conventional ionic semiconductors and the LaSeF polymorphs. **a.** Molecular orbital diagram for semiconductors with less covalency. **b, c.** Molecular orbital diagram for the *h*-LaSeF (**b**) and *t*-LaSeF (**c**). Owing to the poor orbital overlap between cation1 and cation2 in the hexa-phase, the CBM position is shallower than that of the tetra-phase and the situation reverses for the VBM. The red and blue allows represent the degree of orbital overlap between cation-cation enlarging the conduction band width and between anion-anion enlarging the valence band width, respectively.

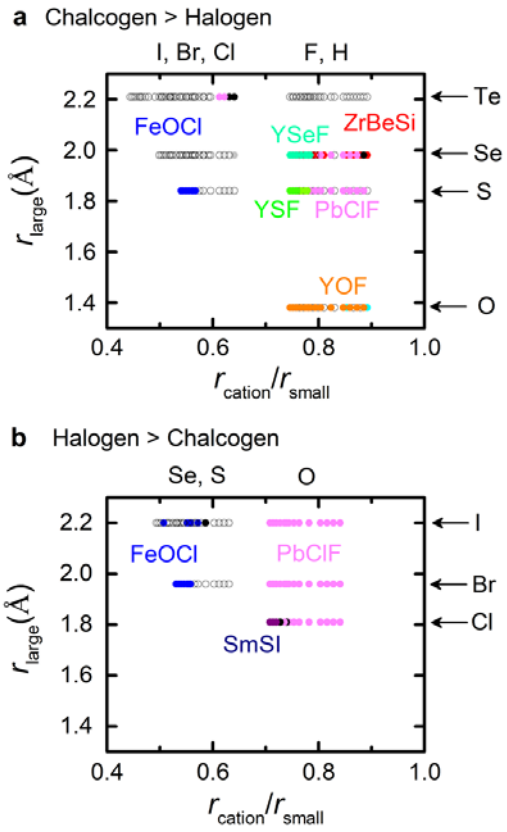

Figure 11. Structure map of ternary rare earth mixed anion compounds. **a.** Case where chalcogen anion is larger than halogen anion. **b.** Case where halogen anion is larger than chalcogen anion. The horizontal axis represents the value that the ionic radius of cation (rare earth elements) is divided by the ionic radius of small anion. The vertical axis represents the ionic radius of large anion. Seven structure types are shown color: blue for FeOCl, gray for YSeF, pink for PbClF-type, yellow for YSF, green for YOF, black for compositions forming polymorph, red for ZrBeSi and HoHSe, and purple for SmSI. [21,22,23,24,25] HoHSe can be regarded as a polytype of ZrBeSi if the ZrBe honeycomb layer is shifted parallel to the *ab* plane. No color represents no structure data.

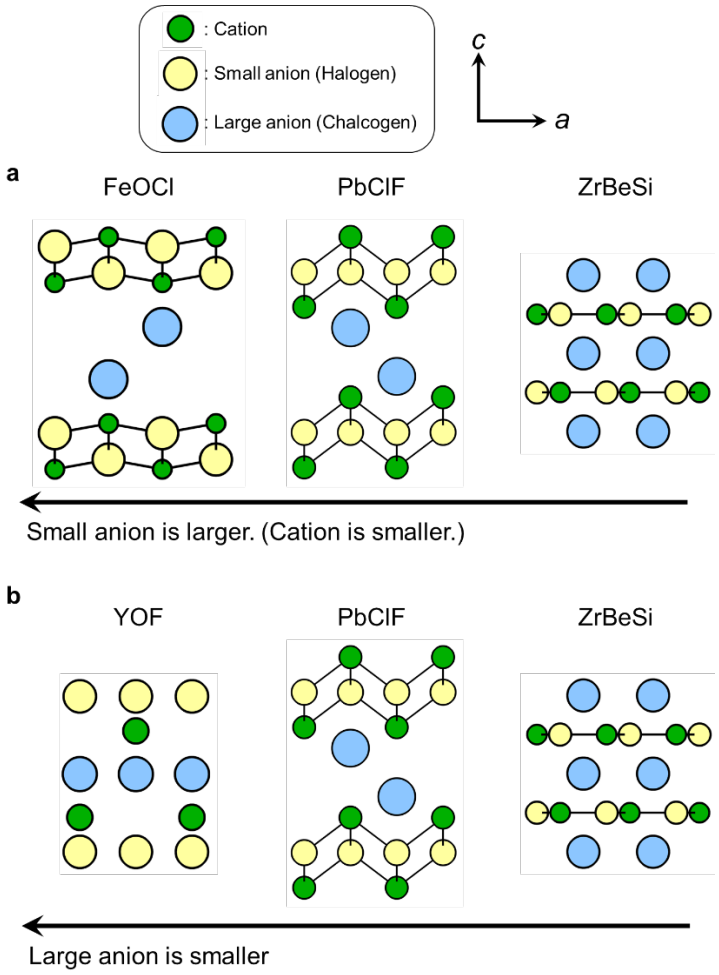

Figure 12. Tendency of structural change depending on ionic radius in the case where chalcogen anion is larger than halogen anion. Large anion separates layers composed of cation and small anion, except for ZrBeSi-type which is a unique structure where a small anion is adjacent to a large anion. As the small anion becomes larger (or cation and large anion become smaller), ZrBeSi-type turns into PbClF-type because the structure where anions are neighboring become unstable. Substituting Cl into Se site of *h*-LaSeF denotes the case of (**b**). Thus, this substitution encourages the structural-type change from ZrBeSi to PbClF.

Chapter 4. General conclusion

The present study accomplished the bipolar doping or the carrier polarity switch in the wide-gap semiconductors based on the early transition metals.

Main conclusion **(Figure 1)**

The semiconductors based on early transition metals the efficient controllability of carrier polarity and density, in future, and will be one of the applicable wide-gap semiconductors.

Conclusions **(Figure 2)**

1. *The compositions, AChX (A = Y, Zr, La, and Hf, Ch = chalcogens, and X = oxygen and fluorine), are suitable for designing the wide-gap and p-type conduction because X anion widens the bandgap due to its high Madelung potential and chalcogen anion is suitable for hole transport owing to its small ionization potential and spatially spread p orbitals.*

2. *Orbital symmetry and crystal structure are key to establish conduction band suitable for electron transport. The d orbital of early transition metals is required to form non-bonding state with neighboring anion p orbitals and σ-bonding state with d orbitals of neighboring same element.*

3. *Chemical bonding of anion p orbital is important to constitute valence band appropriate for hole conduction. Anion p orbital is better to form non-bonding with neighboring cation d orbitals and strong anti-bonding with neighboring anion p orbitals.*

Secondary conclusion

Concept for controlling polymorph brings novel design for wide-gap bipolar semiconductors. This design requires polymorph based on two structures; first structure is suitable for n-type and second structure is appropriate for p-type.

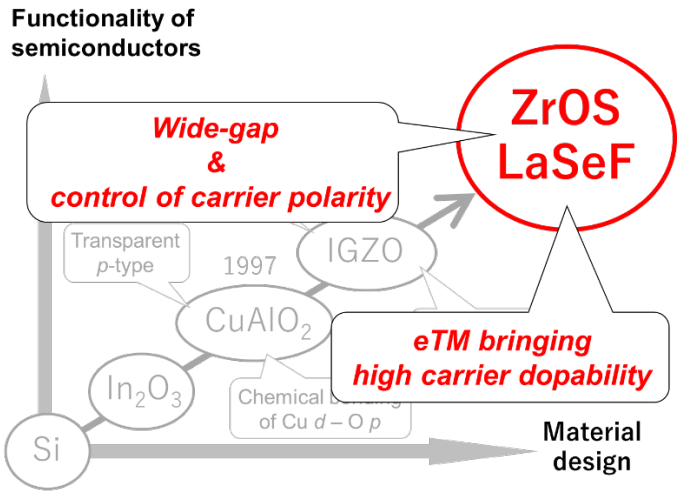

Figure 1. Summary of main conclusion. This figure corresponds to **Figure 1 of *General introduction***. The early transition metals (*e*TM) based semiconductors will be one class of major functional semiconductors. The compositions of eTM have structures with high coordination number which brings the high dopability of carrier. This feature induces the high controllability of carrier polarity.

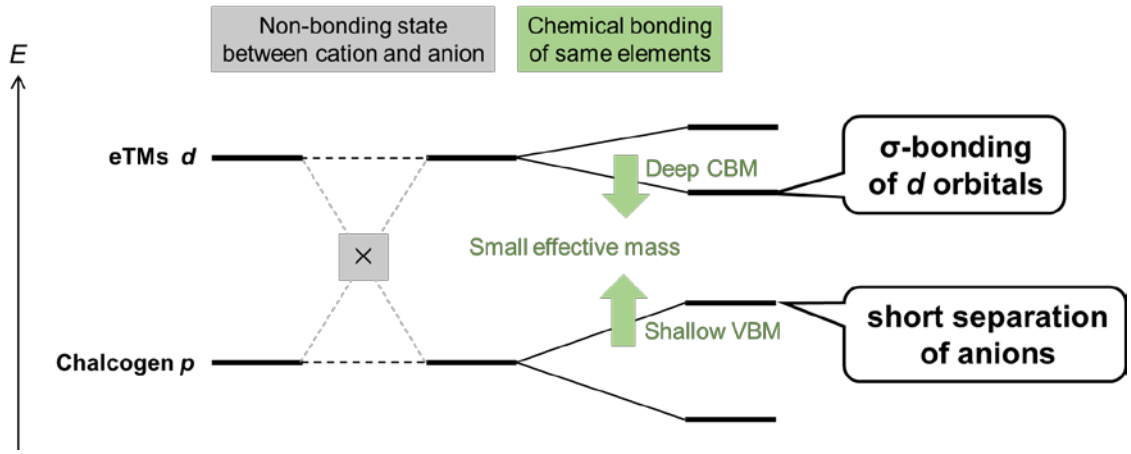

Figure 2. Summary of conclusions. Bipolarity requires non-bonding state between cation and anion and strong covalent nature between same elements.

Acknowledgement

This study was carried out in *Hosono, Kamiya, Hiramatsu & Katase Laboratory* at the Tokyo Institute of Technology from April 2015 to March 2018. Numerous people have contributed to this study.

First of all, I would like to express gratitude to Prof. ***Hideo Hosono*** for their advice and continuous encouragement. Also, I would like to express my sincere thanks to Assistant Prof. ***Soshi Iimura*** for their kind guidance, discussions, and important suggestions. I learned a lot from them such as a sense of materials research.

I am indebted to Prof. ***Toshio Kamiya***, Prof. ***Satoru Fujitsu***, Prof. ***Hideya Kumomi***, Prof. ***Toshiharu Yokoyama***, Associate Prof. ***Hidenori Hiramatsu***, Associate Prof. ***Satoru Matsuishi***, Associate Prof. ***Masaaki Kitano***, Associate Prof. ***Tomofumi Tada***, Associate Prof. ***Masato Sasase***, Associate Prof. ***Hiroshi Mizoguchi***, Assistant Prof. ***Yoshitake Toda***, Assistant Prof. ***Fuji Funabiki***, Assistant Prof. ***Junghwan Kim***, Assistant Prof. ***Keisuke Ide***, Dr. ***Yangfan Lu***, Dr. ***Joonho Bang***, Dr. ***Kosuke Matsuzaki***, Dr. ***Jiazhen Wu***, Dr. ***Junjie Wang***, Dr. ***Taku hanna*** (currently at ULVAC Inc,), and Dr. ***Yoshinori Muraba*** for their kind help and suggestions.

I also would like to thank, Mr. ***Yudai Tomota***, Mr. ***Hikaru Sato*** (currently at General Electric Company Inc,), Mr. ***Junichi Ishida***, Mrs. ***Yukiko Obata***, Mr. ***Sang Won Park,*** Mr. ***Hiroshi Okanishi*** (currently at Deloitte Touche Tohmatsu Inc,), Mr. ***Kota Hanzawa***, Mr. ***Takuya Nakao***, Mr. ***Takashi Sasaki*** (currently at Panasonic Inc,), Mr. ***Taehwan Jun*** and other members of the *Hosono, Kamiya, Hiramatsu & Matsuishi Laboratory*.

Further I am indebted to Mr. ***Yuji Kondo***, Mr. ***Shizuo Hayashi***, and Mr. ***Kenji Ariga*** for helping me to analyze the chemical composition and perform the high pressure apparatus. I would like to acknowledge Secretaries Ms. ***Hanae Murayama***, Ms. ***Mayumi Nakano***, and Ms ***Kanako Ochiai*** *for their kind helps to my research works*.

Finally, I express appreciation to my family and friends.

March 2018

Takeshi Arai

Publication lists

Papers included in the thesis

T. Arai, S. Iimura, J. Kim, Y. Toda, S. Ueda, and H. Hosono
"Chemical Design and Example of Transparent Bipolar Semiconductors"
Journal of the American Chemical Society **2017**, *139* (47), 17175–17180.
This paper was chosen as "Spotlights on Recent *JACS* Publications".

T. Arai, S. Iimura, and H. Hosono
"Doping induced polymorph and carrier polarity changes in LaSeF"
Chemistry of Materials, **2018**, 30, 597–601.

Other papers

A. Shi, **T. Arai**, S. Kitagawa, T. Yamanaka, K. Ishida, A. E. Bohmer, C. Meingast, T. Wolf, M. Hirata, and T. Sasaki
"Pseudogap Behavior of the Nuclear Spin-Lattice Relaxation Rate in FeSe Probed by 77Se-NMR"
Journal of the Physical Society of Japan 2017, 87 013704

A. E. Böhmer, **T. Arai**, F. Hardy, T. Hattori, T. Iye, T. Wolf, H. Löhneysen, K. Ishida, and C. Meingast,
"Origin of the Tetragonal-to-Orthorhombic Phase Transition in FeSe: A Combined Thermodynamic and NMR Study of Nematicity"
Physical Review Letters 2015, *114* (2), 027001.

Presentation lists

Domestic Presentation

Invited

1. **新井健司**, 飯村壮史, 金正煥, 細野秀雄
   「透明バイポーラ酸化物半導体: ZrOS」
   第 78 会応用物理学会秋季学術講演会 (2017 年 9 月 5-8 日, 福岡国際会議場, 福岡)

Oral

1. **新井健司**、飯村壮史、金正煥、細野秀雄
   「透明バイポーラ酸化物半導体: ZrOS」
   第 64 回応用物理学会春季学術講演会（2017 年 3 月 14-17 日, パシフィコ横浜、神奈川

2. **新井健司**, 家哲也, 石田憲二, A. E. BOHMER, F. HARDY, P. SCHWEISS, T. WOLF, C. MEINGAST
   「77Se-NMR を用いた単結晶 FeSe の超伝導状態の研究」
   日本物理学会第 70 回年次大会 (2015 年 3 月 21-24 日 早稲田大学、東京)

3. **新井健司**, A. E. BÖHMER, 家哲也, 石田憲二, F. HARDY, P. SCHWEISS, T. WOLF, C. MEINGAST
   「単結晶 FeSe の 77Se - NMR を用いた構造と磁性・超伝導の研究」
   日本物理学会 2014 年秋季大会 (2014 年 9 月 7-10 日 中部大学、愛知)

4. **新井健司**, A. E. BÖHMER, 家哲也, 石田憲二, F. HARDY, P. SCHWEISS, T. WOLF, C. MEINGAST
   「単結晶 FeSe の構造転移と超伝導の 77Se-NMR を用いた研究」
   日本物理学会第 69 回年次大会 (2014 年 3 月 27-30 日 東海大学、神奈川)

Awards

JSAP 42th Young Scientist Presentation Award (第 42 回 応用物理学会講演奨励賞)
「透明バイポーラ酸化物半導体: ZrOS」

Biography

Date of birth: 7th November 1989.

Education

Mar. 2013 Bachelor from Department of Physics, Kyoto University, Japan.
Mar. 2015 Master from Department of Physics, Kyoto University, Japan.